NASA CR-165,704

NASA Contractor Report 165704

EXPERIMENTAL AND ANALYTICAL STUDIES OF A
TRUE AIRSPEED SENSOR

G. L. Goglia and J. Y. Shen

OLD DOMINION UNIVERSITY RESEARCH FOUNDATION
Norfolk, Virginia 23508

NASA

National Aeronautics and
Space Administration

Langley Research Center
Hampton, Virginia 23665

TABLE OF CONTENTS

LIST OF TABLES

LIST OF FIGURES

LIST OF FIGURES (CONTINUED)

EXPERIMENTAL AND ANALYTICAL STUDIES OF
A TRUE AIRSPEED SENSOR

By

G.L. Goglia[1] and J.Y. Shen[2]

ABSTRACT

The objective of this study was to analyze and design a true airspeed sensor to replace the conventional pitot-static pressure transducer. This indicator should have a flow phenomenon which is the vortex precession or the "vortex whistle," no moving parts, and also be independent of temperature, density, altitude or humidity changes. This indicator was to be designed mainly for small commercial aircraft with airspeeds up to 321.9 km/hr (200 mph).

In an attempt to model the complicated fluid mechanics of the vortex precession, three-dimensional, inviscid, unsteady, incompressible fluid flow was studied by using the hydrodynamical linearized stability theory. The temporal stability approach was used to derive the relationship between the true airspeed and frequency response. The results show that the frequency response is linearly proportional to the airspeed.

The designed sensor basically consisted of a vortex tube, a swirler, and a pickup system. When air passed through the swirler, a precessional flow was generated at the region before and after the sudden enlargement area. An audible vortex whistle was also generated. The signal was picked up by the microphone, and the frequency response shown in a frequency counter. Measurements for both the closed-conduit test and wind-tunnel test were recorded.

A computer program was developed to obtain the numerical solution. The parameters describing the sensor were introduced into the calculation.

---

[1] Eminent Professor and Chairperson, Department of Mechanical Engineering and Mechanics, Old Dominion University, Norfolk, Virginia 23508

[2] Graduate Research Assistant, Department of Mechanical Engineering and Mechanics, Old Dominion University, Norfolk, Virginia 23508

Computational results for various combinations of vortex tubes and swirlers were obtained.

For a specific flow rate or airspeed, the larger the exit swirler angle, the greater was the frequency response. For a smaller cross-sectional area at a precessional flow region, the frequency response was higher. It was observed that as the airspeed was increased the Strouhal number remained constant. The Strouhal number was found to be only dependent on the exit angle of swirler.

In some cases, the experimental results were found to be in reasonable agreement with the theoretical predictions. The viscous effect on the performance of the sensor was appreciable, especially for some sensors.

C constant, defined in equation (52)

c_1, c_2 arbitrary constants

D_1 diameter of swirler generation region, defined in figure 1, cm

D_2 diameter of swirler, defined in figure 1, cm

D_3 diameter of precessional flow region, defined in figure 1, cm

f function of radius r, amplitude of preliminary complex solution in r-direction

F frequency response, KHz

g function of radius r, amplitude of preliminary complex solution in θ-direction

h function of radius r, amplitude of preliminary complex solution in z-direction

k wavenumber, a real number

K parameter, defined in equation (40)

n integer

p actual fluid pressure, kg/cm^2

p' pressure fluctuation, kg/cm^2

$\hat{p}'$ preliminary complex solution in pressure

$\bar{p}'$ mean pressure, kg/cm^2

q function of radius r, amplitude of preliminary complex solution in pressure

Q flow rate, m^3/min

r radius or radial coordinate, cm

R radius of precessional flow region, defined in figure 1, cm

Re Reynolds number based on mean axial velocity and D_3

St Strouhal number based on mean axial velocity and D_3

t time, sec

u	actual fluid radial velocity, km/hr
u'	velocity fluctuation in r-direction, km/hr
û'	preliminary complex solution in r-direction, km/hr
U	true airspeed, km/hr
v	actual fluid tangential velocity, km/hr
v'	velocity fluctuation in θ-direction, km/hr
v̂'	preliminary complex solution in 0-direction, km/hr
$\overline{V}$	mean velocity in 0-direction, km/hr
w	actual fluid axial velocity, km/hr
w'	velocity fluctuation in z-direction, km/hr
ŵ'	preliminary complex solution in z-direction, km/hr
$\overline{W}$	mean velocity in z-direction, km/hr
W_c	constant mean axial velocity, km/hr
z	axial coordinate
α	exit swirler angle, defined in figure 59
θ	θ-coordinate
ρ	fluid density, g/cm^3
ω	angular velocity, a constant complex number
ω_o	constant upstream fluid angular velocity
*	complex conjugate of preliminary complex solution

4

INTRODUCTION

At the present time there are two types of airspeed instruments which might be used on aircraft: the differential-pressure type and the true airspeed meter. However, the pitot-static instrument, which is of the differential-pressure type, is exclusively used. This indicator is calibrated in terms of airspeed at a standard air density. In order to obtain the actual airspeed at other densities, a correction must be made. The performance of the pitot-static tube is greatly affected by installation location. One must therefore find a location for the pitot-static openings that will be free from structual interference effects.

The true airspeed sensor is the conventional type of meter with rotating surfaces, such as propellers, which gives readings independent of air density. The sensor is usually used in making measurements of airspeeds in the lower ranges. One kind of true airspeed sensor used by the United States Navy on airships is known as the commutator-condensor type.

The idea of designing a true airspeed sensor originated from the discovery of vortex whistle and the flow phenomenon-precession, which is different from that of vortex shedding. The origin of the sound or whistle was studied by a few investigators (refs. 1-3) from different points of view. The vortex shedding problems associated with the aerolian tones and edgetones were also studied and observed experimentally by many researchers (refs. 4-12). Very few people worked on the vortex whistle and precessional flow problems. Bernard Vonnegut (ref. 13) in 1954 was the first to discover and investigate the vortex whistle. His laboratory was conducting an experiment on a vortex creating housing for aircraft thermometers. During the experiment he observed that a sound was generated when the rotating air escaped from the open end of the tube. He also found that the frequency of this sound increased with increasing rates of air flow. In addition, the frequency that was produced decreased as the length of the tube in which the vortex rotated was increased. Vonnegut suggested that the vortex instability leaving the tube caused the whistle and developed an empirical formula describing the performance of his whistle.

In 1955, Irving Michelson (ref. 14) published the first analytical work on the theory of a vortex whistle. He considered the flow throughout the whistle to be two-dimensional, unsteady, inviscid, and isentropic. He introduced the parameters s, u', and v', where s was a non-dimensional density perturbation. By this method he was able to arrive at linearized simultaneous equations. A secular equation was then derived, noting one root of particular interest. From the solution and the secular equation, he noted the occurrence of a frequency which was proportional to the flow speed U. When he introduced the isentropic flow relationship, he was able to express the frequency in terms of pressure drop and reservoir sound speed c_1.

Michelson's theory compares very favorably with Vonnegut's empirical formula, particularly when constants 1.09 and 1.19 are used in Michelson's theory for monoatomic and diatomic gases, respectively.

In 1957, J.P. Nicklas (ref. 15) reported his work on the investigation of a vortex tube, acoustic, true airspeed sensor conducted at the Cornell Aeronautical Laboratory. He investigated the feasibility of measuring true aircraft airspeed by measuring the frequency of the sound produced in a vortex tube mounted on an airplane. Nicklas, however, concentrated his efforts on the single tangential nozzle vortex tube. His data revealed that the fundamental sound frequency of a vortex tube could be considered a linear function of true airspeed in the subsonic speed range. He indicated that the altitude and temperature sensitivities of the vortex tube could be reduced by proper design. In his conclusions, he also mentioned that no significant improvement in signal quality was obtained by modifying the tube shape. Nicklas also studied the effect the angle of attack had on frequency response.

In 1960, M. Suzuki (ref. 16) conducted studies to determine a method of eliminating the whistle occurring in the vortex tube. In his analysis he assumed both a free and forced vortex region of velocity distribution. Suzuki, using the boundary conditions at the wall and at the interface between free and forced vortex, derived a linearly proportional relationship between the peculiar frequency and the angular velocity of the forced vortex. In his derivation, the density and velocity components were separated into mean and fluctuation terms. Suzuki introduced a

number of assumptions and restrictions in order to obtain the Bessel's equation and its solution. Although Suzuki did not present either numerical or quantitative results, he did report and discuss his experimental data. In addition to the linear relationship, Suzuki found that no sound was produced at small flow rates and that, when the value of L_c/D_c was less than unity, no distinct frequency could be observed; L_c was the length of cold tube in his model, and D_c was the diameter of the outlet.

In 1963, Robert C. Chanaud (ref. 17) converted Vonnegut's data into Reynolds and Strouhal numbers and found that the air and water data were almost coincident, suggesting that dynamic similarity might occur. The perturbation of a two-dimensional inviscid vortex flow was investigated. Chanaud derived a linear relationship between perturbation frequency and fluid angular velocity for neutrally stable oscillations of an inviscid flow. His results support the investigations and conclusions reported by Vonnegut and Michelson. He confirmed that the precessional frequency is the same as the sound frequency and that the fluid angular velocity is simply related to the precession frequency of the unstable motion. In his conclusion, he mentioned that high speed was not necessary to generate the whistle, as velocities of 1.5 m (5 ft) per sec were found sufficient. He, as others did, explained that the instability which occurred was due to the sudden area change at the tube exit. Chanaud's results show that the amplitude of oscillation within the tube depends on how the area changes; a gradual area increase permits larger amplitude flow oscillations whereas an abrupt area change reduces the magnitude of the flow oscillation within the tube. He mentioned that this may be the reason Vonnegut did not detect the sound with a flared tube, and also stated that no quantitative information on the nature of the instability had been obtained.

Powell (ref. 18) in 1964 published a paper discussing the origin of the sound. He showed and explained in detail, from a physical point of view, how aerodynamic sound in an unsteady fluid flow was generated as a result of the movement of vortices, or of vorticity.

In 1965, Chanaud (ref. 19) published a paper describing the experimental study in certain swirling flows. One of the swirling flows was

studied by Talbot (ref. 20). The experimental results show that the periodic motion in both a vortex whistle and a cyclone separator can be described in terms of a hydrodynamic oscillator where the frequency is closely related to the angular velocity of the flow. Chanaud also mentioned that the two important parameters, the Reynolds number and the Strouhal number, are both of such magnitude that it appears no important simplifications can be made in the equations of motion to solve the problem analytically. The energy of the oscillator is derived from the hydrodynamic instability of the fluid within a reversed-flow region on the swirl axis. No quantitative information is available on the condition of a steady reversed-flow region. Chanaud, however, mentioned that the experimental results suggest that the two-dimensional perturbation analysis may prove of some value in describing the amplifier part of the oscillator.

Rodely et al. (ref. 21) found that the oscillative motion began only beyond certain Reynolds numbers. They also observed that the oscillative motion was accompanied by the reversal of flow near the tube axis. Gove and Ranz (ref. 22) explained this reversal of flow in detail. The reversal of flow was caused by the sudden area enlargement at the tube exit. In the better swirler designs, the Rossby number could be held constant for various Reynolds numbers. This indicated that the frequency was linearly related to the flow rate. However, below some Reynolds number, due to viscous effects, there were deviations from the constant value.

Chanaud again in 1970 (ref. 23) suggested that the vibrating system in the aerodynamic whistle is the air itself. This is in contrast to nonaerodynamic devices such as a drum or loud speaker where sound is generated when a mechanical system vibrates and disturbs the air. Chanaud showed that, due to the instability of the system, a small disturbance in the stream flowing through the aerodynamic whistle was amplified, and that kinetic energy was converted to oscillatory energy. Part of the energy of the amplified disturbance is fed back upstream where the flow is most unstable, and, if the right frequency and amplitude exists, it interacts with the original disturbance to maintain the process. After a few cycles the feedback controls the input completely. A whistle

is produced when the flow speed is high enough and the frequency is in the audible range.

As mentioned in references 21 and 24 to 31, there is one common feature that introduces the concept of "no moving parts" in fluidic devices. In contrast to this concept is the device with moving parts as in reference 32. Fluidic devices have been widely researched in the past 19 years. Simplicity, reliability and easy maintenance make fluidic devices attractive. Reference 33 states, "Although present theory gives results sufficiently accurate for engineering design, it is not possible to justify all the assumptions used. Thus in a scientific sense the theory is not always satisfying, but in an engineering design sense the theory does seem to be satisfactory."

In this investigation fluidic models were designed and then tested in both water and air. Flow visualization tests in a water model were undertaken in order to actually see the flow phenomenon of precession. Smaller models were subsequently made for testing with compressed air and in a wind tunnel. A complete analytical analysis was provided in this study. The physical models were simulated and used in computer calculation. The numerical solutions involved true airspeeds up to 321.89 km (200 mi) per hr. Six different combinations of vortex tubes and swirlers were used both in computer calculations as well as in experimental tests.

The objective of this study was twofold. The first objective was to analyze and design a true airspeed indicator to replace the conventional pitot-static pressure transducer for small commercial aircraft. The desired features of this indicator should include the flow phenomenon-precession, vortex whistle, and no moving parts. In addition this indicator should not be affected by temperature, density, altitude, and humidity changes. The second objective was to obtain a numerical solution and predict the frequency response which is generated by the vortex whistle at a certain airspeed. Prior to this study, theoretical results were never presented quantitatively to enable a comparison with experimental data. Thus, this study will present a general solution to the problem and also provide specific analytical results for comparison purposes. A correction factor for viscous effects will later be

introduced to enable a correlation between theoretical results and
experimental data.

A three-dimensional, inviscid, unsteady, incompressible flow was studied by using the hydrodynamical linearized stability theory. The hydrodynamical linearized stability theory, as mentioned in references 34 to 40, has been used in a variety of problems. In the application of this theory for the temporal stability approach, the frequency was considered a constant complex quantity, and the wavenumber k a real number. Later it will be shown that, when the imaginary part of the frequency is greater than zero, the disturbance grows exponentially in time and is termed a "temporally unstable disturbance." This disturbance when amplified to a certain degree gives a definite whistle at a frequency which is linearly proportional to the true airspeed. The initial effort was devoted to the study of the disturbance caused by sudden enlargement in the rear end of the vortex tube as shown in figure 1.

For the flow described above, the continuity and momentum equations expressed in cylindrical coordinates are as follows:

continuity:

$$\frac{1}{r}\frac{\partial}{\partial r}(ru) + \frac{1}{r}\frac{\partial v}{\partial \theta} + \frac{\partial w}{\partial z} = 0 \tag{1}$$

r-momentum:

$$\frac{\partial u}{\partial t} + u\frac{\partial u}{\partial r} + \frac{v}{r}\frac{\partial u}{\partial \theta} + w\frac{\partial u}{\partial z} - \frac{v^2}{r} = -\frac{1}{\rho}\frac{\partial p}{\partial r} \tag{2}$$

θ-momentum:

$$\frac{\partial v}{\partial t} + u\frac{\partial v}{\partial r} + \frac{v}{r}\frac{\partial v}{\partial \theta} + w\frac{\partial v}{\partial z} + \frac{uv}{r} = \frac{1}{\rho r}\frac{\partial p}{\partial \theta} \tag{3}$$

z-momentum:

$$\frac{\partial w}{\partial t} + u\frac{\partial w}{\partial r} + \frac{v}{r}\frac{\partial w}{\partial \theta} + w\frac{\partial w}{\partial z} = -\frac{1}{\rho}\frac{\partial p}{\partial z} \tag{4}$$

where u, v and w denote the actual fluid radial velocity V_r, tangential velocity V_θ, and axial velocity V_z, respectively.

It is the purpose here to derive the equations that control the small disturbances of a swirling and steady mean flow. This is accomplished in three steps: separation of fluctuations, linearization, and recourse to complex functions.

According to the first step the velocities are separated into a mean value and a fluctuation from the mean. It is assumed that in the absence of fluctuations the flow is laminar and can be specified as follows:

$$u = 0, \quad v = \overline{V}(r), \quad w = \overline{W}(r), \quad p = \overline{P}(r) \tag{5}$$

where the r-component mean velocity is assumed to be zero and the fluid beyond the swirling flow generator consists of a forced vortex flow or solid body rotation. The mean flow in the θ-direction, the axial mean flow, and the pressure terms are assumed to be functions of radius only. If u', v' and w' denote the fluctuations in the r-, θ-, and z-directions, respectively, and p' denotes the fluctuation in the pressure, then the following relationships can be used to express the instantaneous velocity components and pressure:

$$u = u'(r, \theta, z, t) \tag{6}$$

$$v = \overline{V}(r) + v'(r, \theta, z, t) \tag{7}$$

$$w = \overline{W}(r) + w'(r, \theta, z, t) \tag{8}$$

$$p = \overline{P}(r) + p'(r, \theta, z, t) \tag{9}$$

It should be noted that the mean flow, i.e., $\overline{V}$, $\overline{W}$, and $\overline{P}$, must satify the governing equations (1) through (4). Therefore, if equations (6) through (9) are introduced into equations (1) through (4), and the mean flow subtracted from these, one obtains:

the continuity disturbance equation,

$$\frac{\partial u'}{\partial r} + \frac{u'}{r} + \frac{1}{r}\frac{\partial v'}{\partial \theta} + \frac{\partial w'}{\partial z} = 0 \qquad (10)$$

the r-momentum disturbance equation,

$$\frac{\partial u'}{\partial t} + u'\frac{\partial u'}{\partial r} + \frac{1}{r}\left(\overline{V}\frac{\partial u'}{\partial \theta} + v'\frac{\partial u'}{\partial \theta}\right) + \left(\overline{W}\frac{\partial u'}{\partial z} + w'\frac{\partial \overline{W}}{\partial z} + w'\frac{\partial w'}{\partial z}\right)$$

$$- 2\frac{\overline{V}v'}{r} + \frac{v'^2}{r} = -\frac{1}{\rho}\frac{\partial p'}{\partial r} \qquad (11)$$

the θ-momentum disturbance equation,

$$\frac{\partial v'}{\partial t} + u'\frac{\partial \overline{V}}{\partial r} + u'\frac{\partial v'}{\partial r} + \frac{\overline{V}}{r}\frac{\partial v'}{\partial \theta} + \frac{v'}{r}\frac{\partial \overline{V}}{\partial \theta} + \frac{v'}{r}\frac{\partial v'}{\partial \theta} + \overline{W}\frac{\partial v'}{\partial z}$$

$$+ w'\frac{\partial \overline{V}}{\partial z} + w'\frac{\partial v'}{\partial z} + \frac{\overline{V}u'}{r} + \frac{u'v'}{r} = -\frac{1}{\rho r}\frac{\partial p'}{\partial \theta} \qquad (12)$$

and the z-momentum disturbance equation,

$$\frac{\partial w'}{\partial t} + u'\frac{\partial \overline{W}}{\partial r} + u'\frac{\partial w'}{\partial r} + \frac{\overline{V}}{r}\frac{\partial w'}{\partial \theta} + \frac{v'}{r}\frac{\partial \overline{W}}{\partial \theta} + \frac{v'}{r}\frac{\partial w'}{\partial \theta} + \overline{W}\frac{\partial w'}{\partial z}$$

$$+ w'\frac{\partial \overline{W}}{\partial z} + w'\frac{\partial w'}{\partial z} = -\frac{1}{\rho}\frac{\partial p'}{\partial z} \qquad (13)$$

In equations (10) through (13), the product terms such as $u' \cdot \frac{u'}{r}$ correspond to the effect of one fluctuation on another. Retention of these product terms prohibits an easy solution to the equations. However, these difficulties are eliminated by assuming that the fluctuations and their derivatives have small amplitudes with respect to mean flow quanti-ties. This, indeed, is a reasonable assumption and will be invoked. Thus all products and powers (higher than the first) of the fluctuations are neglected and only those terms which are linear in them are retained. This procedure of linearization leads to the following linearized equations:

r-momentum:

$$\frac{\partial u'}{\partial t} + \frac{\overline{V}}{r} \frac{\partial u'}{\partial \theta} + W \frac{\partial u'}{\partial z} + w' \frac{\partial \overline{W}}{\partial \theta} - 2 \frac{\overline{V} v'}{r} = - \frac{1}{\rho} \frac{\partial p'}{\partial r} \tag{14}$$

θ-momentum:

$$\frac{\partial v'}{\partial t} + u' \frac{\partial \overline{V}}{\partial r} + \frac{\overline{V}}{r} \frac{\partial v'}{\partial \theta} + \frac{v'}{r} \frac{\partial \overline{V}}{\partial \theta} + \overline{W} \frac{\partial v'}{\partial z} + w' \frac{\partial \overline{V}}{\partial z} + \frac{\overline{V} u'}{r}$$

$$= - \frac{1}{\rho r} \frac{\partial p'}{\partial \theta} \tag{15}$$

z-momentum:

$$\frac{\partial w'}{\partial t} + u' \frac{\partial \overline{W}}{\partial r} + \frac{\overline{V}}{r} \frac{\partial w'}{\partial \theta} + \frac{v'}{r} \frac{\partial \overline{W}}{\partial \theta} + \overline{W} \frac{\partial w'}{\partial z} + w' \frac{\partial \overline{W}}{\partial z} = - \frac{1}{\rho} \frac{\partial p'}{\partial z} \tag{16}$$

For simplicity, the axial mean flow $\overline{W}$ is assumed to be a constant, and since the mean flow in the θ-direction is a function of radius only, the above continuity and momentum disturbance equations can then be written as the continuity disturbance equation [eq. (10)], as well as the r-momentum disturbance equation,

$$\frac{\partial u'}{\partial t} + \frac{\overline{V}}{r} \frac{\partial u'}{\partial \theta} + \overline{W} \frac{\partial u'}{\partial z} - 2 \frac{\overline{V} u'}{r} = - \frac{1}{\rho} \frac{\partial p'}{\partial r} \tag{17}$$

the θ-momentum disturbance equation,

$$\frac{\partial v'}{\partial t} + u' \frac{\partial \overline{V}}{\partial r} + \frac{\overline{V}}{r} \frac{\partial v'}{\partial \theta} + \overline{W} \frac{\partial v'}{\partial z} + \frac{\overline{V} u'}{r} = - \frac{1}{\rho r} \frac{\partial p'}{\partial \theta} \tag{18}$$

and the z-momentum disturbance equation,

$$\frac{\partial w'}{\partial t} + \frac{\overline{V}}{r} \frac{\partial w'}{\partial \theta} + \overline{W} \frac{\partial w'}{\partial z} = - \frac{1}{\rho} \frac{\partial p'}{\partial z} \tag{19}$$

14

Finally, the linearity of equations (10) and (17) to (19) enables one to obtain periodic solutions in terms of complex functions. Thus the system of partial differential equations (10), (17), (18), and (19) can be converted into ordinary differential equations.

The various parameters describing the perturbation have a (z, θ, t)-dependence assumed to be given by

$$e^{i(kz + n\theta - \omega t)} \tag{20}$$

where k is the wavenumber of the disturbance in the z-direction, n is an integer (which can only be positive, zero or negative), and ω is a constant (which can be complex). In this analysis, k is assumed a real number and ω a complex number that will be determined later. Furthermore, if $f(r)$, $g(r)$, $h(r)$, and $q(r)$ were to denote the amplitudes of the respective perturbations u', v', w' and p' whose (z, θ, t)-dependence is governed by equation (20), then one could expect to find solutions of the type:

$$\hat{u}' = i\, f(r)\, e^{i(kz + n\theta - \omega t)} \tag{21}$$

$$\hat{v}' = g(r)\, e^{i(kz + n\theta - \omega t)} \tag{22}$$

$$\hat{w}' = h(r)\, e^{i(kz + n\theta - \omega t)} \tag{23}$$

and

$$\hat{p}' = q(r)\, e^{i(kz + n\theta - \omega t)} \tag{24}$$

The superscript $^\wedge$ denotes a preliminary complex solution which ultimately leads to a real solution. In other words, one can obtain a set of solutions which are the complex conjugates of the preliminary solutions. The pure real solutions can then be constructed as follows:

$$u' = 1/2\, (\hat{u}' + \hat{u}*') \tag{25}$$

$$v' = 1/2\, (\hat{v}' + \hat{v}*') \tag{26}$$

$$w' = 1/2 \ (\hat{w}' + \hat{w}*') \tag{27}$$

and

$$p' = 1/2 \ (\hat{p}' + \hat{p}*') \tag{28}$$

where the superscript * denotes a conjugate of the preliminary solution.

Substituting equations (21) through (24) into equations (10), (17), (18) and (19), and cancelling the common expression, $\exp [i(kz + n\theta - \omega t)]$, one obtains the following:

the continuity equation,

$$\frac{df}{dr} + \frac{f}{r} \frac{n}{r} g + k h = 0 \tag{29}$$

the r-momentum equation,

$$\left(\omega - \frac{n}{r} \overline{V} - k \overline{W}\right) f - 2 \frac{\overline{V}}{r} g = - \frac{1}{\rho} \frac{dq}{dr} \tag{30}$$

the θ-momentum equation,

$$\left(\frac{d\overline{V}}{dr} + \frac{\overline{V}}{r}\right) f + \left(n \frac{\overline{V}}{r} - \omega + k \overline{W}\right) g = - \frac{n}{\rho r} q \tag{31}$$

and the z-momentum equation,

$$\left(n \frac{\overline{V}}{r} - \omega + k \overline{W}\right) h = - \frac{k}{\rho} q \tag{32}$$

Since the flow at the section of radius R is a forced vortex or solid body rotation, the mean flow velocity in θ-direction $\overline{V}$ can be written as

$$\overline{V} = r \omega_o \tag{33}$$

16

where ω_o is the upstream fluid angular velocity. However, with

$$\frac{d\bar{V}}{dr} + \frac{\bar{V}}{r} = 2\,\omega_o \qquad (34)$$

and the axial mean flow velocity $\bar{W}$ considered a constant W_c, equations (29) through (32) become:

continuity:

$$\frac{df}{dr} + \frac{f}{r} + \frac{n}{r}\,g + k\,h = 0 \qquad (35)$$

r-momentum:

$$(\omega - n\,\omega_o - k\,W_c)\,f - 2\,\omega_o\,g = -\frac{1}{\rho}\frac{dq}{dr} \qquad (36)$$

θ-momentum:

$$2\,\omega_o\,f - (\omega - n\,\omega_o - k\,W_c)\,g = -\frac{n}{\rho r}\,q \qquad (37)$$

z-momentum:

$$(\omega - n\,\omega_o - k\,W_c)\,h = \frac{k}{\rho}\,q \qquad (38)$$

It can be shown from equations (35) to (38) that

$$f(r)\,\frac{k}{K}\,\left\{\frac{dh}{dr} - \frac{2\,n\,\omega_o}{\omega - n\,\omega_o - k\,W_c}\,\frac{h}{r}\right\} \qquad (39)$$

where the parameter K, a function of (k, ω), is defined as

$$K^2 = \left(\frac{k^2\left[4\,\omega_o^2 - (\omega - n\,\omega_o - k\,W_c)^2\right]}{(\omega - n\,\omega_o - k\,W_c)^2}\right) \qquad (40)$$

17

Substituting equation (39) into equation (36) yields the following expression for g:

$$g(r) = \frac{k}{K^2}\left[\left(1 + \frac{K^2}{k^2}\right)\frac{\omega - n\,\omega_o - k\,W_c}{2\,\omega_o}\frac{h}{r} - n\frac{h}{r}\right] \tag{41}$$

It is interesting to observe that equations (39), (40) and (41) are exactly the same as Suzuki's equations (197), (198) and (198') (ref. 16).

Substituting equations (39) and (41) into the continuity equation (35) produces the following Bessel's equation of order n in cylindrical coordinates

$$\frac{d^2h}{dr^2} + \frac{1}{r}\frac{h}{r} + \left(K^2 - \frac{h^2}{r^2}\right)h = 0 \tag{42}$$

The general solution of this equation is of the form

$$h(r) = c_1 J_n(rK) + c_2 Y_n(rK) \tag{43}$$

where c_1 and c_2 are arbitrary constants. It should be noted that in the above development no restrictions were necessary and therefore the analysis should be simpler and less restrictive.

Because the value Y_n tends to infinity as r approaches zero, it is necessary to force the constant c_2 to zero. Equation (43) then becomes

$$h(r) = c_1 J_n(rK) \tag{44}$$

The wall boundary condition stipulates no radial velocity, i.e.,

$$f(r) = 0 \text{ at } r = R$$

Hence from equations (39) and (44) one obtains

$$f(r = R) = 0 = \frac{k}{K^2}\left\{\frac{d}{dr}\left[c_1 J_n(rK)\right] - \frac{2n\,\omega_o}{\omega - n\,\omega_o - Kw_c}\right.$$

$$\left.\cdot\,\frac{c_1 J_n(rK)}{r}\right\} r = R \qquad (45)$$

Evaluation of the derivative of the Bessel function

$$\frac{dJ_n(rK)}{dr} = K\left[J_{n-1}(rK) - \frac{n}{rK} J_n(rK)\right] \qquad (46)$$

and inclusion in equation (45) produces

$$\frac{c_1 K}{K^2}\left[K J_{n-1}(RK) - \frac{n}{R} J_n(RK) - \frac{2n\,\omega_o}{(\omega - n\,\omega_o - kW_c)R} J_n(RK)\right] = 0 \quad (47)$$

From equation (40), however, it can readily be shown that

$$\omega = \left[n + \frac{2}{1 + K^2 (K^{-2})}\right]\,\omega_o + k\,W_c \qquad (48)$$

It should be noted that, if $k = 0$, equation (47) is automatically satisfied, and equation (48) becomes

$$\omega = n\,\omega_o \qquad (49)$$

This shows that the angular velocity ω is linearly related to the constant upstream fluid angular velocity ω_o. The angular velocity ω can be simply related to the sound frequency as $\omega = 2\,\pi\,F$, where F is the frequency response in kHz. The upstream fluid angular velocity ω_o is in reality another form of the true airspeed which can be derived easily. Therefore, equation (49) indicates that the vortex whistle frequency response is linearly proportional to the true airspeed for $K = 0$.

If, however, k is not equal to zero, and since c_1 cannot be zero, then the bracketed quantity of equation (47) must be zero, or

$$K J_{n-1}(RK) - \frac{n}{R}\left(1 + \frac{2\omega_o}{\omega - n\omega_o - kW_c}\right) J_n(RK) = 0 \qquad (50)$$

By rearranging equation (50), ω can be expressed as

$$\omega = c\,\omega_o + k\,W_c \qquad (51)$$

where

$$C = n + \frac{2}{\dfrac{RK}{n}\dfrac{J_{n-1}(RK)}{J_n(RK)} - 1} \qquad (52)$$

Equation (51), therefore, is the desired general solution showing a linear relation between the frequency response of the vortex whistle and true airspeed. This, however, is only the situation as long as the values of the parameters ω_o, k, W_c, α, and K are known.

Although equation (51) appears simple, the complex values for angular velocity ω and parameter K must be recognized. For this reason it is difficult to obtain a quantitative solution. Fortunately, a numerical procedure (described in Appendix A) can be used to obtain the desired solution. The derivations of the expression for the upstream fluid angular velocity ω_o as well as the constant mean axial velocity W_c are included in Appendix B.

NUMERICAL RESULTS AND DISCUSSION

Introduction

It has been suggested and subsequently theoretically proven that the sensor frequency response is linearly proportional to the airspeed under various conditions. The different combinations of vortex tubes and swirlers used are tabulated in table 1. The results from computer calculations will be presented later. The quantitative results which are derived in Appendix A prove that the analytic theory works well for all combinations of vortex tubes and swirlers tested in the current work. It should be noted that the procedure of calculation presented applies only to those geometries similar to the ones discussed in this study. For other designs the procedure of calculation would have to be modified. The quantitative results and discussions of the theoretical work are summarized below.

Relationship Between Flow Rate and Frequency Response

Basically, the flow rate versus frequency response has the same relationship as airspeed versus frequency response, i.e., the flow rate is linearly proportional to the frequency response. For the swirlers with the same exit angle but different flutes, the theoretical frequency responses are the same, as shown in figures 2 to 9. Under the specified condition and configuration, the frequency response changes dramatically as the cross-sectional size of the precessional flow region changes. For example, the frequency response for sensor 2 is approximately 3.5 times greater than that of sensor 1. The frequency response is higher with larger exit angle swirlers. It is expected that these sensors can be utilized as an instrument for measurement of flow rates in the industrial and research areas.

Effect of Exit Angle on Swirler

In general, under the same conditions, the higher the exit angle, the higher the frequency response will be. This is true because at higher exit angles the tangential component of flow is higher. The higher exit angles generate higher angular velocities or revolutions

which in turn produce higher frequencies. A comparison of the results is presented in figures 10 to 30.

Effect of Wavenumber

The results for sensor 1 with wavenumbers one, three, five and seven are shown in figures 12 to 15, respectively. A comparison of the results for each shows no difference, which proves that the frequency response does not depend on the wavenumber. This also indicates that assuming a wavenumber of one when computing the results is justified.

Effect of Flutes on Swirler

The effect of flutes imposed on the swirler is shown in figures 31 to 36. As the number of flutes on the swirler is increased, the intake flow decreases, as does the frequency response. For the same frequency, the airspeed sensor designed as a 4-flute swirler needs approximately 12 percent more flow or speed than that of a 2-flute swirler. Although the two-flute swirler would be more economical, the decision as to how many flutes the swirler should have should be determined from both design and performance criteria.

Effect of Swirler Core Size D_2

As observed from figures 12, 21, and 27, the frequency response is higher in the small core size of swirler. Specifically, the frequency response for the 1.588- and 1.524-cm core size swirlers is much lower than for the 0.953-cm swirler. (See table 1 for the dimensions of each configuration.) In the experiments for the 0.953-cm core diameter swirler with 3 flutes whose exit angles are each 45 degrees, a whistle was generated. As mentioned in reference 41, some swirlers would not generate a distinct whistle as expected. The ideal range for the swirler core size D_2 when expressed in terms of the ratio of D_2/D_1 is between 0.81 and 0.67.

Effect of Cross-Sectional Size of
the Precessional Flow Region

The cross-sectional size of the precessional flow region proved to be a significant parameter in the design of the vortex tube. The frequency responses were much higher for the smaller diameter precessional flow regions. Figures 37 to 39 clearly show that much higher frequency responses occurred in sensors 2, 4, and 6 than were experienced in sensors 1, 3 and 5, respectively. (Again, refer to table 1 and fig. 1 for dimensions of sensors 1 through 6.) The 0.635-cm diameter precessional flow region produced a frequency response approximately 3 times that of the 0.953-cm one. It should be noted that the diameter size of the precessional flow region can be adjusted to obtain a desired frequency response range.

Relationship Between the Mean Axial Velocity W_c and Airspeed

From equation (B10), Appendix B, it is concluded that the mean axial velocity W_c is linearly related to the airspeed. Theoretical data for different indicators are plotted in figures 40 to 45. The theoretical results show the mean axial velocity for the higher exit angle swirlers to be less than for the smaller exit angle swirlers. Figure 46 reveals the frequency response to be linearly proportional to the mean axial velocity.

Relationship Between Reynolds Number and Strouhal Number

Both Reynolds number Re and Strouhal number St are defined in terms of the axial velocity W_c and diameter of precessional flow region D_3. Except for the singular point at zero airspeed, the predicted Strouhal numbers remained constant as the airspeed was increased. (Note that, for a given exit angle, the Strouhal number is a constant regardless of the number of flutes in the swirler.) The data for six different indicators are plotted in figures 47 to 52. When the sensors with the same swirler exit angles are compared, one finds the Strouhal numbers are the same. Therefore it is reasonable to conclude that the Strouhal number is dependent only on α, the swirler exit angle. The approximate values of Strouhal number for 45°, 60°, and 75° swirlers are 0.51, 0.88, and 1.88, respectively.

APPARATUS AND TESTS

General Description

In order to understand the operation and performance of the true airspeed sensor, visualization, closed-conduit and wind-tunnel tests were undertaken. The purpose of the visualization test was to carefully examine the fluid flow phenomenon-precession and observe how the flow velocity affects the precessional motion. Another objective was to observe and locate a suitable position for picking up the signal. The closed-conduit test (flow rate versus frequency response) provided information as to how the flow rate could be related to the frequency response. These sensors can certainly be compared with commercially available flow meters. Finally, the wind-tunnel test or actual flight test was conducted to supply the actual data for the relationship between the true airspeed and the frequency response. It is anticipated that additional research will be undertaken to improve the design of the sensor in the latter two stages. A complete description of the sensor setup and test procedures follows.

Visualization

In the early stages of investigation, a water model apparatus was set up for observing the fluid flow phenomenon-precession. The descriptions of vortex tube geometry and experimental arrangement are shown in figures 53 and 54. In figure 53, sections I and II, which were made of brass, were used for generating the swirling flow. Axial flow was injected at section I while eight tangential jet flows were brought into the stream at section II. Both the axial and tangential flows were regulated by separate valves to produce the desired swirling flow pattern. To provide the necessary space for the occurrence of precessional flow, section III was made of transparent Plexiglas and constructed as a Venturi-like converging-diverging nozzle. Small air bubbles were brought into the main stream from the tangential flow inlet. The air bubbles collected in the lowest pressure region. The movement of the low-pressure air bubble stream revealed the precessional flow for some definite flow rate. It was clearly shown that, the higher the flow rate, the higher would be the number

of revolutions of the air bubble stream about the axis of the tube. For investigation and observation purposes, four rolls of high-speed movies and some slides were taken from different angles. Some of the pictures are shown in figures 55 and 56. The pictures clearly demonstrate that the precessional flow whirled around as it left the central part or as it entered the enlargement (divergement) section.

Closed-Conduit Test

There are many different types of gas flow meters currently in use. Some of the meters make use of either the vortex shedding principle or the vortex precession principle. Such meters are usually used for low flow rates. The indicator designed during this project could also be considered as a potential flow meter. It was therefore considered desirable to investigate the relationships between the flow rate and the frequency response. It was also anticipated that the results from this test could be compared with data from wind-tunnel tests.

The initial designs for the vortex tubes and swirlers are shown in figures 57 to 59. The vortex tube in figure 58 was used to investigate the effect of the enlargement exit section wall and to note whether a gradual or abrupt enlargement made any difference. Swirlers with 4 flutes and with 45°, 60°, or 75° exit angles were considered. The vortex tubes were made of Plexiglas while the swirlers were made of aluminum. The test apparatus is shown in figure 60. The VOL-O-FLO flow meter (product of National Laboratories Instrument Inc., Model 50) with 0.283 m^3 (10 ft^3) per minute capacity was used for the measurement of flow rate. The flow rate could be read and recorded through a voltmeter and converted to the equivalent flow rate unit, m^3/min. The sound or whistle signals were picked up by an electric condenser microphone and passed through an amplifier which was connected to either an oscilloscope or a frequency counter. The schematic diagram of the signal amplifier is shown in figure 61, and the electric condenser microphone used in this test is shown in figure 62. It is expected that the flow rate is also linearly proportional to the frequency response.

Wind-Tunnel Test

A small but well-designed wind tunnel was available for testing (see fig. 63). The test area is 15.24 cm by 15.24 cm (6 in. by 6 in). A honeycomb type screen, 2.54 cm by 2.54 cm grid, was placed in front of the tunnel in order to assure uniform flow at the test section. The speed was measured by a pitot-static tube which was aligned with the entrance plane of the vortex tube being tested. The frequency responses were also picked up by the electric condenser microphone. The arrangement is the same used in the closed-conduit test. Different combinations of vortex tubes and swirlers were arranged for testing and their dimensions are given in table 1.

EXPERIMENTAL RESULTS AND DISCUSSION

The experimental results, obtained from both the closed-conduit tests and the wind-tunnel tests, did reveal a linear relationship between the true airspeed/flow rate and the frequency response. All swirlers used in these tests had 4 flutes with an exit angle of either 45°, 60°, or 75°. The actual dimension h on the swirler shown in figure B-1 (Appendix B) is shown in figure 64. The comparison between the designed (used in the numerical calculations) and actual cross-sectional areas for flow passage at section A-A shown in figure B-2 is also shown in figure 65.

Past investigators had difficulty eliminating noise from the signal. During these tests it was discovered that the proper positioning of the microphone was critical in obtaining the desired frequency response. This inevitably resulted in eliminating noise interference and thus produced a stable and clean signal. This breakthrough made measurements possible. It was observed that a definite minimum airspeed value had to be reached first for the frequency response to be stable. This was because of the unstable precessional flow at low airspeeds as well as the low amplitude signals. The minimum airspeed value was obtained by either lifting or lowering the microphone. It was therefore necessary to maintain this microphone position for all measurements, as the signal would have otherwise deteriorated. The arrangement and position of the microphone is shown in figure 66. The results obtained from both the closed-conduit test and wind-tunnel test are shown and discussed as follows.

Closed-Conduit Test

The first step was to test the sensor with compressed air. The results for sensors 1 through 4 are shown in figures 67 to 70. The flow rate was recorded and calculated according to the calibration sheet provided with the flow meter used in this test. When calibrated at atmospheric pressure, the formula for flow rate is

$$Q = F_1 \cdot P$$

where Q is the flow rate of the air (ft^3/min), P is the differential
pressure (in. of water), and F_1 is the constant 5.23. The flow rate
Q is then converted to the metric system units.

As observed from the figures, the frequency response for each sensor
with different swirlers was linearly proportional to the flow rate over a
definite range. The working ranges for each sensor with a special swirler
are tabulated in table 2. It was noted that sensors 2 and 4 had wider
ranges of frequency response than did sensors 1 and 3. The minimum flow
rate for generating a stable signal was 0.009 m^3/min, and this occurred
in indicators 2 and 4 with an exit swirler angle of 75°. The minimum
frequency response picked up by the microphone was 0.70 kHz, and this was
observed in sensor 3, which had an exit swirler angle of either 45° or
60°. The maximum flow rate working linear range was noted to be 0.157
m^3/min, and this was observed with sensor 3 having an exit swirler angle
of 45°. As predicted in the numerical calculations, it was found that
the higher the exit swirler angle, the higher the frequency response that
occurred. The best performance among those sensors was for the one with
an exit swirler angle of 45°. In general, the sensors with the smaller
cross-sectional precessional flow areas had quicker responses at the lower
flow rates. This smaller cross-sectional precessional flow area produced
a more stable precessional flow and a more pronounced whistle. Below the
minimum flow rate, the signal was random and the noise level was high.
Beyond the maximum point, the frequency response declined. It will be
shown later that the working ranges listed in table 2 will indeed cover
the maximum desired airspeed of 321.9 km/hr.

Wind-Tunnel Test

Unlike the closed-conduit test, when a sensor was tested in the wind
tunnel, a much higher airspeed was needed to generate a stable frequency
response. Hence a modified model for the vortex tube was made (shown
in figure 71). A convergent nozzle was placed in front of the vortex
tube. This enabled the airspeed to reach a higher value at the entrance
to the vortex tube. When compared with the original sensor, this modified
model was able to generate a higher angular velocity and more stable
precessional flow. Also, a divergent nozzle was placed in the back of the

vortex tube in order to minimize the outside influence of the back flow region. Such an arrangement, another breakthrough, contributed to making measurements possible. A pitot-static tube was placed in front of the convergent nozzle to allow measurement of speed. It was anticipated that a stable frequency response was not possible until the minimum frequency response, as noted in the closed-conduit test with a specified sensor, was reached. Based on this test, the minimum airspeed to obtain a stable signal was 70 km/hr (43.5 mph).

Due to wind-tunnel limitations described in figure 63, only a few measurements were made. However, through correlation of flow rates, airspeeds, and frequency responses, additional data can be extrapolated to higher airspeeds. The combinations of test results for true airspeed, flow rate, and frequency response are shown in figures 72 to 83 for the individual sensors with a specified swirler. The procedure to obtain these figures is described in Appendix C.

It should be mentioned that, for a specified sensor and swirler, the working range for the closed-conduit test is also the working range for the wind-tunnel test. The frequency response is linearly proportional to the true airspeed. When the desired maximum airspeed of 321.9 km/hr (200 mph) is reached, the frequency response is still within the working range.

In figures 72 to 83, the converted, dimensional, numerical results are plotted for comparison. The converted numerical results were obtained by multiplying the theoretical results by the area ratio shown in figure 65. To avoid any misunderstanding two points should be mentioned. First, the numerical results were calculated assuming inviscid flow. In reality, the viscous effects were, however, significant. The deviations between the theory and experimental data are clearly evident, especially for sensors 2 and 4. Secondly, the pitot tube position for measuring the airspeed in the wind-tunnel test was not at the same location used in the numerical calculation. The actual airspeed at the entrance of the vortex tube was 1.84 times higher than that at the point of the converging nozzle. The experimental results for sensors 1 and 3 compare favorably with the numerical results when one follows the procedures and measurements recommended in this section. It was concluded that the analytical and

experimental results did prove that the frequency response was linearly proportional to the true airspeed, while quantitative agreement between theory and experiment was sufficiently good to allow theoretical prediction only for sensors 1 and 3.

SUMMARY AND CONCLUSION

An experimental and analytical study of a true airspeed sensor was undertaken. The results of the theoretical study proved to be successful, in that it was determined that the frequency response was linearly proportional to the airspeed. The performance was shown to be heavily dependent upon the design of the vortex tube and swirler geometries. The smaller the cross-sectional area in the precessional flow region, the more sensitive was the frequency response. The exit angle on the swirler also played a very important role in the performance of the sensor. The larger the exit swirler angle, the greater was the frequency response. It was also observed that as Reynolds number increased the Strouhal number remained constant. Moreover, it was noticed that the Strouhal numbers based on W_c were dependent only upon the exit swirler angles.

The experimental results revealed similar characteristics to those obtained through analysis. This true airspeed sensor has three unique characteristics: flow phenomenon-precession, vortex whistle, and no moving parts. It was also observed that the position of the microphone was critical. When the microphone was located close to the inner wall, a nondesirable random signal was created. On the other hand, when the microphone was placed too far from the inner wall, the capability of picking up a signal was reduced. Thus, the best microphone position was achieved by adjusting the position until a stable signal was obtained. By such a procedure it became possible to make the necessary measurements. The working ranges of the sensors were beyond the maximum airspeed required.

Due to the complexity of the problem, the analytical results are valid only for inviscid fluid flow. When compared with the experimental result, the deviations noted are belived to be mainly due to the viscous effects. Under the arrangement described under "EXPERIMENTAL RESULTS AND DISCUSSION," it was found that the experimental results were in agreement with the analytical results for sensors 1 and 3. Although for this project the minimum airspeed was 70 km/hr (43.5 mph), the minimum airspeed achievable could be lowered by placing a modified convergent nozzle in front of the vortex tube. By such a modification a stable signal could be detected even at lower airspeeds.

In conclusion, it was found that this true airspeed sensor has a linear relationship between frequency response and airspeed and is also independent of altitude. The sensor has proven to be reliable, capable of high accuracy, and one that could be easily fabricated and maintained. Such an insturment has proven to be desirable in measuring true airspeeds and flow rates.

ACKNOWLEDGMENTS

APPENDIX A

NUMERICAL ANALYSIS AND SOLUTIONS

Since equation (51) contains the precessional angular velocity ω, a complex number, and since the arguments of the Bessel functions are also complex, a quantitative solution of equation (51) is difficult to obtain. Therefore, an alternate method will be used to obtain the frequency response for a specified airspeed.

Throughout the following analysis all but one parameter will be assumed constant. Let ω_r and ω_i, respectively, represent the real and imaginary parts of the precessional angular velocity such that $\omega = \omega_r + i\omega_i$. When substituted into equation (20), one obtains

$$e^{i(kz + n\theta - \omega t)} = e^{\omega_i t} \cdot e^{i(kz + n\theta - \omega_r t)} \tag{A1}$$

As evident, for ω_i values greater than zero, the perturbation amplitude increases as ω_i increases. The objective of this analysis is to find the maximum value of ω_i for a specified velocity such that the corresponding ω_r will be the precessional angular velocity (or frequency) response desired. Equation (50) can be written in the following form:

$$\frac{J_{n-1}(RK)}{\partial_n (RK)} = \frac{n}{RK}\left(1 + \frac{2\omega_o}{\omega - n\omega_o - k W_c}\right) \tag{A2}$$

In equation (A2), n will be assigned the value one. The justification for this assumption is based on observations in the present work and results of Chanaud's work (ref. 17). Chanaud tested a vortex tube submerged in water. He injected air into the vortex tube to observe the air bubble flow pattern throughout. He noted the formation of a bubble line and that the line did not assume a helical form. This can be interpreted to imply that the perturbations are constant along a simple helix, which would be the case for n = 1 in equation (A2). Thus, provided parameters ω_o, W_c, k and R are known, equation (A2) becomes

$$\frac{J_o(RK)}{J_1(RK)} = \frac{1}{RK}\left(1 + \frac{2\,\omega_o}{\omega - \omega_o - k\,W_c}\right) \qquad \text{(A3)}$$

However, from equation (40) with $n = 1$, K can be written as

$$K = \frac{k\sqrt{4\,\omega_o^2 - (\omega - \omega_o - k\,W_c)^2}}{\omega - \omega_o - k\,W_c} \qquad \text{(A4)}$$

Substituting equation (A4) into equation (A3), the right-hand side (RHS) of equation (A3) becomes

$$RHS = \frac{1}{RK}\frac{\omega - \omega_o - k\,W_c}{\sqrt{4\,\omega_o^2 - (\omega - \omega_o - k\,W_c)^2}}\left(1 + \frac{2\,\omega_o}{\omega - \omega_o - k\,W_c}\right)$$

or

$$RHS = \frac{1}{RK}\frac{\omega - \omega_o - k\,W_c}{\sqrt{4\,\omega_o^2 - (\omega - \omega_o - k\,W_c)^2}} \qquad \text{(A5)}$$

The left-hand side (LHS) of equation (A3) is

$$LHS = \frac{J_o(RK)}{J_1(RK)}$$

and since

$$J_o(x) = 1 - \frac{x^2}{2^2(1!)^2} + \frac{x^4}{2^4(2!)^2} - \frac{x^6}{2^6(3!)^2} + - \ldots \qquad \text{(A6)}$$

and

$$J_1(x) = \frac{x}{2} - \frac{x^3}{2^3.1!.2!} + \frac{x^5}{2^5.!.3!} - \frac{x^7}{2^7.3!.4!} + - \ldots \qquad \text{(A7)}$$

the left-hand side of equation (A3) can be expressed approximately as

$$\text{LHS} \cong \frac{1 - \dfrac{(RK)^2}{2^2 (1!)^2} + \dfrac{(RK)^4}{2^4 (2!)^2} - \dfrac{(RK)^6}{2^6 (3!)^2}}{\dfrac{RK}{2} - \dfrac{(RK)^3}{2^3 (1!)(2!)} + \dfrac{(RK)^5}{2^5 (2!)(3!)}} \tag{A8}$$

An analysis of the errors due to replacing the exact expression by equation (A8) may be found in Appendix D.

Substituting equation (A4) into equation (A8) and simplifying, one obtains

$$\begin{aligned}
\text{LHS} \cong \Bigg\{ & (\omega - \omega_o - kW_c)^6 - \frac{R^2K^2}{4} \Big[4\,\omega_o^2 - (\omega - \omega_o - kW_c)^2 \Big] \\
& \times (\omega - \omega_o - k\,W_c)^4 + \frac{R^4K^4}{64} \Big[4\,\omega_o^2 - (\omega - \omega_o - kW_c)^2 \Big]^2 \\
& \times (\omega - \omega_o - kW_c)^2 - \frac{R^6K^6}{2304} \Big[4\,\omega_o^2 - (\omega - \omega_o - kW_c)^2 \Big]^3 \Bigg\} \\
\div \Bigg\{ & \frac{RK}{2} \Big[4\,\omega_o^2 - (\omega - \omega_o - kW_c)^2 \Big]^{1/2} (\omega - \omega_o - kW_c)^5 \\
& - \frac{R^3K^3}{16} \Big[4\,\omega_o^2 - (\omega - \omega_o - kW_c)^2 \Big]^{3/2} (\omega - \omega_o - kW_c)^3 \\
& + \frac{R^5K^5}{384} \big(4\,\omega_o^2 - (\omega - \omega_o - kW_c)^2 \big]^{5/2} (\omega - \omega_o - kW_c) \Bigg\}
\end{aligned} \tag{A9}$$

By introducing the following coefficients:

$$C_o = \omega_o + kW_c$$

$$C_1 = 4\,\omega_o^2 - C_o^2$$

$$C_2 = RK/2$$

$$C_3 = R^2K^2/4 = C_2^2 \tag{A10}$$
$$\text{(cont'd)}$$

$$C_4 = R^3 K^3/16 = C_2^3/2$$

$$C_5 = R^4 K^4/64 = C_2^4/4$$

$$C_6 = R^5 K^5/384 = C_2^5/12$$

$$C_7 = R^6 K^6/2304 = C_2^6/36$$

$$C_8 = \omega_o - k W_c \qquad \text{(A10)}$$
$$\text{(concl'd)}$$

equations (A9) and (A5) become, respectively,

$$
\begin{aligned}
\text{LHS} = & \left\{ (\omega - C_o)^6 - C_3(C_1 + 2C_o \omega - \omega^2)(\omega - C_o)^4 \right. \\
& \left. + C_5(C_1 + 2C_o \omega - \omega^2)^2 (\omega - C_o)^2 - C_7(C_1 + 2C_o \omega - \omega^2)^3 \right\} \\
& \div \left\{ C_2(\omega - C_o)^5 (C_1 + 2C_o \omega - \omega^2)^{1/2} - C_4(\omega - C_o)^3 \right. \\
& \left. \times (C_1 + 2C_o \omega - \omega^2)^{3/2} + C_6(\omega - C_o)(C_1 + 2C_o \omega - \omega^2)^{5/2} \right\} \qquad \text{(A11)}
\end{aligned}
$$

$$\text{RHS} = \frac{1}{2C_2} \frac{\omega + C_8}{(C_1 + 2C_o \omega - \omega^2)^{1/2}} \qquad \text{(A12)}$$

By equating equations (A11) and (A12) and multiplying both sides by $(C_1 + 2C_o \omega - \omega^2)^{1/2}$, one obtains

$$
\begin{aligned}
\frac{1}{2C_2}(\omega + C_8) = & \left\{ (\omega - C_o)^6 - C_3(C_1 + 2C_o \omega - \omega^2)(\omega - C_o)^4 \right. \\
& + C_5(C_1 + 2C_o \omega - \omega^2)^2 (\omega - C_o)^2 \\
& \left. - C_7(C_1 + 2C_o \omega - \omega^2)^3 \right\} \div \left\{ C_2(\omega - C_o)^5 \right. \\
& - C_4(\omega - C_o)^3 (C_1 + 2C_o \omega - \omega^2) \\
& \left. + C_6(\omega - C_o)(C_1 + 2C_o \omega - \omega^2)^2 \right\} \qquad \text{(A13)}
\end{aligned}
$$

Simplifying and rearranging according to the power of ω, one obtains

$$F(\omega) = C_{39}\,\omega^6 + C_{40}\,\omega^5 + C_{41}\,\omega^4 + C_{42}\,\omega^3 + C_{43}\,\omega^2$$

$$+ C_{44}\,\omega + C_{45} = 0 \qquad\qquad (A14)$$

where the intermediate C constants in the development are as follows:

$$C_9 = 9C_o^2 - C_1$$

$$C_{10} = 3C_o C_1 - 7\,C_o^3$$

$$C_{11} = 2C_o^4 - 3C_o^2 C_1$$

$$C_{12} = 8C_o^2 - 2C_1$$

$$C_{13} = 4C_o C_1 - 4C_o^3 + 2C_1$$

$$C_{14} = C_1^2 - 4C_o^2 C_1$$

$$C_{15} = 14C_o^2 - C_1$$

$$C_{16} = 4C_o C_1 - 16C_o^3$$

$$C_{17} = 9C_o^4 - 6C_o^2 C_1$$

$$C_{18} = 4C_o^3 C_1 - 2C_o^5$$

$$C_{19} = 9C_o^2 + 4C_o - 2C_1$$

$$C_{20} = 8C_o C_1 - 8C_o^2 - 4C_o^3$$

$$C_{21} = 4C_o^3 - 10C_o^2 C_1 + C_1^2$$

$$C_{22} = 4C_o^3 C_1 - 2C_o C_1^2$$

$$C_{23} = 12C_o^2 - 3C_1$$

$$C_{24} = 12C_o C_1 - 8C_o^3$$

$$C_{25} = 3C_1^2 - 12C_o^2 C_1$$

$$C_{26} = C_2 + C_4 + C_6$$

$$C_{27} = 1 + C_3 + C_5 + C_7$$

$$C_{28} = 10C_o^2C_2 + C_4C_9 + C_6C_{12}$$

$$C_{29} = 15C_o^2 + C_3C_{15} + C_5C_{19} + C_7C_{29}$$

$$C_{30} = 10C_o^3C_2 + C_4C_{10} + C_6C_{13} + 10C_o^2C_2C_8 + C_4C_8C_9 + C_6C_8C_{12}$$

$$C_{31} = 20C_o^3 - C_3C_{16} - C_5C_{20} - C_7C_{24}$$

$$C_{32} = 5C_o^4C_2 + C_4C_{11} + C_6C_{14} - 10C_o^3C_2C_8 + C_4C_8C_{10} + C_6C_8C_{13}$$

$$C_{33} = C_3C_{17} - 15C_o^4 - C_5C_{21} - C_7C_{25}$$

$$C_{34} = C_o^2C_4 - C_1C_6$$

$$C_{341} = C_o^4C_2(5C_8 - C_o)$$

$$C_{35} = C_4C_8C_{11} + C_6C_8C_{14}$$

$$C_{36} = 6C_o^5 - C_3C_{18} - C_5C_{22} + 6C_oC_1^2C_7$$

$$C_{37} = C_o^2C_4 - C_1C_6$$

$$C_{38} = -C_o^4 + C_o^2C_1C_3 - C_1^2C_5$$

$$CC = 1/C_2$$

$$C_{39} = \frac{CC}{2}C_{26} - C_{27}$$

$$C_{40} = \frac{CC}{2}C_{26}(C_8 - 5C_o) + 6C_oC_{27}$$

$$C_{41} = \frac{CC}{2}(C_{28} - 5C_oC_8C_{26}) - C_{29}$$

$$C_{42} = \frac{CC}{2}C_{30} + C_{31}$$

$$C_{43} = \frac{CC}{C}C_{32} + C_{33}$$

$$C_{44} = \frac{CC}{2}(C_oC_1C_{34} + C_{341} + C_{35}) + C_{36}$$

$$C_{45} = \frac{CC}{2}(C_oC_1C_8C_{37} - C_o^5C_2C_8) + C_o^2C_{38} + C_1^3C_7$$

Equation (51) has therefore been transformed to equation (A14), a sixth order polynomial in ω having real coefficients C_{39} through C_{45}. As stated earlier, for a specified airspeed, one desires the maximum value of ω_i among the six roots of the equation. The corresponding ω_r is the frequency response. The solution to equation (A14) will be obtained through use of a computer porgram available at NASA/LaRC. The subroutine of this program, named "RPOLY," is a simple program developed to determine the complex roots of an equation by a three-stage variable-shift technique (refs. 42, 43). The distinct advantage of this subroutine is that it does not require any initial estimates of the roots.

The derivation of expressions for the upstream fluid angular velocity ω_o and the constant mean axial flow velocity W_c is given in Appendix B. The computing procedure and sample programming are given in Appendix E.

APPENDIX B

DERIVATION OF THE UPSTREAM FLUID ANGULAR VELOCITY

ω_o AND THE CONSTANT MEAN AXIAL FLOW VELOCITY W_c

The values of the upstream fluid angular velocity ω_o and the downstream constant mean axial flow velocity W_c are strongly dependent upon the design of both the vortex tube and swirler flow generator. The derivation will be based on the parameters listed in table 1; however, prior to the derivation each parameter will be discussed separately.

The combination of vortex tube and swirler used in the analysis is shown in figure B-2. The cross-sectional view of A-A is shown in figure B-1. The net fluid passage area as shown in figure B-1 is

$$A_{net} = \frac{\pi}{4} (D_1^2 - D_2^2) - n_1 \, h \, \frac{D_1 - D_2}{2} \tag{B1}$$

where n_1 is the number of flutes in the swirler, and h is the width of each flute. It is apparent that the net area at section B-B is

$$B_{net} = \frac{\pi D_3^2}{4} \tag{B2}$$

The fluid velocity or airspeed U leaving section A-A at an angle of α, as shown below, is separated into axial and tangential velocities U_a and U_t respectively.

Due to the complexity in geometry, an accurate analysis is very difficult to obtain. Thus, an approximation which is close to reality will be derived.
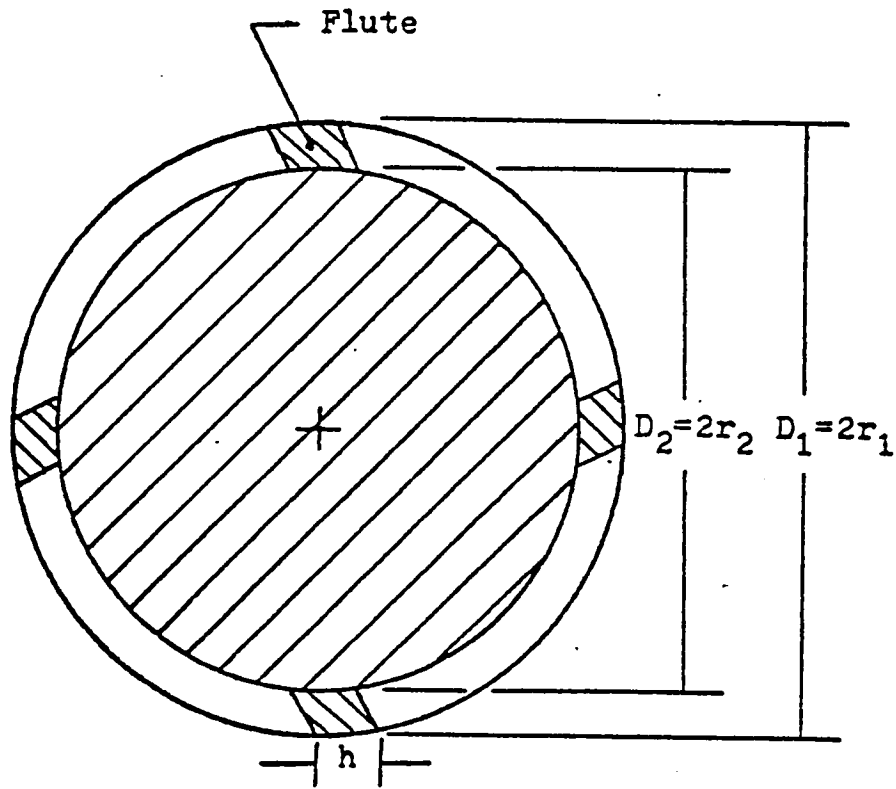
Figure B-1. Cross-sectional view of section A-A.
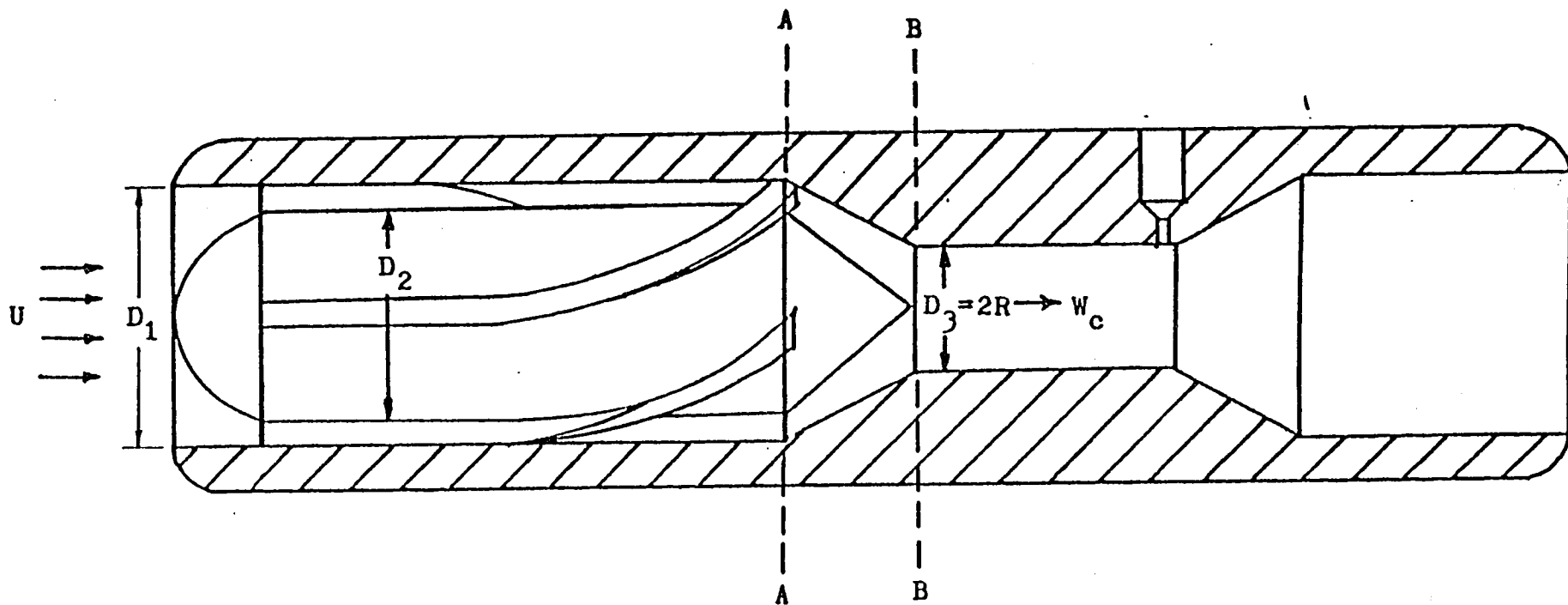
Figure B-2.   Cross-sectional view of vortex tube and swirler.

Since the fluid passage or gap between the vortex tube wall and swirler is so small, it is assumed here that the net area A_{net} at section A-A is replaced by a circular ring with the same outside radius r_1 but different inside radius, named equivalent radius $r_{e,2}$, which is larger than the original radius r_2. This equivalent radius $r_{e,2}$ will be determined first and then used later as a lower limit in the calculation of conservation of angular momentum at section A-A. Hence this circular ring will not include the cross-sectional areas of flutes. Thus, one can find this equivalent radius $r_{e,2}$ by equating the net area A_{net} with this new circular ring area as

$$A_{net} = \pi (r_1^2 - r_{e,2}^2)$$

or

$$r_{e,2} = \sqrt{r_1^2 - \frac{A_{net}}{\pi}} \qquad (B3)$$

where A_{net} was defined in equation (B1).

Due to the converging geometry between sections, the fluid angular velocity at section A-A is different from that at section B-B. The conservation of angular momentum can be expressed as

$$\int_{r_{e,2}}^{r_1} \omega_A \, r^2 \, dr = \int_0^R \omega_o \, r^2 \, dr \qquad (B4)$$

where ω_A and ω_o are constant fluid angular velocities at sections A-A and B-B, respectively.

In the forced vortex flow the tangential velocity is equal to the product of the constant angular velocity and the radius. Since the spacing between the core of the swirler and inner wall of the vortex tube is extremely small, the radius will be considered to be the average of r_1 and $r_{e,2}$. Thus, the constant angular velocity ω_A can be written as

44

$$\omega_A = \frac{U_t}{r_1 + r_{e,2}} \cdot \frac{1}{2}$$

or

$$\omega_A = \frac{2\ U \sin \alpha}{r_1 + r_{e,2}} \tag{B5}$$

Note, however, that $U_t = U \sin \alpha$. Therefore equation (B4) becomes

$$\int_{r_{e,2}}^{r_1} \frac{2\ U \sin \alpha}{r_1 + r_{e,2}}\ r^2\ dr = \int_0^R \omega_0\ r^2\ dr \tag{B6}$$

The value of the constant angular velocity ω_0 at section B-B can then be shown to be

$$\omega_0 = \frac{2\ U \sin \alpha}{R^3}\ \frac{r_1^3 - r_{e,2}^3}{r_1 - r_{e,2}} \tag{B7}$$

Hence, for a given airspeed U and swirler geometry there is one value for ω_0.

The downstream constant mean axial velocity W_c is obtained by considering the continuity of mass for sections A-A and B-B. The conservation of mass requires

$$U_a\ A_{net} = W_c\ B_{net} \tag{B8}$$

where ρ is constant, U_a is $U \cos \alpha$, and W_c is the constant mean axial velocity. Thus, the constant mean axial velocity W_c can be written as

$$W_c = U \cos \alpha\ \frac{A_{net}}{B_{net}} \tag{B9}$$

45

APPENDIX C

THE CONSTRUCTION OF FIGURES 72 THROUGH 83

The procedure for constructing the scales and data line of figures 72 through 83 is as follows:

1. Find the slope m of the data line in closed-conduit test results.

2. (A) If the data line goes through the origin, as in (a), figure C-1, calculate the reciprocal of the slope and obtain the scale for flow rate per unit frequency response, i.e. $(m^3/min)/kHz$.

    (B) If the data line does not go through the origin, as in (b), figure C-1, calculate the reciprocal of the slope and obtain the scale for flow rate per unit frequency response. Then use the following form to mark the scale for flow rate:

$$Q = \frac{1}{m} F + S \qquad\qquad (C1)$$

3. Mark the scale of the frequency response F on the left-hand side of the figure. Mark also the scale of the true airspeed U on the bottom of the figure, as shown in figure C-2.

4. (A) If the data line mentioned in step 2 goes through the origin, mark the scale of the flow rate on the right-hand side of the figure with zero m^3/min at bottom line, as in (a), figure C-2.

    (B) If the data line mentioned in step 2 does not go through the origin, mark the bottom line with the value of S and the corresponding scales based on equation C-1, as in (b), figure C-2.

5. Find the slope of the data line taken from the wind-tunnel test, then calculate the reciprocal of the slope to obtain the value of airspeed per unit frequency response F_r.

6. Find the intersection of one kHz and the value F_r from step 5.

7. Draw the line which connects the origin and the intersection found in step 6. This line represents the desired relationship among true airspeed, flow rate, and frequency response, as shown in figure C-3.

F

m

ΔF

ΔQ

Q

$m = \Delta F / \Delta Q$

(a)

F

m

ΔF

ΔQ

S

Q
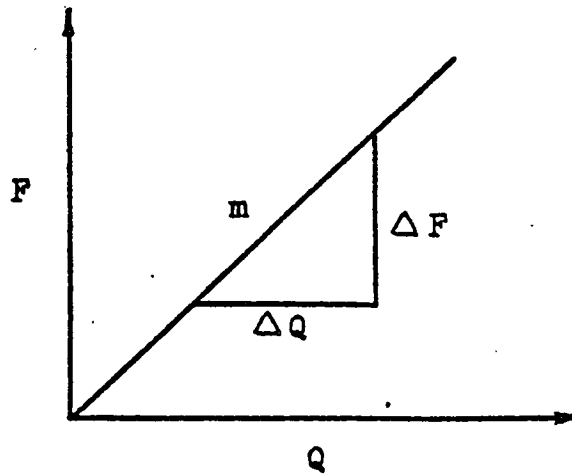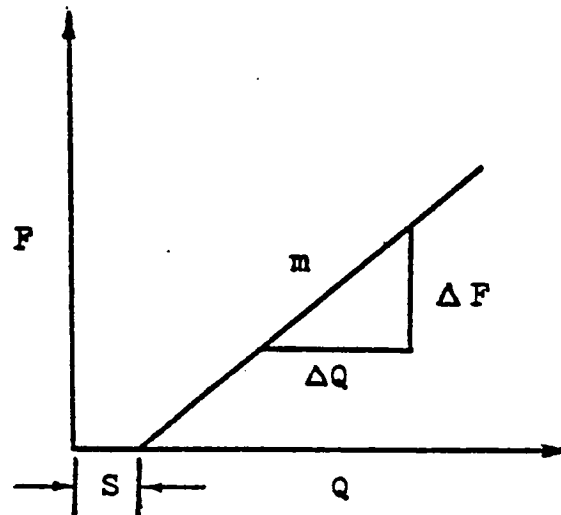
(b)

Figure C-1. Types of data line taken at closed-conduit test.
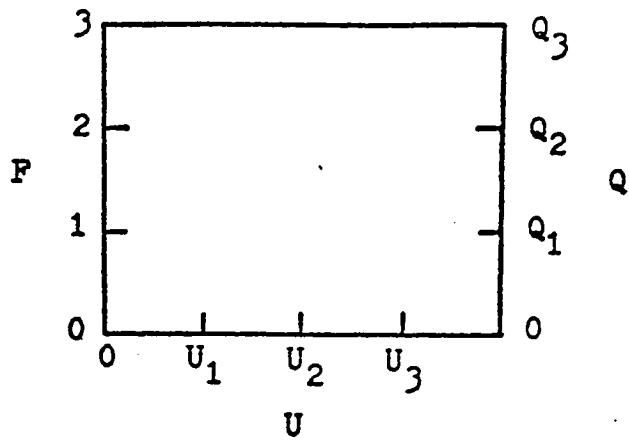
(a)
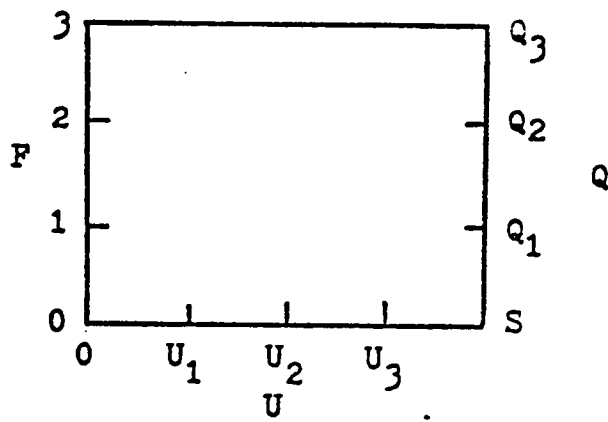
(b)

Figure C-2. The scales for flow rate at right-hand side.
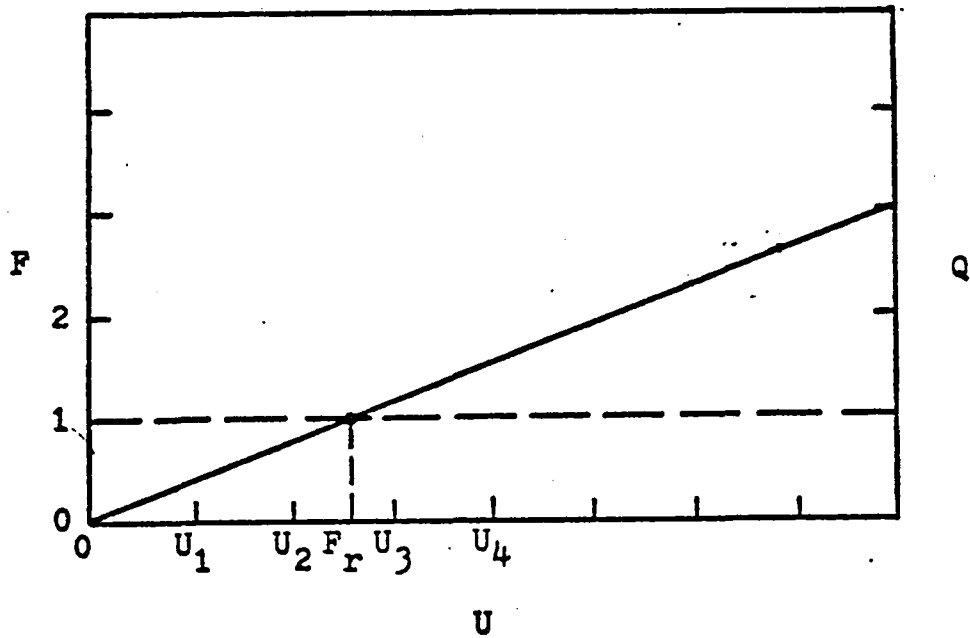
Figure C-3.   The performance line of a specific sensor.

APPENDIX D

ERROR ANALYSIS

In order to effectively compare the theoretical, numerical, and experimental results, an error analysis was undertaken. Throughout this research endeavor and, in particular in the development of the theoretical aspects of the problem, it became evident that certain simplifications would be necessary. As a result of these simplifications errors might have possibly been introduced.

The deviation of the theoretical from the experimental results, due to neglecting viscous effects in the development of the theory, has already been discussed (see "EXPERIMENTAL RESULTS AND DISCUSSION"). It is believed that the viscous effects caused the most significant deviation of theoretical results from the experimental data. In the derivation of the upstream fluid angular velocity ω_o and the constant downstream mean axial velocity W_c, as presented in Appendix B, the error introduced is considered insignificant. The complexity of the flow pattern between sections A-A and B-B rendered a quantitative error analysis virtually impossible. The derivations, however, were believed to be close enough to reality that errors could be considered extremely small compared with the overall performance features.

The most significant errors were found in the derivation of equation (A14), where the Bessel functions J_o and J_1 were evaluated on the basis of equations (A6) and (A7). It is however, very difficult to solve the problem, as both arguments of J_o and J_1 are complex numbers. In equation (A8), J_o took into consideration the first four terms of equation (A6), whereas J_1 took into consideration the first three terms of equation (A7).

We will now investigate the errors introduced from the elimination of the higher terms in the Bessel functions J_o and J_1. The actual values of J_o and J_1 will be calculated by calling the subroutine COMBES provided by NASA/LaRC. This subroutine COMBES is the only known source available for computing the Bessel functions $J_w(z)$ and $Y_w(z)$ for

complex orders and arguments. Note that the convergence of equations (A6) and (A7) is premised on the absolute value of the argument of the Bessel functions being less than one. The argument of the Bessel function will be derived first and evaluated before proceeding with the derivation.

It is necessary to first determine the real and imaginary expressions for the argument RK. Rewriting equation (40) gives

$$K = \frac{k\sqrt{4\,\omega_o^2 - (\omega - n\,\omega_o - kW_c)^2}}{\omega - \omega_o - kW_c} \tag{D1}$$

then the expression for RK becomes

$$RK = RK\sqrt{\frac{4\,\omega_o - (n\,\omega_o + kW_c)^2 + 2(n\,\omega_o + kW_c)\,\omega - \omega^2}{\omega - (n\,\omega_o + kW_c)}} \tag{D2}$$

Let $A_1 = n\,\omega_o + kW_c$, $A_2 = 4\,\omega_o^2 - A_1^2$ and $A_3 = RK$, and substitute into equation (D2), which then becomes

$$RK = A_3\sqrt{\frac{A_2 + 2A_1\,\omega - \omega^2}{\omega - A_1}} \tag{D3}$$

Now assume

$$\omega = \omega_r + i\,\omega_i \tag{D4}$$

where ω_r and ω_i are the real and imaginary parts of precessional angular velocity, respectively.

Now substitute equation (D4) into equation (D5) and let

$$A_4 = A_3/[(\omega_r - A_1)^2 + \omega_i^2] \tag{D5}$$

$$A_5 = A_2 + 2A_1\,\omega_r - \omega_r^2 + \omega_i^2 \tag{D6}$$

$$A_6 = 2A_1\,\omega_i - 2\,\omega_r\omega_i \tag{D7}$$

54

$$A_7 = \omega_r - A_1 \tag{D9}$$

One then obtains

$$RK = A_4 \left[(A_7 - i \omega_i)(A_5 + i A_6)^{1/2} \right] \tag{D9}$$

However, it is desirable to convert the expression $(A_5 + i A_6)^{1/2}$ into a simple $X + i Y$ form, where X and Y are real numbers, so that the argument RK can be rearranged into a convenient form for later use. Noting that Z^α can be expressed as

$$Z^\alpha = e^{\ln(Z)^\alpha} = e^{\alpha \ln(Z)} = e^{\alpha[\ln(Z) + i(\theta_1 + 2m\pi)]} \tag{D10}$$

where $Z = x + i y$, α is either a constant or a complex number, $|Z| = (x^2 + y^2)^{1/2}$, and θ_1 is the principle value of angle defined by $\theta_1 = \tan^{-1}(y/x)$. An appropriate selection of θ_1 allows $(A_5 + iA_6)^{1/2}$ to be written as

$$(A_5 + iA_6)^{1/2} = e^{1/2}[\ln(A_5^2 + A_6^2)^{1/2} + i \theta_1] \tag{D11}$$

where $\theta_1 = \tan^{-1}(A_6/A_5)$, or

$$(A_5 + iA_6)^{1/2} = (A_5 + A_6)^{1/4} (\cos \frac{\theta_1}{2} + i \sin \frac{\theta_1}{2}) \tag{D12}$$

Again let

$$A_8 = (A_5^2 + A_6^2)^{1/4} \tag{D13}$$

$$A_9 = A_7 \cos \frac{\theta_1}{2} + \omega_i \sin \frac{\theta_1}{2} \tag{D14}$$

$$A_{10} = A_7 \sin \frac{\theta_1}{2} - \omega_i \cos \frac{\theta_1}{2} \tag{D15}$$

$$A_{11} = A_4 A_8 A_9 \tag{D16}$$

$$A_{12} = A_4 A_8 A_{10} \tag{D17}$$

then equation (D9) becomes

$$RK = A_{11} + i A_{12} \qquad \text{(D18)}$$

where the constants A_{11} and A_{12} are real and imaginary parts of the argument. The subroutine COMBES can then be used to evaluate the actual values of Bessel functions J_O and J_1 for each argument of RK.

Now, substituting equation (D18) into equations (A6) and (A7), one obtains

$$J_O(RK) \cong 1 - 1/4 \; (A_{11} + i A_{12})^2 + \frac{1}{64} \; (A_{11} + i A_{12})^4$$

$$- \frac{1}{2304} \; (A_{11} + i A_{12})^6 \qquad \text{(D19)}$$

and

$$J_1(RK) \cong 1/2 \; (A_{11} + i A_{12}) - \frac{1}{16} \; (A_{11} + A_{12})^3$$

$$+ \frac{1}{384} \; (A_{11} + i A_{12})^5 \qquad \text{(D20)}$$

Expanding the power series, simplifying and separating the real and imaginary parts, $J_O(RK)$ becomes

$$J_O(RK) \cong [1 - 1/4 \; (A_{11}^2 - A_{12}^2) + \frac{1}{64} \; (A_{11}^4 - 6A_{11}^2 A_{12}^2 + A_{12}^4)$$

$$- \frac{1}{2304} \; (A_{11}^6 - 15A_{11}^4 A_{12}^2 + 15A_{11}^2 A_{12}^4 - A_{12}^6)]$$

$$+ i \; [- 1/2A_{11} A_{12} + \frac{1}{64} \; (4A_{11}^3 A_{12} - 4A_{11} A_{12}^3)$$

$$- \frac{1}{2304} \; (6A_{11}^5 A_{12} - 20A_{11}^3 A_{12}^3 + 6A_{11}A_{12}^5)] \qquad \text{(D21)}$$

and $J_1(RK)$ becomes

$$J_1(RK) \cong \left[\frac{1}{2} A_{11} - \frac{1}{16}(A_{11}^3 - 3A_{11} A_{12}^2) + \frac{1}{384}(A_{11}^5 - 10A_{11}^3 A_{12}^2\right.$$

$$\left. + 5A_{11} A_{12}^4)\right] + i\left[\frac{1}{2} A_{12} - \frac{1}{16}(3A_{11}^2 A_{12} - A_{12}^3)\right.$$

$$\left. + \frac{1}{384}(5A_{11}^4 A_{12} - 10A_{11}^4 A_{12}^3 + A_{12}^5)\right] \tag{D22}$$

Let

$$A_{13} = A_{11}^2 - A_{12}^2 \tag{D23}$$

$$A_{14} = A_{11}^4 \; 6A_{11}^2 A_{12}^2 - A_{12}^4 \tag{D24}$$

$$A_{15} = A_{11}^6 - 15A_{11}^4 A_{12}^2 + 15A_{11}^2 A_{12}^4 - A_{12}^6 \tag{D25}$$

$$A_{16} = -\frac{1}{2} A_{11} A_{12} \tag{D26}$$

$$A_{17} = 4A_{11}^3 A_{12} - 4A_{11} A_{12}^3 \tag{D27}$$

$$A_{18} = 6A_{11}^5 A_{12} - 20A_{11}^3 A_{12}^3 + 6A_{11} A_{12}^5 \tag{D28}$$

$$A_{19} = 1 - A_{13}/4 + A_{14}/64 - A_{15}/2304 \tag{D29}$$

$$A_{20} = A_{16} + A_{17}/64 - A_{18}/2304 \tag{D30}$$

then equation (D21) becomes

$$J_0(RK) = A_{19} + i A_{20} \tag{D31}$$

Note that A_{19} and A_{20} are real constant numbers.

The Bessel function $J_1(RK)$ is obtained in a similar manner to $J_0(RK)$ by allowing

$$A_{21} = A_{11}^3 - 3A_{11} A_{12}^2 \tag{D32}$$

$$A_{22} = A_{11}^5 - 10A_{11}^3 A_{12}^2 + 5A_{11} A_{12}^4 \tag{D33}$$

$$A_{23} = 3A_{11}^2 A_{12} - A_{12}^3 \tag{D34}$$

$$A_{24} = 5A_{11}^4 A_{12} - 10A_{11}^2 A_{12}^3 + A_{12}^5 \tag{D35}$$

$$A_{25} = \frac{1}{2} A_{11} - A_{22}/16 + A_{22}/384 \tag{D36}$$

$$A_{26} = \frac{1}{2} A_{12} - A_{23}/16 + A_{24}/384 \tag{D37}$$

then the Bessel function $J_1(RK)$ can be written as

$$J_1(RK) = A_{25} + i A_{26} \tag{38}$$

Note that A_{25} and A_{26} are real constant numbers.

Equations (D31) and (D38) are the approximate solutions for values of Bessel functions J_o and J_1. Thus far the expressions for the argument RK and approximate solutions for J_o and J_1 have been established. The absolute values of the approximate Bessel functions J_o and J_1 are obtained from equations and (D31) and (D38), as respectively, as

$$E_o = \left| J_o(RK) \right| = (A_{19}^2 + A_{20}^2)^{1/2} \tag{D39}$$

and

$$E_1 = \left| J_1(RK) \right| = (A_{25}^2 + A_{26}^2)^{1/2} \tag{D40}$$

The actual value of J_o as obtained from the computer output is

$$J_o(RK) = BJRE(1) + i BJIM(1)$$

from which the absolute value is defined as

$$A_o + \left| J_o(RK) \right| = \left\{ [BJRE(1)]^2 + [BJIM(1)]^2 \right\}^{1/2} \tag{D41}$$

58

Similarly, the absolute value of $J_1(RK)$ can be shown to be

$$A_1 = |J_1(RK)| = \left\{ [BJRE(2)]^2 + [BJIM(2)]^2 \right\}^{1/2} \qquad (D42)$$

the difference between actual and estimated values of J_0 is defined as

$$D_0 = |A_0 - E_0| \qquad (D43)$$

Thus the error based on the actual value is then defined as

$$\text{Error } \% = \frac{|A_0 - E_0|}{A_0} \cdot 100\% \qquad (D44)$$

In a similar manner the error for J_1 is defined as

$$\text{Error } \% = \frac{|A_1 - E_1|}{A_1} \cdot 100\% \qquad (D45)$$

The procedure for determining the approximate and actual values of J_0 and J_1 is as follows:

1. Determine the values of ω_r and ω_i from equation (A14) for a specified airspeed.

2. Substitute ω_r, ω_i, and other relevant information into equation (D18) to obtain the values of the real and imaginary parts of the argument, i.e. A_{11} and A_{12}.

3. Input the values of A_{11} and A_{12} into subroutine COMBES to determine the values of J_0 and J_1 and their absolute values.

4. Use the value of ω from step 1 to evaluate A_{19} and A_{20} and find the absolute approximate value for J_0 as in equation (D39).

5. Proceed as instructed in step 4 to calculating A_{25} and A_{26} and obtain the absolute approximate value for J_1 as in equation (D40).

6. Compare the solutions from steps 3, 4, and 5 with the absolute actual values of J_o and J_1 as in equations (D41) and (D42).

7. Finally, calculate the error for J_o and J_1 by using equations (D44) and (D45), respectively.

The flow diagram is shown in figure D-1, and the computer program and a sample output appear at the end of the appendix.

The computer output shows that the arguments of the Bessel functions are indeed less than one for each case shown. Therefore, since the procedure for deriving and calculating the numerical solutions satisfies this requirement, the solution procedure is correct. Furthermore, the error analysis reveals insignificant difference between the actual and estimated values of the Bessel functions. The errors based on equations (D44) and (D45) were 0.11×10^{-7} when J_o had the value of 1, and 0.25×10^{-8} when J_1 had the value of 0.676×10^{-1}.

Find desired ω_r and ω_i from the
listed step in Appendix E

Find the argument of J in the form
$RK = A_{11} + i\, A_{12}$

CALL COMBES (A_{11}, A_{12},...). Get actual
values of J_o and J_1

Get estimated values of J_o and $\bar{J_1}$
by calculating A_{19}, A_{20}, A_{25}, and A_{26}

Find A_o, E_o, A_1 and E_1 from equa-
tions (D41), (D39), (D42) and (D40)

Calculate the error percentage by
using equations (D44) and (D45)

Calculate the frequency,... etc.
Return to original procedures

Figure D-1. Flow diagram for error analysis in the Bessel functions.

```
      PROGRAM WHISTL (INPUT,OUTPUT,TAPE5=INPUT,TAPE6=OUTPUT)
      DIMENSION VEL(11),WC(11),RE(11),ST(11),UU(11),WCK(11),
      DIMENSION U(11)
      DIMENSION ALPHAD(5),N1(5),FREQ(11),XO(11)
      DIMENSION COEFF(7),ROOT1(6,2),Q(11),QQ(11)
      DIMENSION BJRE(50),BJIM(50),YRE(10),YIM(10)
      COMPLEX ROOT(6)
      NN=11
      CK=1
      MM=6
      WRITE(MM,1)
    1 FORMAT(1H1)
      IDEGRE=6
      PI=3.1415927
      XNU=160.0E-06
      N=1
      LL=1
      D1=0.745/12.
      DO 25 LM=1,3
      IF(LM-2) 2,3,4
    2 D2=0.625/12.
      GO TO 5
    3 D2=0.6/12.
      GO TO 5
    4 D2=0.375/12.
    5 CONTINUE
      DO 24 NM=1,2
      IF(NM-1) 6,6,7
    6 D3=0.375/12.
      GO TO 8
    7 D3=0.25/12.
    8 CONTINUE
      WRITE(MM,9) LL
    9 FORMAT(5X,*FOR THE DEVICE *,I1/)
      R=D3/2.
      H=0.1/12.
      CKW=CK/(2.*PI)
      DO 23 IJ=1,3
      XIJ=IJ+2
      DO 22 II=1,3
      N1(II)=II+1
      ALPHAD(IJ)=XIJ*15.
      WRITE(MM,10) N1(II),ALPHAD(IJ)
   10 FORMAT(5X,I1,*-*,F3.0,*DEGREE SWIRLER*//)
      ALPHA=ALPHAD(IJ)*PI/180.
      AREAA=PI/4.*(D1**2.-D2**2.)-N1(II)*H*(D1-D2)/2.
      AREAB=PI/4.*D3**2
      RE2=SQRT((D1/2.)**2-(AREAA/PI))
```

<div align="center">(cont'd)</div>

```
      WRITE(MM,11)
   11 FORMAT(5X,*VEL*,11X,*RE J*,11X,*IM J*,8X,*ERROR %*,14X
     1,*ARGUMENT OF J*/)
      U(1)=0.0
C********** CHANGE VELOCITY **********************
      DO 21 J=1,11
      VEL(J)=U(J)*5280./3600.
      UU(J)=U(J)*1.60935
      Q(J)=VEL(J)*COS(ALPHA)*AREAA*60.
      QQ(J)=UU(J)*COS(ALPHA)*1000./60.*AREAA*0.0929
      WC(J)=VEL(J)*COS(ALPHA)*AREAA/AREAB
      WCK(J)=WC(J)*0.304801E-03*3600.
      RE(J)=WC(J)*D3/XNU
      XO(J)=2.*VEL(J)*SIN(ALPHA)*((D1/2.)**3.-RE2**3.)/(R**3
     1.*(D1/2.+RE2))
      CO=XO(J)+CK*WC(J)
      C1=4.*XO(J)**2.-CO**2.
      C2=R*CK/2.
      C3=C2**2.
      C4=C2**3./2.
      C5=C2**4./4.
      C6=C2**5./12.
      C7=C2**6./36.
      C8=XO(J)-CK*WC(J)
      C9=9.*CO**2.-C1
      C10=3.*CO*C1-7.*CO**3.
      C11=2.*CO**4.-3.*CO**2.*C1
      C12=8.*CO**2.-2.*C1
      C13=4.*CO*C1-4.*CO**3.+2.*C1
      C14=C1**2.-4.*CO**2.*C1
      C15=14.*CO**2.-C1
      C16=4.*CO*C1-16.*CO**3.
      C17=9.*CO**4.-6.*CO**2.*C1
      C18=4.*CO**3.*C1-2.*CO**5.
      C19=9.*CO**2.+4.*CO-2.*C1
      C20=8.*CO*C1-8.*CO**2.-4.*CO**3.
      C21=4.*CO**3.-10.*CO**2.*C1+C1**2.
      C22=4.*CO**3.*C1-2.*CO*C1**2.
      C23=12.*CO**2.-3.*C1
      C24=12.*CO*C1-8.*CO**3.
      C25=3.*C1**2.-12.*C1*CO**2.
      C26=C2+C4+C6
      C27=1.+C3+C5+C7
      C28=10.*CO**2.*C2+C4*C9+C6*C12
      C29=15.*CO**2.+C3*C15+C5*C19+C7*C23
      C30=-10.*CO**3.*C2+C4*C10+C6*C13+10.*CO**2.*C2*C8+C4*
     1C8*C9+C6*C8*C12
      C31=20.*CO**3.-C3*C16-C5*C20-C7*C24
```

```
      C32=5.*C0**4.*C2+C4*C11+C6*C14-10.*C0**3.*C2*C8+C4*C8*
     1C10+C6*C8*C13
      C33=C3*C17-15.*C0**4.-C5*C21-C7*C25
      C34=C0**2.*C4-C1*C6
      C341=C0**4.*C2*(5.*C8-C0)
      C35=C4*C8*C11+C6*C8*C14
      C36=6.*C0**5.-C3*C18-C5*C22+6.*C0*C1**2*C7
      C37=C0**2.*C4-C1*C6
      C38=-C0**4.+C0**2.*C1*C3-C1**2.*C5
      CC=1./C2
      C39=(CC*C26)/2.-C27
      C40=(CC*C26/2.)*(C8-5.*C0)+6.*C0*C27
      C41=CC/2.*(C28-5.*C0*C8*C26)-C29
      C42=CC*C30/2.+C31
      C43=CC*C32/2.+C33
      C44=CC/2.*(C0*C1*C34+C35+C341)+C36
      C45=CC/2.*(C0*C1*C8*C37-C0**5.*C2*C8)+C0**2.*C38+C1**3
     1.*C7
      COEFF(1)=C39
      COEFF(2)=C40
      COEFF(3)=C41
      COEFF(4)=C42
      COEFF(5)=C43
      COEFF(6)=C44
      COEFF(7)=C45
      CALL RPOLY (IDEGRE,COEFF,ROOT,IERR)
      DO 12 M=1,6
      ROOT1(M,1)=REAL(ROOT(M))
      ROOT1(M,2)=AIMAG(ROOT(M))
   12 CONTINUE
      AMAX=ROOT1(1,2)
      IMAX=1
      DO 13 MN=2,6
      IF(ROOT1(MN,2).LE.AMAX) GO TO 13
      AMAX=ROOT1(MN,2)
      IMAX=MN
   13 CONTINUE
      FREQ(J)=ROOT1(IMAX,1)/(2.*PI)/1000.
C     NOW CALCULATE THE REAL AND IMAGINARY PART OF ARGUMENT
C     OF THE BESSEL FUNCTION
      ZR=ROOT1(IMAX,1)
      ZI=ROOT1(IMAX,2)
      A1=N*XO(J)+CK*WC(J)
      A2=4.*XO(J)**2-A1**2
      A3=R*CK
      A4=A3/((ZR-A1)**2+ZI**2)
      A5=A2+2.*A1*ZR-ZR**2+ZI**2
      A6=2.*A1*ZI-2.*ZR*ZI
```

```
      IF(J-1) 14,14,15
   14 BJRE(1)=1.
      BJIM(1)=0.
      BJRE(2)=0.
      BJIM(2)=0.
      A19=1.
      A20=0.
      A25=0.
      A26=0.
      PE0=0.
      PE1=0.
      GO TO 16
   15 CONTINUE
      THETA1=ATAN2(A6,A5)
      THETA=THETA1/2.
      A7=ZR-A1
      A8=(A5**2+A6**2)**0.25
      A9=A7*COS(THETA)+ZI*SIN(THETA)
      A10=A7*SIN(THETA)-ZI*COS(THETA)
      A11=A4*A8*A9
      A12=A4*A8*A10
C     FIND THE ACTUAL VALUES OF THE BESSEL FUNCTIONS
      CALL COMBES(A11,A12,0.,0.,1,BJRE,BJIM,YRE,YIM)
C     FIND THE ESTIMATED VALUES OF BESSEL FUNCTION JO
      A13=A11**2-A12**2
      A14=A11**4-6.*A11**2*A12**2+A12**4
      A15=A11**6-15.*A11**4*A12**2+15.*A11**2*A12**4-A12**6
      A16=-0.5*A11*A12
      A17=4.*A11**3*A12-4.*A11*A12**3
      A18=6.*A11**5*A12-20.*A11**3*A12**3+6.*A12**5*A11
      A19=1.-A13/4.+A14/64.-A15/2304.
      A20=A16+A17/64.-A18/2304.
C     FIND THE ESTIMATED VALUES OF BESSEL FUNCTION J1
      A21=A11**3-3.*A11*A12**2
      A22=A11**5-10.*A11**3*A12**2+5.*A11*A12**4
      A23=3.*A11**2*A12-A12**3
      A24=5.*A11**4*A12-10.*A11**2*A12**3+A12**5
      A25=0.5*A11-A21/16.+A22/384.
      A26=0.5*A12-A23/16.+A24/384.
C     ACTUAL VALUE OF JO
      CA0=SQRT(BJRE(1)**2+BJIM(1)**2)
C     ESTIMATED VALUE OF JO
      CE0=SQRT(A19**2+A20**2)
C     ACTUAL VALUE OF J1
      CA1=SQRT(BJRE(2)**2+BJIM(2)**2)
C     ESTIMATED VALUE OF J1
      CE1=SQRT(A25**2+A26**2)
      DC0=ABS(CA0-CE0)
```

```
C    ERROR PERCENTAGE OF J0
     PE0=DC0/CA0*100.
     DC1=ABS(CA1-CE1)
C    ERROR PERCENTAGE OF J1
     PE1=DC1/CA1*100.
 16  CONTINUE
     WRITE(MM,17) U(J),BJRE(1),BJIM(1),A11,A12,A19,A20,PE0
    1,BJRE(2),BJIM(2),A25,A26,PE1
 17  FORMAT(5X,F4.0,2X,*(A) *,E13.7,2X,E13.7,15X,*(*,E13.7
    1,* +I *,E13.7,*)*/11X,*(E) *,E13.7,2X,E13.7,2X,E11.5/
    211X,*(A) *,E13.7,2X,E13.7/11X,*(E) *,E13.7,2X,E13.7,2
    3X,E11.5/)
     IF(J-1) 18,18,19
 18  ST(1)=0.0
     GO TO 20
 19  ST(J)=FREQ(J)*1000.*D3/WC(J)
 20  CONTINUE
     U(J+1)=U(J)+20.
 21  CONTINUE
 22  CONTINUE
 23  CONTINUE
     LL=LL+1
     WRITE(MM,1)
 24  CONTINUE
 25  CONTINUE
     STOP
     END
```

SAMPLE OUTPUT OF COMPUTER PROGRAM FOR DETERMINING

VALUES OF J_0 AND J_1

Solution
FOR THE DEVICE 1 $(P_1 = 0.745", P_2 = 0.625", D_3 = 0.375")$ $\star$ (A) denotes actual value of J
(E) " approx.

$$\text{Error } \% \equiv \frac{||E| - |A||}{|A|} \times 100 \ \%$$

VEL (MPH)		RE(J)	IM(J)	ERROR %	ARGUMENT OF J
0.	J_o (A)	.1000000E+01	0.		(-R +I -R I
	(E)	.1000000E+01	0.	0.	
	J_1 (A)	0.	0.		
	(E)	0.	0.	0.	
20.	(A)	.1003284E+01	.1298986E-02		(.2222344E-01 +I -.1167107E+00)
	(E)	.1003284E+01	.1298986E-02	.10504E-07	
	(A)	.1116784E-01	-.5844392E-01		
	(E)	.1116784E-01	-.5844392E-01	.25376E-08	
40.	(A)	.1003284E+01	.1298986E-02		(.2222344E-01 +I -.1167107E+00)
	(E)	.1003284E+01	.1298986E-02	.10505E-07	
	(A)	.1116784E-01	-.5844392E-01		
	(E)	.1116784E-01	-.5844392E-01	.25383E-08	
60.	(A)	.1003284E+01	.1298986E-02		(.2222344E-01 +I -.1167107E+00)
	(E)	.1003284E+01	.1298986E-02	.10504E-07	
	(A)	.1116784E-01	-.5844392E-01		
	(E)	.1116784E-01	-.5844392E-01	.25300E-08	
80.	(A)	.1003284E+01	.1298986E-02		(.2222344E-01 +I -.1167107E+00)
	(E)	.1003284E+01	.1298986E-02	.10506E-07	
	(A)	.1116784E-01	-.5844392E-01		
	(E)	.1116784E-01	-.5844392E-01	.25376E-08	
100.	(A)	.1003284E+01	.1298986E-02		(.2222344E-01 +I -.1167107E+00)
	(E)	.1003284E+01	.1298986E-02	.10505E-07	
	(A)	.1116784E-01	-.5844392E-01		
	(E)	.1116784E-01	-.5844392E-01	.25383E-08	
120.	(A)	.1003284E+01	.1298985E-02		(.2222344E-01 +I -.1167107E+00)
	(E)	.1003284E+01	.1298986E-02	.10505E-07	
	(A)	.1116784E-01	-.5844392E-01		
	(E)	.1116784E-01	-.5844392E-01	.25383E-08	
140.	(A)	.1003284E+01	.1298986E-02		(.2222344E-01 +I -.1167107E+00)
	(E)	.1003284E+01	.1298986E-02	.10505E-07	
	(A)	.1116784E-01	-.5844392E-01		
	(E)	.1116784E-01	-.5844392E-01	.25387E-08	
160.	(A)	.1003284E+01	.1298986E-02		(.2222344E-01 +I -.1167107E+00)

(Cont'd)

```
(E) .1003284E+01    .1298986E-02    .10504E-07
(A) .1116784E-01  -.5844392E-01
(E) .1116784E-01  -.5844392E-01    .25387E-08

180.  (A) .1003284E+01   .1298986E-02           ( .2222344E-01 +I -.1167107E+00)
      (E) .1003284E+01   .1298986E-02    .10505E-07
      (A) .1116784E-01  -.5844392E-01
      (E) .1116784E-01  -.5844392E-01    .25380E-08

200.  (A) .1003284E+01   .1298986E-02           ( .2222344E-01 +I -.1167107E+00)
      (E) .1003284E+01   .1298986E-02    .10504E-07
      (A) .1116784E-01  -.5844392E-01
      (E) .1116784E-01  -.5844392E-01    .25387E-08
```

3-45.DEGREE SWIRLER

VEL		RE J	IM J	ERROR %	ARGUMENT OF J
0.	(A)	.1000000E+01	0.		(.2222344E-01 +I -.1167107E+00)
	(E)	.1000000E+01	0.	0.	
	(A)	0.	0.		
	(E)	0.	0.	0.	
20.	(A)	.1003284E+01	.1298986E-02		(.2222346E-01 +I -.1167106E+00)
	(E)	.1003284E+01	.1298987E-02	.10504E-07	
	(A)	.1116785E-01	-.5844391E-01		
	(E)	.1116785E-01	-.5844391E-01	.25383E-08	
40.	(A)	.1003284E+01	.1298986E-02		(.2222346E-01 +I -.1167106E+00)
	(E)	.1003284E+01	.1298987E-02	.10504E-07	
	(A)	.1116785E-01	-.5844391E-01		
	(E)	.1116785E-01	-.5844391E-01	.25387E-08	
60.	(A)	.1003284E+01	.1298986E-02		(.2222346E-01 +I -.1167106E+00)
	(E)	.1003284E+01	.1298987E-02	.10505E-07	
	(A)	.1116785E-01	-.5844391E-01		
	(E)	.1116785E-01	-.5844391E-01	.25380E-08	
80.	(A)	.1003284E+01	.1298986E-02		(.2222346E-01 +I -.1167106E+00)
	(E)	.1003284E+01	.1298987E-02	.10505E-07	
	(A)	.1116785E-01	-.5844391E-01		
	(E)	.1116785E-01	-.5844391E-01	.25383E-08	
100.	(A)	.1003284E+01	.1298986E-02		(.2222346E-01 +I -.1167106E+00)
	(E)	.1003284E+01	.1298987E-02	.10505E-07	
	(A)	.1116785E-01	-.5844391E-01		
	(E)	.1116785E-01	-.5844391E-01	.25383E-08	

COMPUTING PROCEDURE AND PROGRAMMING

Equation (A14) can be easily solved by use of the computer, and the step by step procedure is given below.

1. Input the physical parameters D_1, D_2, D_3, n_1, α and calculate equations (B1), (B2), (B3), (B7), and (B9).

2. Set airspeed equal to 0 km/hr and calculate all the polynomial co-efficients listed in Appendix A.

3. Find the roots of the polynomial by calling the subroutine RPOLY.

4. Separate the real and imaginary parts of the roots.

5. Find the maximum value of the imaginary part of root ω_i, which gives the maximum amplitude, and the corresponding real part of root ω_r.

6. Calculate the frequency response and Strouhal number St.

7. Print out the airspeed and frequency response. Then increase the airspeed and repeat the procedure until the airspeed reaches 321.9 km/hr (or 200 mph).

8. Repeat the above procedure for different vortex tube configurations and swirler designs.

The flow diagram for the above procedure is shown in figure E-1. All the data were plotted by using NASA CDC 6000 series CalComp model 765 plotter. The NASA/LaRC subroutine INFOPLT was used to generate the plot for specified information. The flow diagram used in obtaining the plot is shown in figure E-2. The complete computer program is listed after figure E-2. The program only involved sensor 4. For the other indicators, only D_2 and D_3 need to be changed.

START

Input the designed parameters D_1, D_2, D_3, k, n_1, α

Calculate A_{net}, B_{net}, $r_{e,2}$

Set U = 0.

Calculate Q, W_c, ω_o, Re

Calculate the numerical values of coefficients of equation (66)

Find the roots of equation (66) and separate into real and imaginary parts

Find the maximum value of ω_i and the corresponding ω_r

Calculate the frequency from ω_r. Calculate Strouhal number St.

Print out U, ω_i, ω_r, F, St

U + 20   < 0   U - 200   > 0

STOP

Figure E-1. Flow diagram for calculating the frequency at various true airspeeds.

70
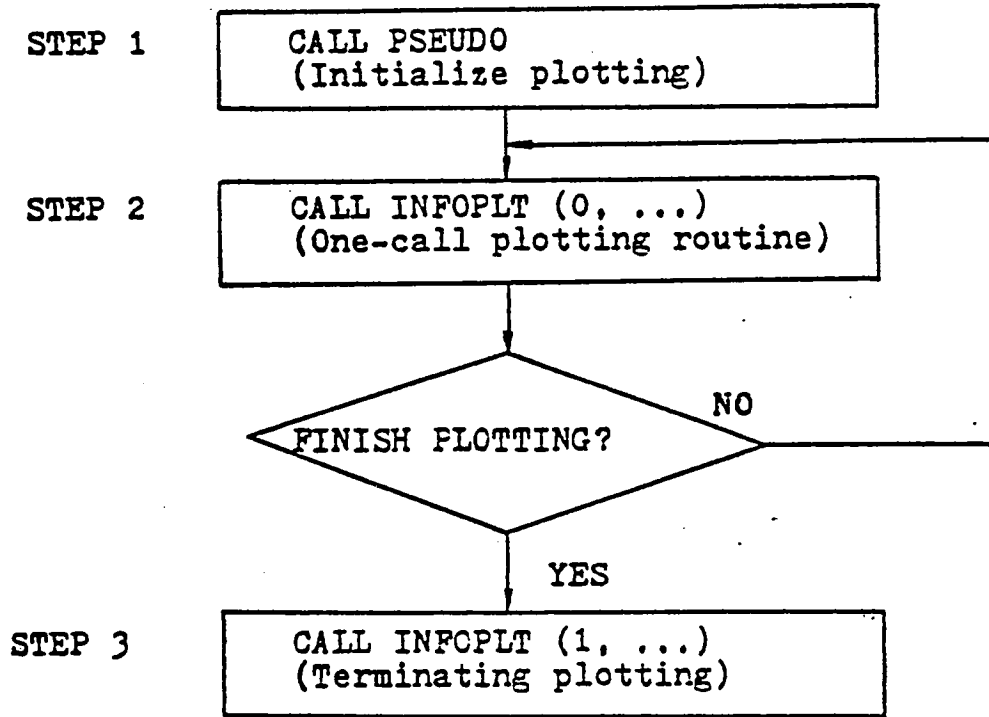
Figure E-2. Flow diagram for getting the plots.

```
      PROGRAM WHISTL (INPUT,OUTPUT,TAPE5=INPUT,TAPE6=OUTPUT)
      DIMENSION VEL(11),WC(11),RE(11),ST(11),UU(11),WCK(11)
      DIMENSION ALPHAD(5),N1(5),FREQ(11),XO(11),U(11)
      DIMENSION ROOT1(6,2)
      DIMENSION COEFF(7)
      COMPLEX ROOT(6)
C     NUMBER OF POINTS TO BE CALCULATED
      NN=11
C     DEFINE WAVENUMBER K
      CK=1.
C     CHANGE THE VALUES OF K
      DO 24 K=1,4
      MM=6
      WRITE(MM,1)
    1 FORMAT(1H1)
C     DEGREE OF THE POLYNOMIAL
      IDEGRE=6
C     DEFINE THE PARAMETERS FOR THE INDICATOR
      D1=0.745/12.
      D2=0.6/12.
      D3=0.25/12.
      R=D3/2.
      H=0.1/12.
      PI=3.1415927
      XNU=160.0E-06
C     AN INTEGER REPRESENTS THE PERTURBATIONS ARE CONSTANT
C     ALONG A SIMPLE HELIX
      N=1
      DO 23 IJ=1,3
      XIJ=IJ+2
C     DESIGNED NUMBER OF FLUTES ON THE SWIRLER
      DO 22 II=1,3
      N1(II)=II+1
      CKW=CK/(2.*PI)
      WRITE(MM,2) CK,CKW
    2 FORMAT(5X,*THE WAVENUMBER K=*,E10.3,10X,*THE WAVELENG
     1TH=K/(2.PI)=*,E10.3////)
C     DESIGNED EXIT ANGLES ON THE SWIRLER
      ALPHAD(IJ)=XIJ*15.
      ALPHA=ALPHAD(IJ)*PI/180.
      AREAA=PI/4.*(D1**2.-D2**2.)-N1(II)*H*(D1-D2)/2.
      AREAB=PI/4.*D3**2
C     EQ.(B3)
      RE2=SQRT((D1/2.)**2-(AREAA/PI))
      WRITE(MM,3)D1,D2,D3,H,N1(II),AREAA,AREAB
    3 FORMAT(5X,*D1=*,F10.5/5X,*D2=*,F10.5/5X,*D3=*,F10.5//
     15X,*H=*,F10.5/5X,*HOW MANY FLUTES IN THE SWIRLER?*,I3
     2/5X,*NET AREA AT SECTION A-A=*,F10.5/5X,*NET AREA AT
     3SECTION B-B=*,F10.5//)
```

(cont'd)

```
      WRITE(MM,4),N,ALPHAD(IJ)
    4 FORMAT(5X,*N=*,I2/5X,*EXIT ANGLE OF SWIRLER=*,F5.1,2X,
     1*DEGREES*//)
      U(1)=0.0
C********** CHANGE VELOCITY **********************
      DO 21 J=1,11
C     VELOCITY FOOT PER SECOND
      VEL(J)=U(J)*5280./3600.
C     VELOCITY KILOMETER PER HOUR
      UU(J)=U(J)*1.60935
C     AXIAL MEAN VELOCITY IN Z-DIRECTION(FT/SEC)
      WC(J)=VEL(J)*COS(ALPHA)*AREAA/AREAB
C     IN KILOMETER PER HOUR
      WCK(J)=WC(J)*0.304801E-03*3600.
C     REYNOLDS NUMBER BASED ON MEAN AXIAL VELOCITY
      RE(J)=WC(J)*D3/XNU
C     UPSTREAM ANGULAR VELOCITY AT SECTION AA AS DEFINED IN
C     EQ(B7)
      XO(J)=2.*VEL(J)*SIN(ALPHA)*((D1/2.)**3.-RE2**3.)/(R**
     13.*(D1/2.+RE2))
      WRITE(MM,5)U(J),VEL(J),UU(J),WC(J),WCK(J),RE(J),XO(J)
    5 FORMAT(5X,*U=*,F7.1,2X,*MILES PER HOUR*,5X,*OR*,2X,F7
     11.1,2X,*FOOT PER SECOND*,5X,*OR*,2X,F7.1,2X,*KILOMETER
     2 PER HOUR*/5X,*WC=*,FZ1,2X,*FOOT PER SECOND*,5X,*OR*,
     32X,F7.1,2X,*KILOMETER PER HOUR*/5X,*REYNOLDS NUMBER=*
     4,F8.1/5X,*ANGULAR VELOCITY AT ENTRANCE=*,F8.1//)
      CO=XO(J)+CK*WC(J)
      C1=4.*XO(J)**2.-CO**2.
      C2=R*CK/2.
      C3=C2**2.
      C4=C2**3./2.
      C5=C2**4./4.
      C6=C2**5./12.
      C7=C2**6./36.
      C8=XO(J)-CK*WC(J)
      C9=9.*CO**2.-C1
      C10=3.*CO*C1-7.*CO**3.
      C11=2.*CO**4.-3.*CO**2.*C1
      C12=8.*CO**2.-2.*C1
      C13=4.*CO*C1-4.*CO**3.+2.*C1
      C14=C1**2.-4.*CO**2*C1
      C15=14.*CO**2.-C1
      C16=4.*CO*C1-16.*CO**3.
      C17=9.*CO**4.-6.*CO**2.*C1
      C18=4.*CO**3.*C1-2.*CO**5.
      C19=9.*CO**2.+4.*CO-2.*C1
      C20=8.*CO*C1-8.*CO**2.-4.*CO**3.
```

```
      C21=4.*CO**3.-10.*CO**2.*C1+C1**2.
      C22=4.*CO**3.*C1-2.*CO*C1**2.
      C23=12.*CO**2.-3*C1
      C24=12.*CO*C1-8.*CO**3.
      C25=3.*C1**2.-12.*C1*CO**2.
      C26=C2+C4+C6
      C27=1.+C3+C5+C7
      C28=10.*CO**2.*C2+C4*C9+C6*C12
      C29=15.*CO**2.+C3*C15+C5*C19+C7*C23
      C30=-10.*CO**3.*C2+C4*C10+C6*C13+10.*CO**2.*C2*C8+C4*
     1C8*C9+C6*C8*C12
      C31=20.*CO**3.-C3*C16-C5*C20-C7*C24
      C32=5.*CO**4.*C2+C4*C11+C6*C14-10.*CO**3.*C2*C8+C4*C8
     1*C10+C6*C8*C13
      C33=C3*C17-15.*CO**4.-C5*C21-C7*C25
      C34=CO**2.*C4-C1*C6
      C341=CO**4.*C2*(5.*C8-CO)
      C35=C4*C8*C11+C6*C8*C14
      C36=6.*CO**5.-C3*C18-C5*C22+6.*CO*C1**2*C7
      C37=CO**2.*C4-C1*C6
      C38=-CO**4.+CO**2.*C1*C3-C1**2.*C5
      CC=1./C2
      C39=(CC*C26)/2.-C27
      C40=(CC*C26/2.)*(C8-5.*CO)+6.*CO*C27
      C41=CC/2.*(C28-5.*CO*C8*C26)-C29
      C42=CC*C30/2.+C31
      C43=CC*C32/2.+C33
      C44=CC/2.*(CO*C1*C3+C35+C341)+C36
      C45=CC/2.*(CO*C1*C8*C37-CO**5.*C2*C8)+CO**2.*C38+C1**
     13.*C7
C     COEFFICIENTS OF THE POLYNOMIAL
      COEFF(1)=C39
      COEFF(2)=C40
      COEFF(3)=C41
      COEFF(4)=C42
      COEFF(5)=C43
      COEFF(6)=C44
      COEFF(7)=C45
      WRITE(MM,6) (COEFF(I),I=1,7)
    6 FORMAT(5X,7(E12.5,2X)//)
C     FIND THE COMPLEX ROOTS OF THE POLYNOMIAL
      CALL RPOLY (IDEGRE,COEFF, ROOT, IERR)
      WRITE(MM,7) IERR, IDEGRE
    7 FORMAT(5X,*IERR=*,I2,5X,I5///)
      WRITE(MM,8)
    8 FORMAT(11X,*REAL PART OF ROOT*,3X,*IMAG PART OF ROOT*
     1,11X,*ROOT NUMBER*/)
```

```
      DO 9 I=1,IDEGRE
    9 WRITE(MM,10) ROOT(I),I
   10 FORMAT(5X,2E20.5,I20)
C     SEPARATE THE REAL AND IMAGINARY PARTS OF ROOT
      DO 11 M=1,6
      ROOT1(M,1)=REAL(ROOT(M))
      ROOT1(M,2)=AIMAG(ROOT(M))
   11 CONTINUE
C     FIND THE MAXIMUM IMAGINARY PART OF ROOT AMONG THOSE
C     ROOTS
      AMAX=ROOT1(1,2)
      IMAX=1
      DO 12 MN=2,6
      IF(ROOT1(MN,2).LE.AMAX) GO TO 12
      AMAX=ROOT1(MN,2)
      IMAX=MN
   12 CONTINUE
C     DESIRED FREQUENCY RESPONSE
      FREQ(J)=ROOT1(IMAX,1)/(2.*PI)/1000.
      IF(J-1) 13,13,14
   13 RK=0.
      GO TO 15
   14 OMEGA=SQRT(AMAX**2.+ROOT1(IMAX,1)**2.)
      XK1=OMEGA-1.*XO(J)-CK*WC(J)
      XK2=SQRT(4.*XO(J)**2.-(XK1**2.))
      XK3=CK*XK2
      XK=XK3/XK1
      RK=R*XK
   15 CONTINUE
      WRITE(MM,16) RK
   16 FORMAT(5X,*THE ARGUMENT OF THE BESSEL FUNCTION =*,E12
     1.5//)
      IF(J-1) 17,17,18
   17 ST(1)=0.0
      GO TO 19
C     CALCULATE THE CORRESPONDING STROUHAL NUMBER
   18 ST(J)=FREQ(J)*1000.*D3/WC(J)
   19 CONTINUE
      WRITE(MM,20) ROOT1(IMAX,1),ROOT1(IMAX,2),FREQ(J),ST(J)
   20 FORMAT(5X,*THE DESIRED SOLUTIONS ARE*/5X,2E20.5/5X,*TH
     1E CORRESPONDING FREQUENCY AT THIS VELOCITY IS*,E15.5,2
     2X,*KHZ*/5X,*THE STROUHAL NUMBER IS*,E15.5/////)
      U(J+1)=U(J)+20.
   21 CONTINUE
      WRITE(MM,1)
   22 CONTINUE
   23 CONTINUE
      CK=CK+2.
   24 CONTINUE
      STOP
      END
```

REFERENCES

1. Lighthill, M.J.: On Sound Generated Aerodynamically. Proc. Roy, Soc. (London), Vol. 211, 1952, pp. 564-587.

2. Curle, N.: The Influence of Solid Boundaries upon Aerodynamic Sound. Proc. Roy. Soc. (London), Vol. 231, 1955, pp. 505-514.

3. Howe, M.S.: Attenuation of Sound in a Low Mach Number Nozzle Flow. J. Fluid Mech. Vol. 91, pt. 2, 1979, pp. 209-229.

4. Roshko, Anatol: On the Development of Turbulent Wakes from Vortex Streets. NACA TN-2913, Report 1191, 1953.

5. Blokhinstev, D.I. (Translated by Cooper, R.D.): Excitation of Resonance by Air Flow. Zhurnal Tekhnicheskoi Fiziki, ZhTF, Vol. XV, 1945, pp. 63-70.

6. Powell, Alan; and Shulman, A.: On the Edgetone. J. Acoust. Soc. America, Vol. 33, No. 4, Apr. 1961, pp. 395-409.

7. Powell, Alan; and Shulman, A.: Vortex Action in Edgetones. J. Acoust. Soc. America, Vol. 34, No. 2, Feb. 1962, pp. 163-166.

8. Powell, Alan; and Shulman, A.: Effects of Wire Resonance on Aerolian Tones. J. Acoust. Soc. America, Vol. 34, No. 8, Aug. 1962, pp. 1146-1147.

9. Wilson, T.A.; Beavers, G.S.; DeCoster, M.A.; Holger, D.K.; and Regenfuss, M.D.: Experiments on the Fluid Mechanics of Whistling. J. Acoust. Soc. America, Vol. 50, No. 1, pt. 2, 1971, pp. 366-372.

10. Fineblum, S.S.: Vortex Diodes. Fluidic State-of-the-Art Symposium, Vol. 1, 1974, pp. 46-80.

11. Fink, R. Martin: Prediction of Airfoil Tone Frequencies. J. Aircraft, Vol. 12, No. 2, 1975, pp. 118-120.

12. Cummings, A.: Sound Transmission at Sudden Area Expansions in Circular Ducts with Superimposed Mean Flow. J. Sound Vib., Vol. 38, No. 1, 1975, pp. 149-155.

13. Vonnegut, Bernard: A Vortex Whistle. J. Acoust. Soc. America, Vol. 26, No. 1, 1954, pp. 18-20.

14. Michelson, Irving: Theory of Vortex Whistle. J. Acoust. Soc. America, Vol. 27, No. 5, 1955, pp. 930-931.

15. Nicklas, J.P.: Investigation of a Vortex Tube True Airspeed Sensor. Cornell Aeronautical Laboratories. Report 1H-942-P-2, 1957.

16. Suzuki, M.: Theoretical and Experimental Studies on the Vortex-Tube. Scientific Papers of the Institute of Physical Chemistry Research (Tokyo), Vol. 54, No. 1, 1960, pp. 43-87.

17. Chanaud, R.C.: Experiments Concerning the Vortex Whistle. J. Acoust. Soc. America, Vol. 35, No. 7, 1963, pp. 953-960.

18. Powell, Alan: Theory of Vortex Sound. J. Acoust. Soc. America, Vol. 36, No. 1, Jan. 1964, pp. 177-195.

19. Chanaud, R.C.: Observations of Oscillatory Motion in Certain Swirling Flows. J. Fluid Mech., Vol. 21, pt. 1, 1965, pp. 111-127.

20. Talbot, L.: Laminar Swirling Pipe Flow. J. Appl. Mech., Mar. 1954, pp. 1-7.

21. Rodely, A.E.; White, D.F.; and Chanaud, R.C.: A Digital Flowmeter Without Moving Parts. ASME Paper No. 65-WA/FM-6.

22. Gore, R.W.; and Ranz, W.E.: Backflows in Rotating Fluids Moving Axially Through Expanding Cross Sections. Amer. Inst. Chem. Eng. J., Vol. 10, No. 1, 1964, pp. 83-88.

23. Chanaud, R.C.: Aerodynamic Whistles. Sci. Am., Vol. 222, No. 1, 1970, pp. 40-46.

24. Joy, Robert D.: Air Flow Measurement for Engine Control. J-TEC Associates, Inc.

25. Cartmell, Bernard C.; and Zeisler, Fred L.: Engine Mass Air Flow Meter. Ford Motor Co. 760017.

26. Weissler, Paul: Servicing the '79 Chrysler-Plymouth and Dodge Models. Pop. Mech., Oct. 1978, p. 40.

27. Kopp, J.G.: The Swirlmeter. Tenth CHEMPID Symposium (Toronto), May 1969.

28. Herzl, J. Peter: The System Approach to High Performance Gas Flow Measurement with the Swirlmeter. Flow: It's Measurement and Control in Science and Industry, Vol. 1, pt. 2, 1974, pp. 963-966.

29. White, D.F.; Rodely, A.E.; and McMurtrie, C.L.: The Vortex Shedding Flowmeter. Flow: Its Measurement and Control in Science and Industry, Vol. 1, pt. 2, 1974, pp. 967-974.

30. Yamasaki, Hiro; and Rubin, Martin: The Vortex Flowmeter. Flow: Its Measurement and Control in Science and Industry, Vol. 1, pt. 2, 1974, pp. 975-983.

31. Beale, R.B.; and Lawler, M.T.: Development of a Wall-Attachment Fluidic Oscillator Applied to Volume Flow Metering. Flow: Its Measurement and Control in Science and Industry, Vol. 1, pt. 2, 1974, pp. 989-996.

32. Kwok, C.K.; Lee, P.M.; Lin, S.: An Analytical Investigation of a Vortex Flowmeter. ISA Transactions, Vol. 14, No. 2, 1975, pp. 167-171.

33. Kirshner, Joseph M.; and Katz, Silas: Design Theory of Fluidic Components. Academy Press, 1975.

34. DiPrima, R.C.: Stability of Nonrotationally Symmetric Disturbances for Viscous Flow Between Rotating Cylinders. Phys. Fluids, Vol. 4, No. 6, June 1961, pp. 751-755.

35. Krueger, E.R., and DiPrima, R.C.: Stability of Nonrotationally Symmetric Disturbances for Inviscid Flow between Rotating Cylinders. Phys. Fluids, Vol. 5, No. 11, Nov. 1961, pp. 1362-1367.

36. Sparrow, E.M.; Munro, W.D.; Jonsson, V.K.: Instability of the Flow between Rotating Cylinders: The Widegap Problem. J. Fluid Mech., Vol. 20, pt. 1, 1964, pp. 35-46.

37. Schwarz, K.W.; Springett, B.E.; Donnelly, R.J.: Modes of Instability in Spiral Flow Between Rotating Cylinders. J. Fluid Mech., Vol. 20, pt. 2, 1964, pp. 281-289.

38. Mattingly, G.E.; and Criminale, W.O.: The Stability of an Incompressible Two-dimensional Wake. J. Fluid Mech., Vol. 51, pt. 2, 1972, pp. 233-272.

39. Kubo, I., Gouldin, F.C.: Numerical Calculations of Turbulent Swirling Flow. J. Fluid Eng., Sept. 1975, pp. 310-315.

40. Morris, Philip J.: The Spatial Viscous Instability of Axisymmetric Jets. J. Fluid Mech., Vol. 77, pt. 3, 1976, pp. 511-529.

41. Shen, Y.C.; Goglia, G.L.: Experimental and Analytical Studies in Fluidics: The Experimental Study of a True Airspeed Indicator. Progress Report, for NASA Grant NSG 1177, June 1978.

42. Jenkins, M.A.; and Traub, J.F.: A Three Stage Variable-Shift Iteration for Polynomial Zeros and Its Relation to Generalized Rayleigh Iteration. Numerische Mathematik, Vol. 14, 1970, pp. 252-263.

43. Jenkins, M.A., and Traub, J.F.: A Three-Stage Algorithm for Real Polynomials Using Quadratic Iteration. SIAM J. Numerical Analysis, Vol. 7, No. 4, Dec. 1970, pp. 545-566.

Table 1. Different combinations of vortex tube and swirler.

Size		Sensor No.					
		1	2	3	4	5	6
D_1	cm	1.892	1.892	1.892	1.892	1.892	1.892
	(in.)	(0.745)	(0.745)	(0.745)	(0.745)	(0.745)	(0.745)
D_2	cm	1.588	1.588	1.524	1.524	0.953	0.593
	(in.)	(0.625)	(0.625)	(0.6)	(0.6)	(0.375)	(0.375)
D_3	cm	0.953	0.635	0.953	0.635	0.953	0.635
	(in.)	(0.375)	(0.250)	(0.375)	(0.250)	(0.375)	(0.250)

Table 2. The working ranges of the sensors with swirlers having four flutes and different exit angles.

Type of Combination	Flow Rate Ranges	Minimum		Maximum	
		Q (m^3/min)	F (KHz)	Q (m^3/min)	F (KHz)
Sensor 1	45°	0.0304	0.72	0.1150	2.98
	60°	0.0200	0.72	0.0680	3.10
	75°	0.0200	0.89	0.0550	3.05
Sensor 2	45°	0.0152	1.03	0.0713	4.75
	60°	0.0127	1.23	0.0698	7.50
	75°	0.0090	0.85	0.0400	5.20
Sensor 3	45°	0.0330	0.70	0.1570	3.30
	60°	0.0200	0.69	0.0770	3.10
	75°	0.0180	0.74	0.0590	3.05
Sensor 4	45°	0.0206	1.20	0.1200	7.00
	60°	0.0158	1.30	0.0702	6.65
	75°	0.0090	0.84	0.0450	5.35
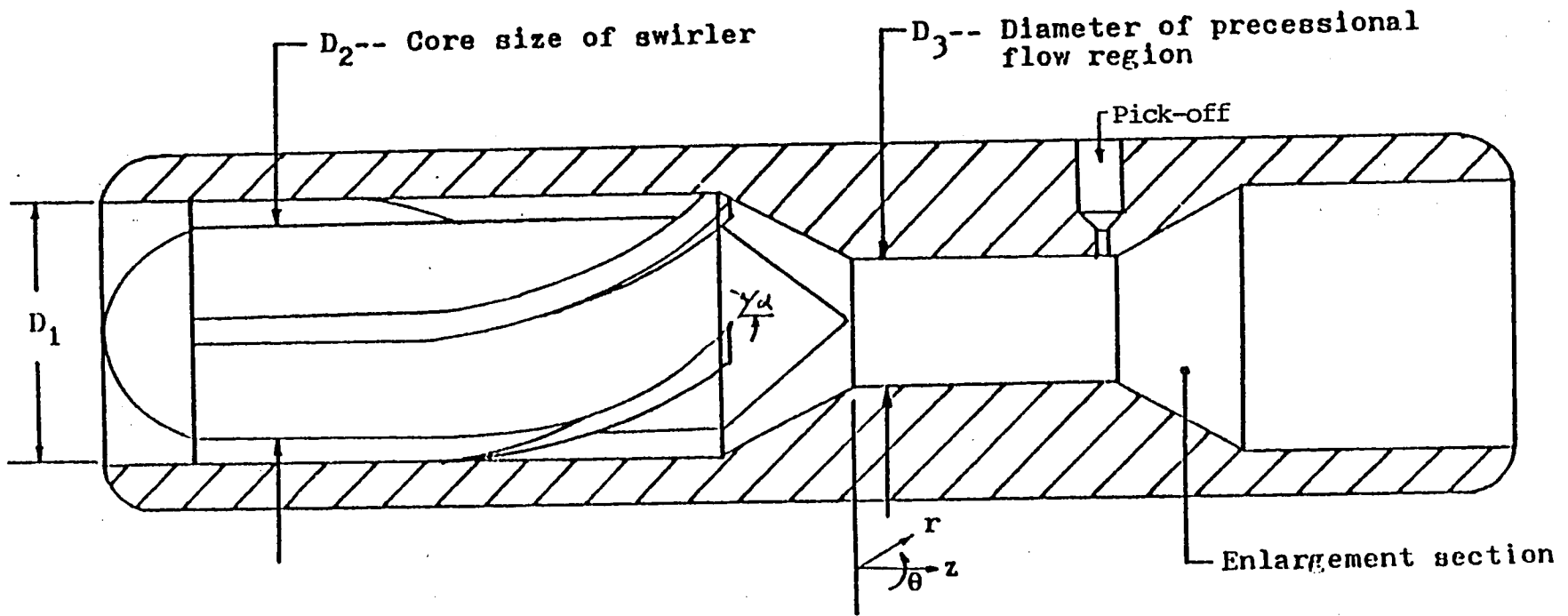
Figure 1.   Cross-sectional view of true airspeed indicator.
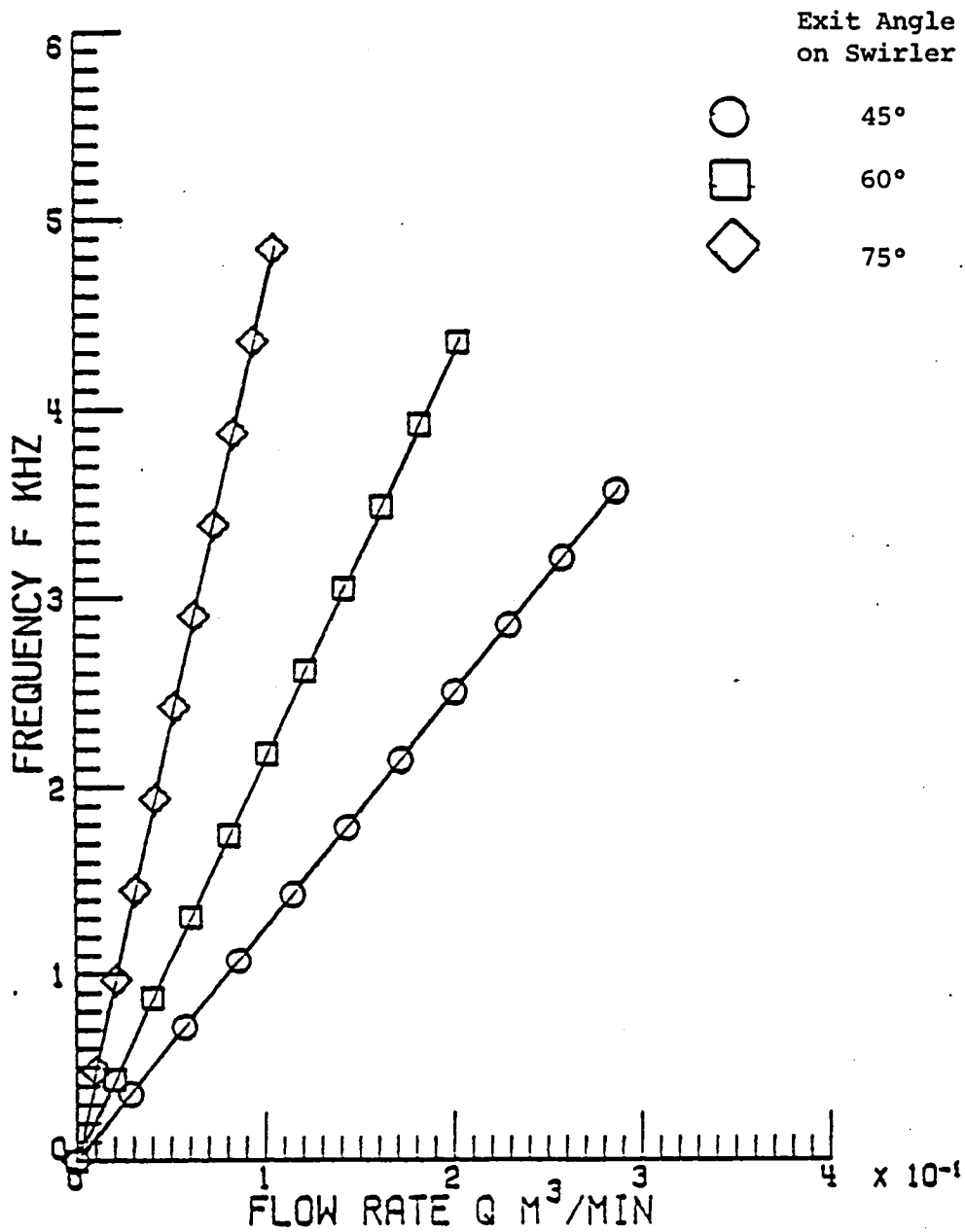
Figure 2. Flow rate versus frequency response for sensor 1 with swirlers having two flutes and various exit angles.
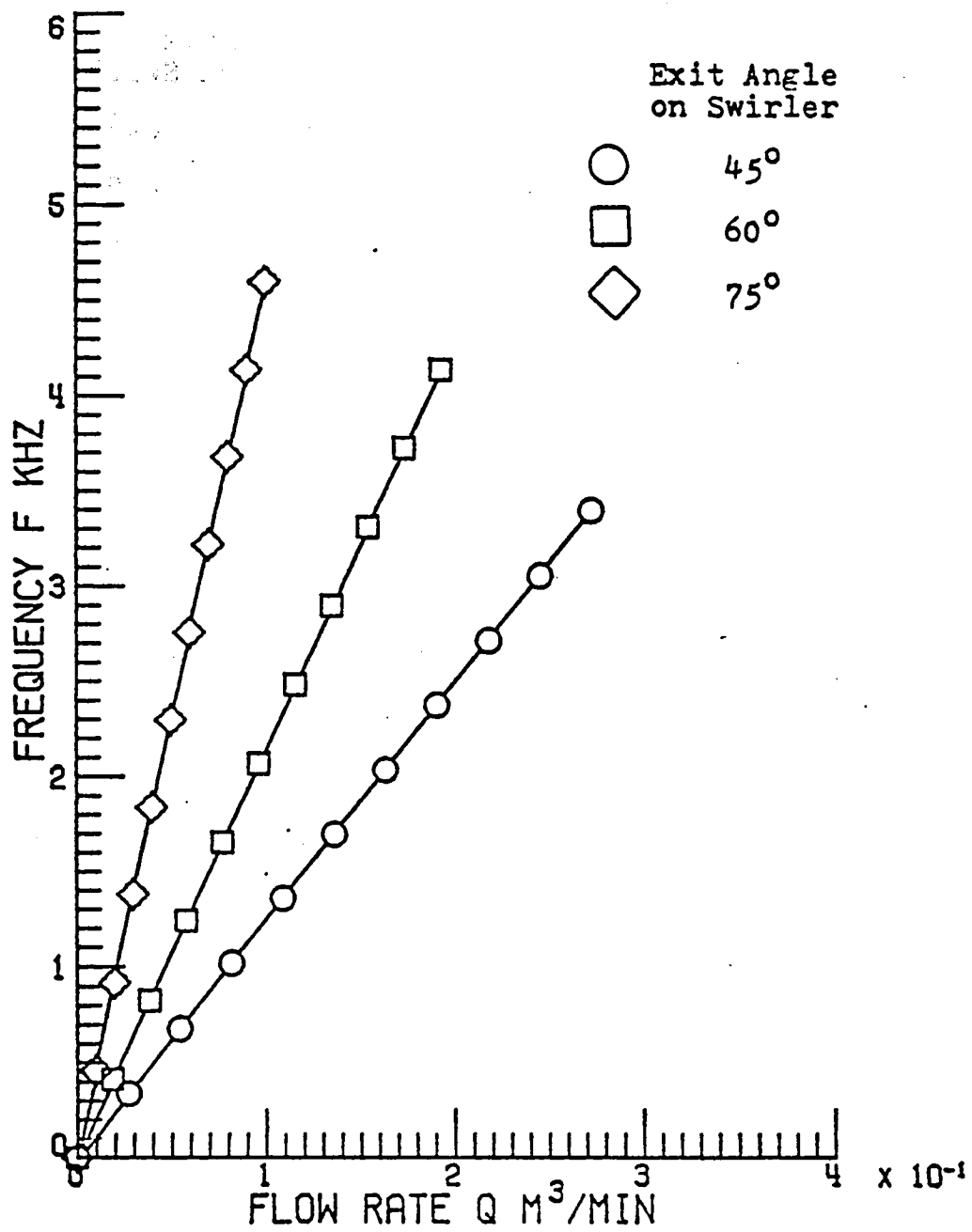
Figure 3. Flow rate versus frequency response for sensor 1 with
swirlers having three flutes and various exit angles.
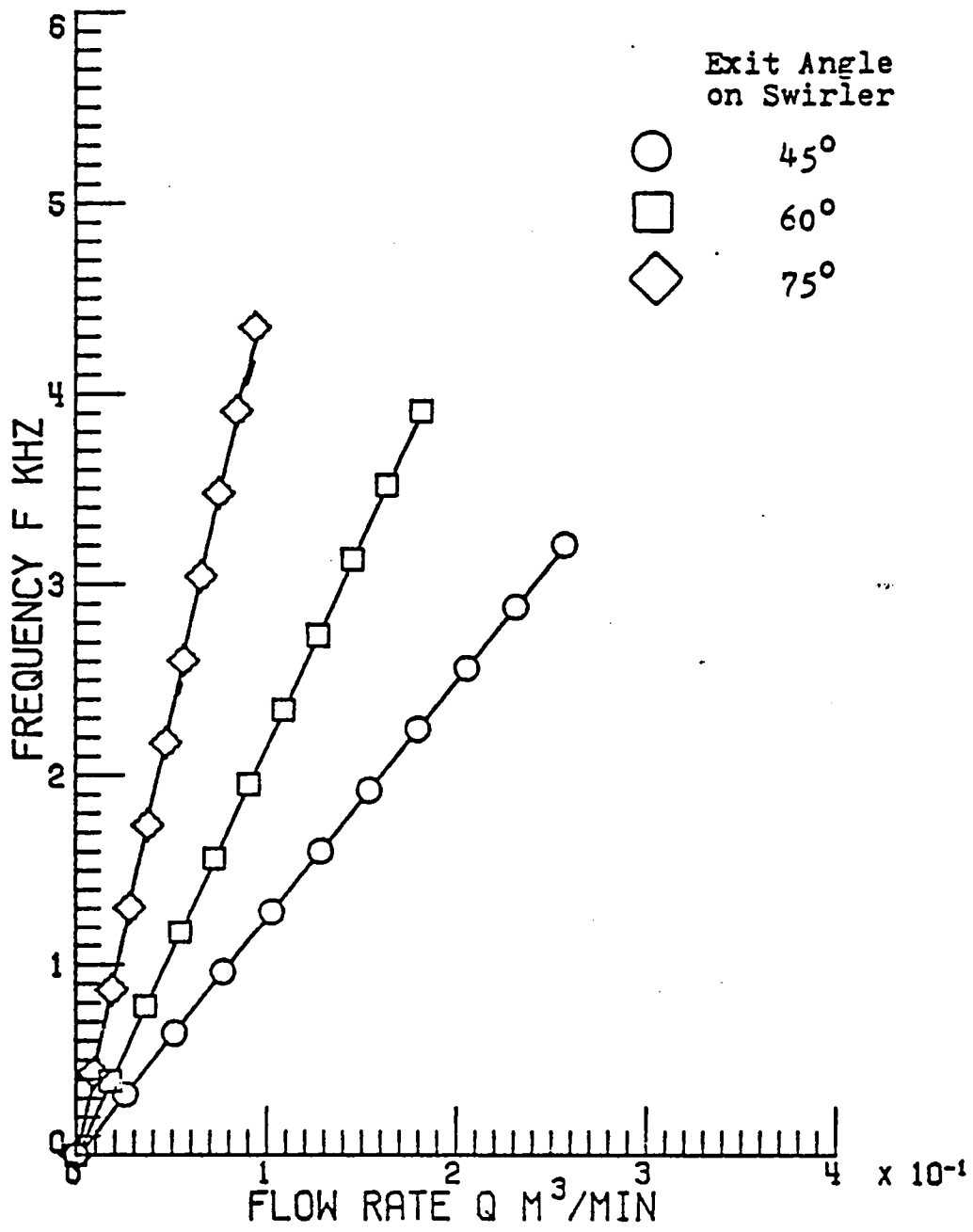
Figure 4.   Flow rate versus frequency response for sensor 1 with
            swirlers having four flutes and various exit angles.
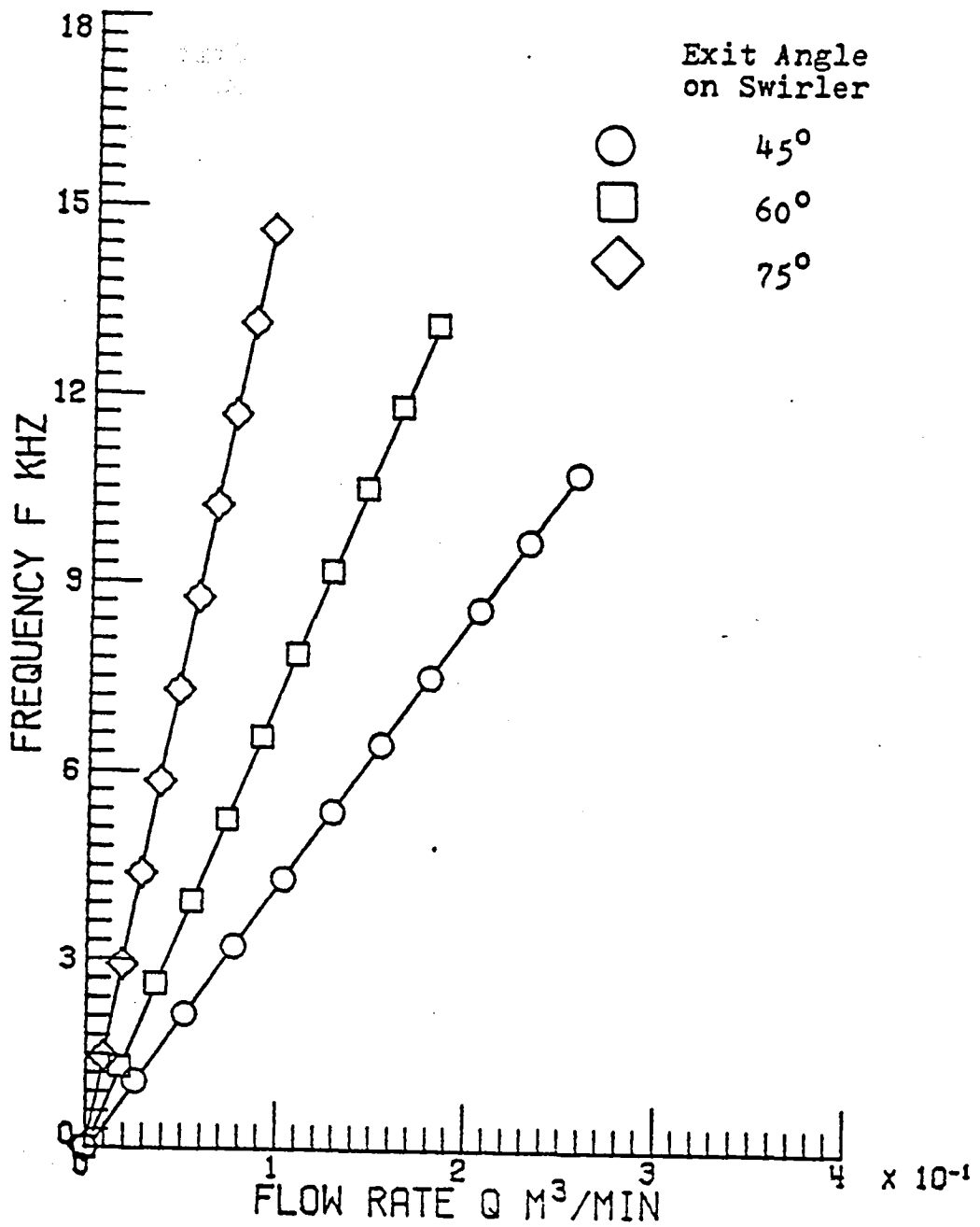
Figure 5.   Flow rate versus frequency response for sensor 2 with
            swirlers having four flutes and various exit angles.
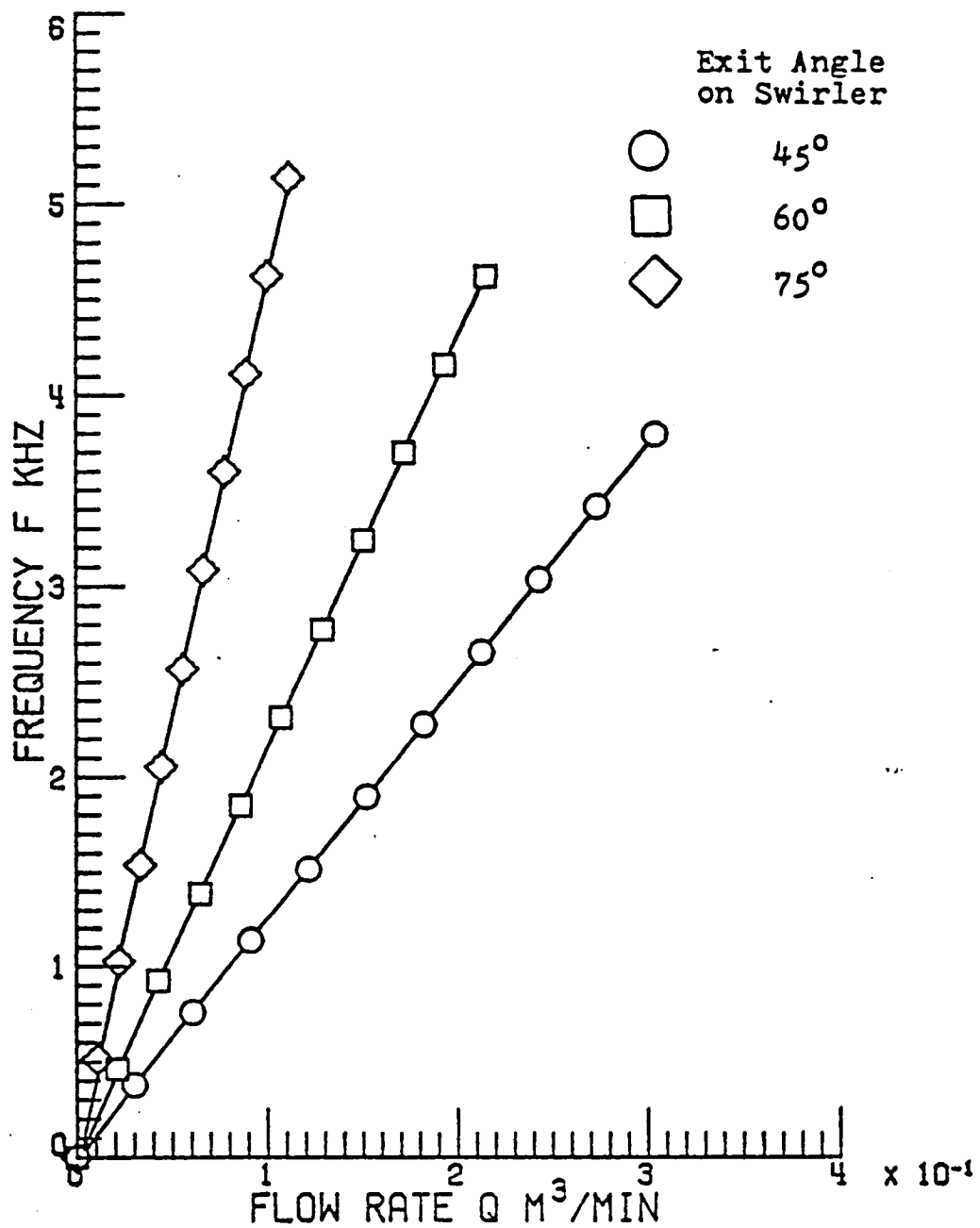
Figure 6. Flow rate versus frequency response for sensor 3 with swirlers having four flutes and various exit angles.
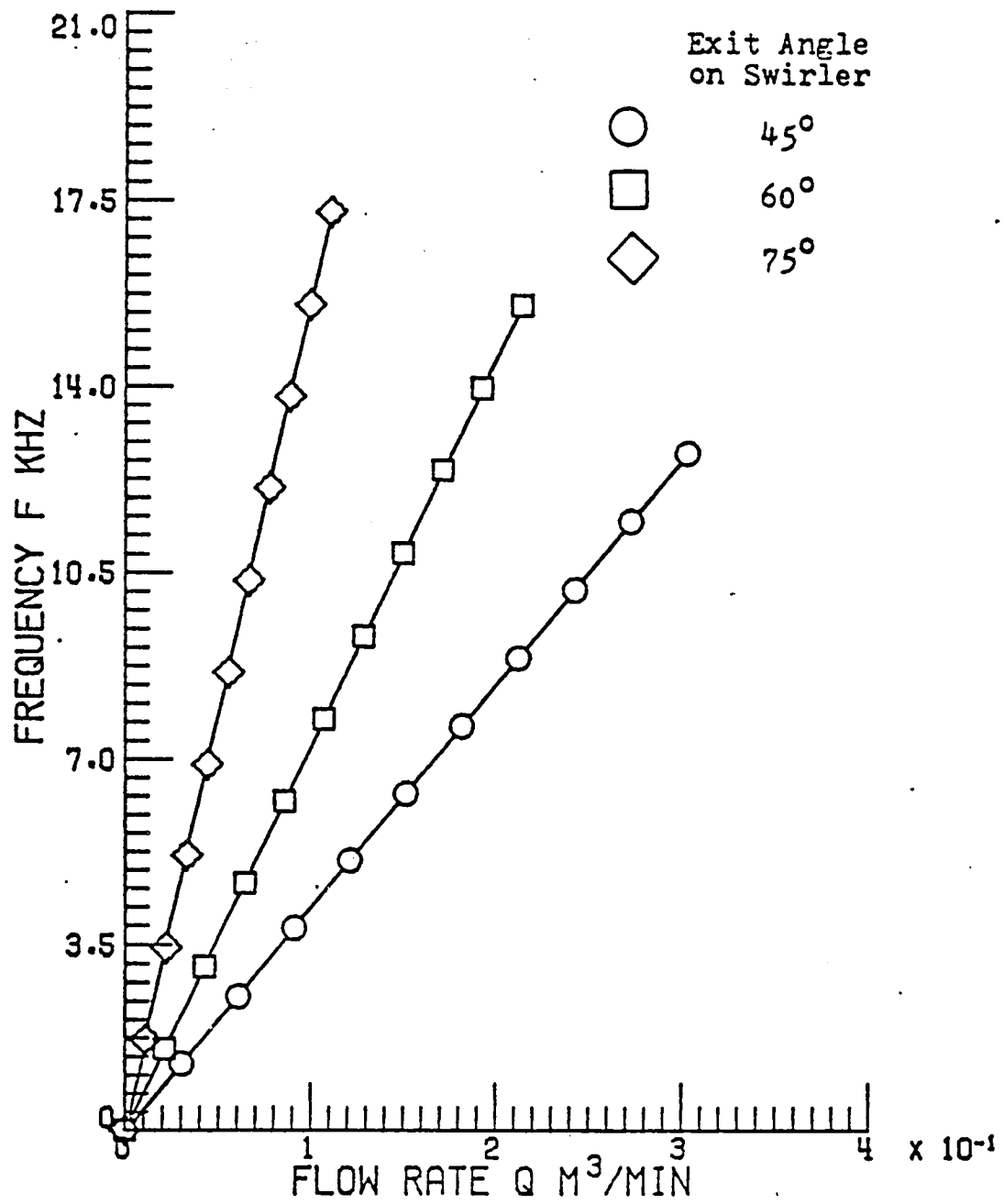
Figure 7. Flow rate versus frequency response for sensor 4 with
swirlers having four flutes and various exit angles.
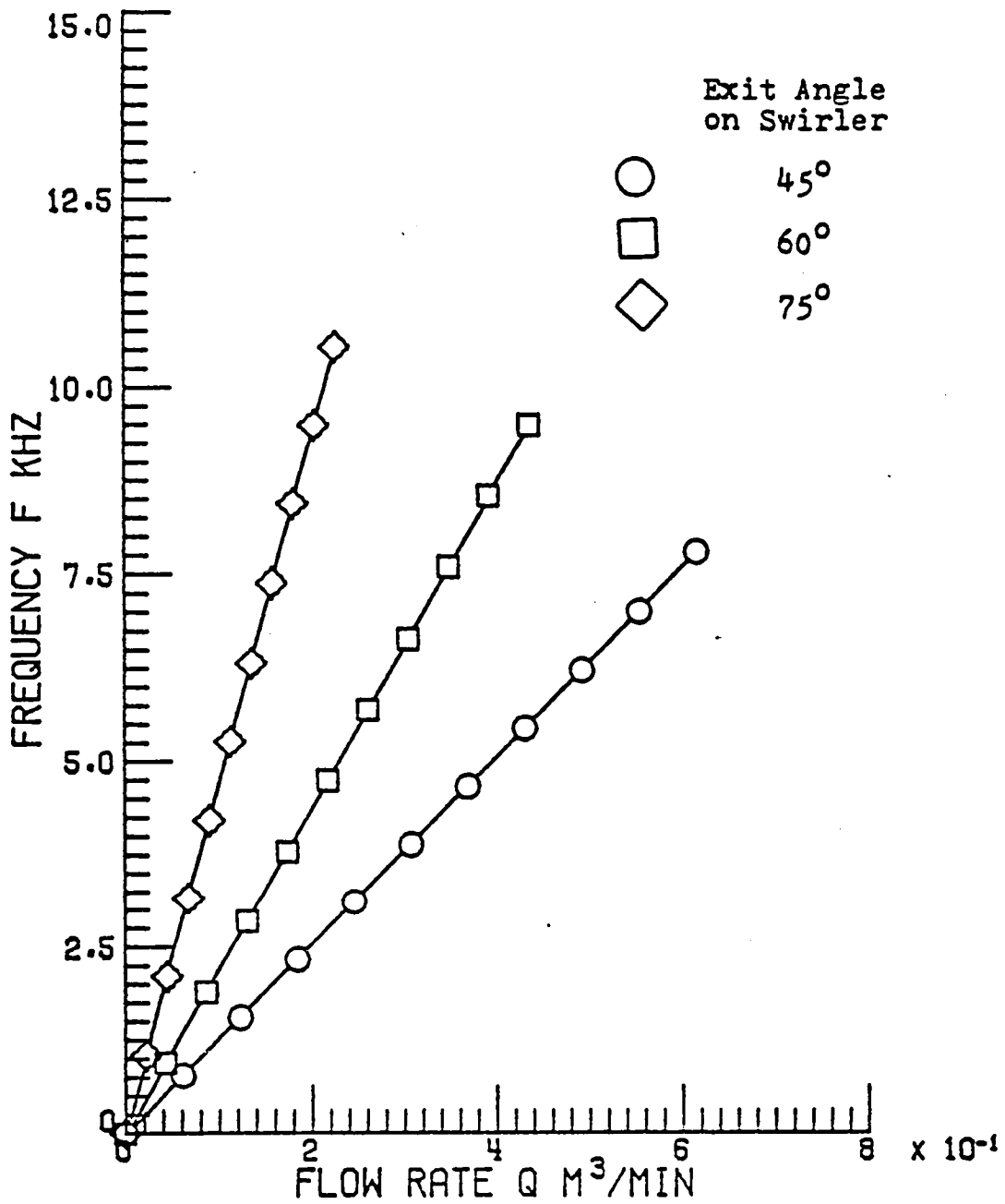
Figure 8. Flow rate versus frequency response for sensor 5 with
swirlers having four flutes and various exit angles.
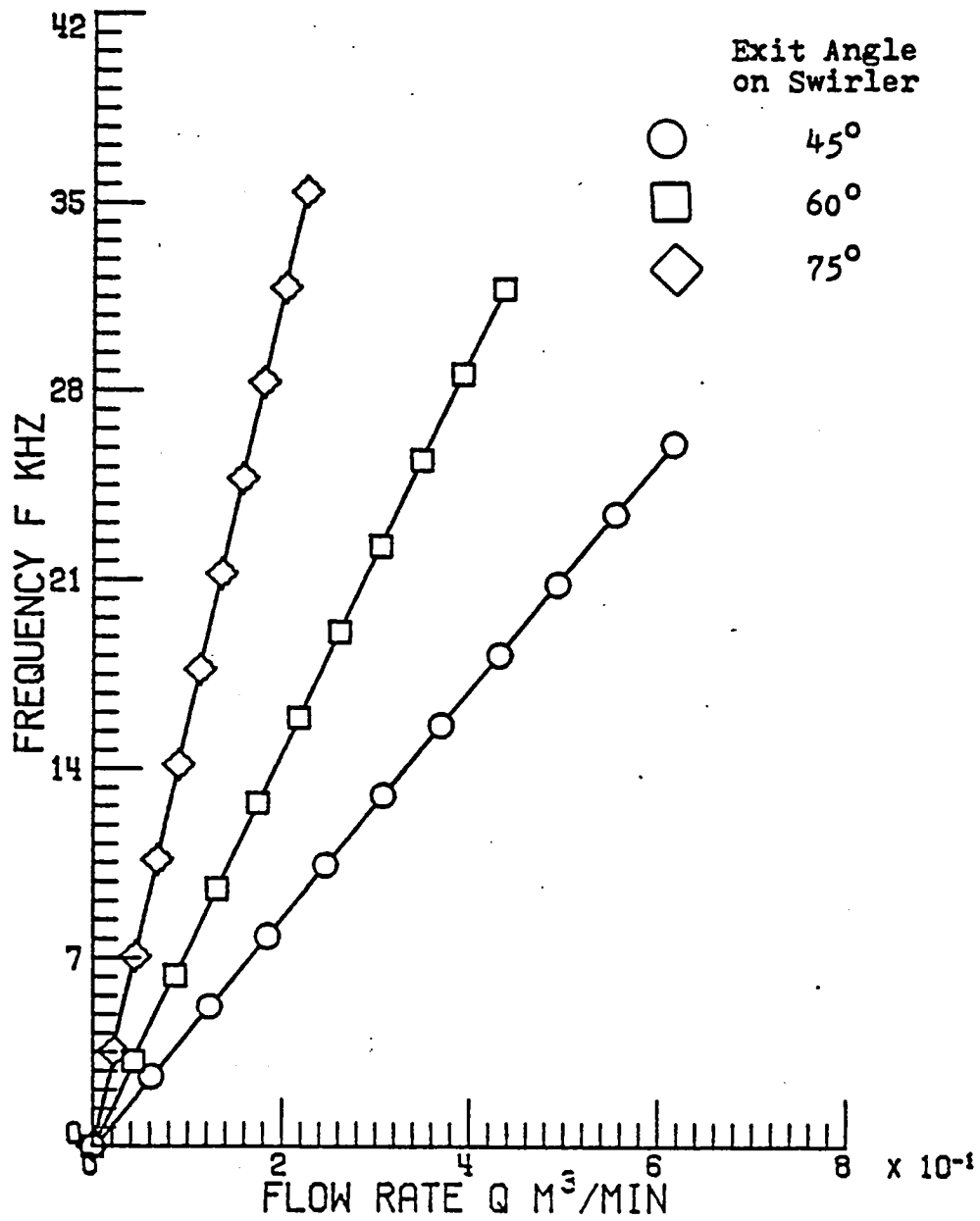
Figure 9. Flow rate versus frequency response for sensor 6 with swirlers having four flutes and various exit angles.
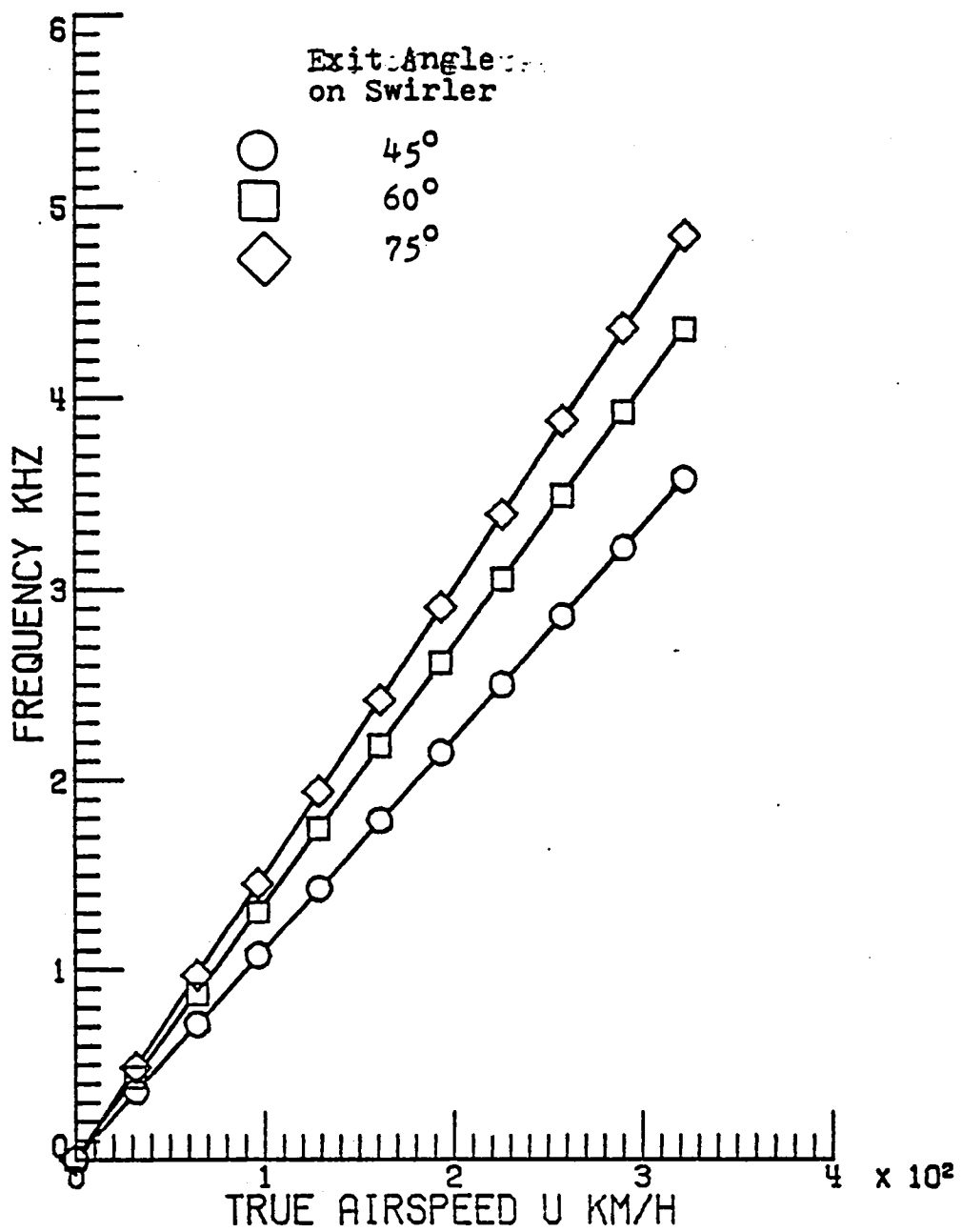
Figure 10.   True airspeed versus frequency response for sensor 1
with two-flute swirlers and wavenumber k = 1.
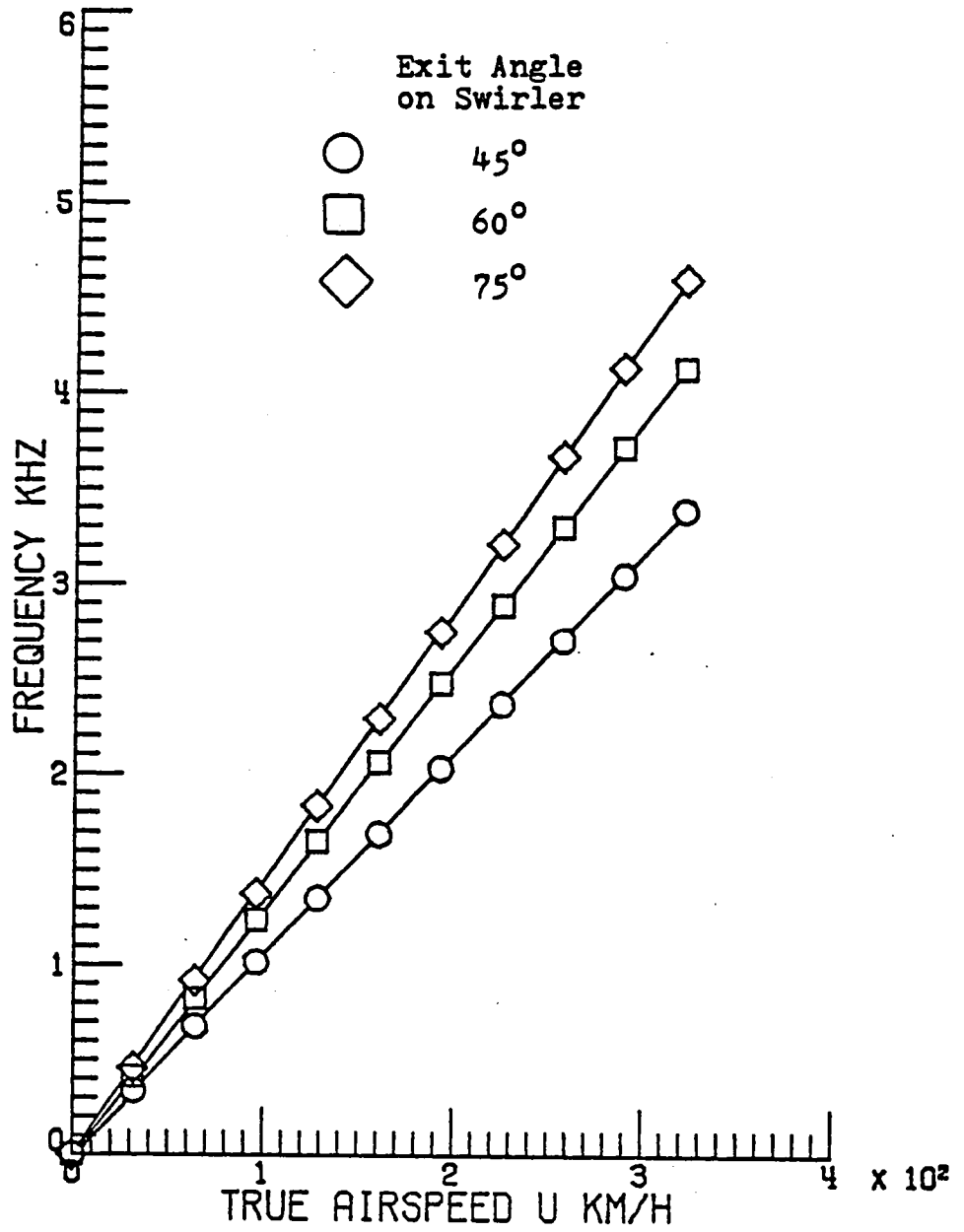
Figure 11. True airspeed versus frequency response for sensor 1 with three-flute swirlers and wavenumber k = 1.
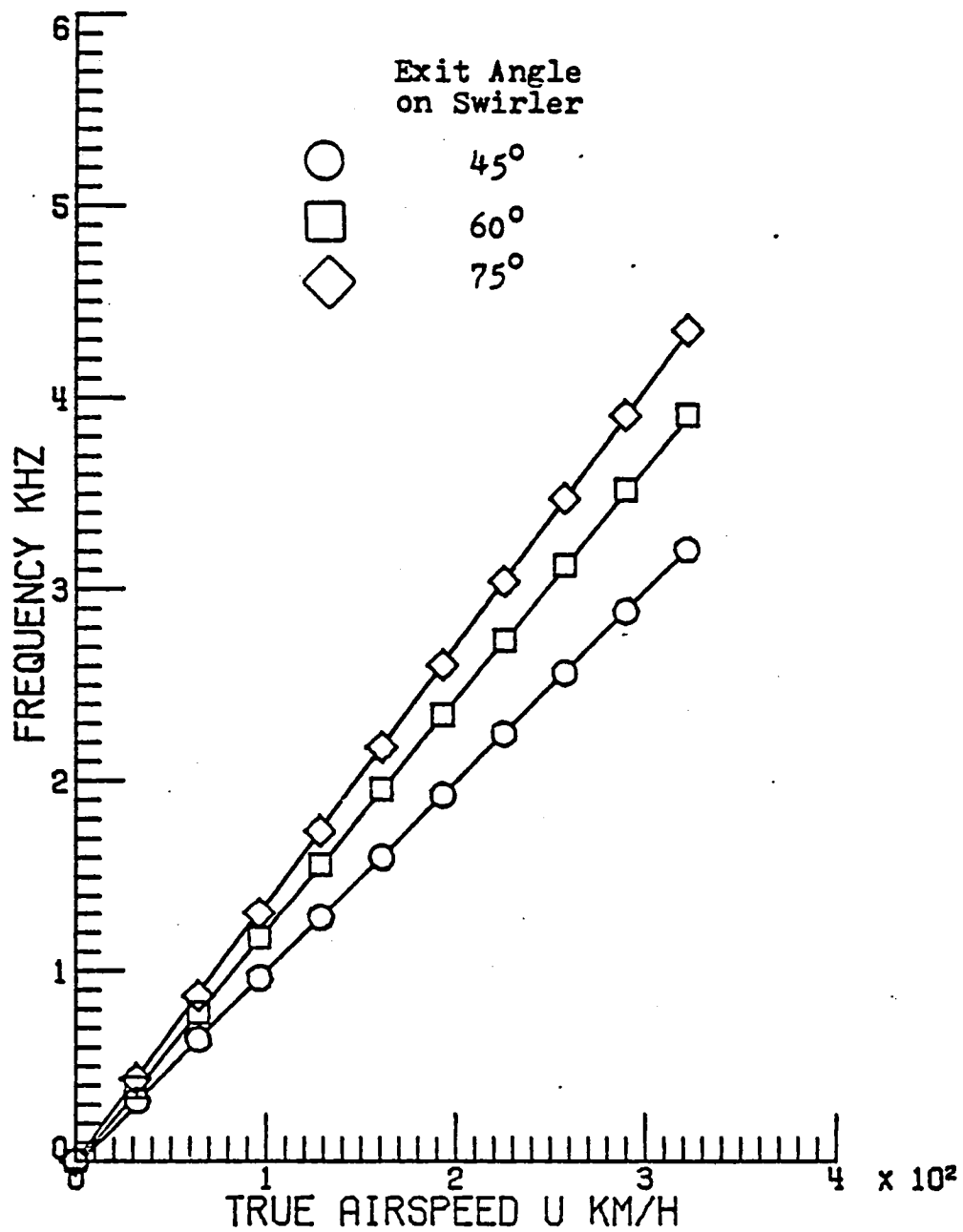
Figure 12.   True airspeed versus frequency response for sensor 1
with four-flute swirlers and wavenumber k = 1.
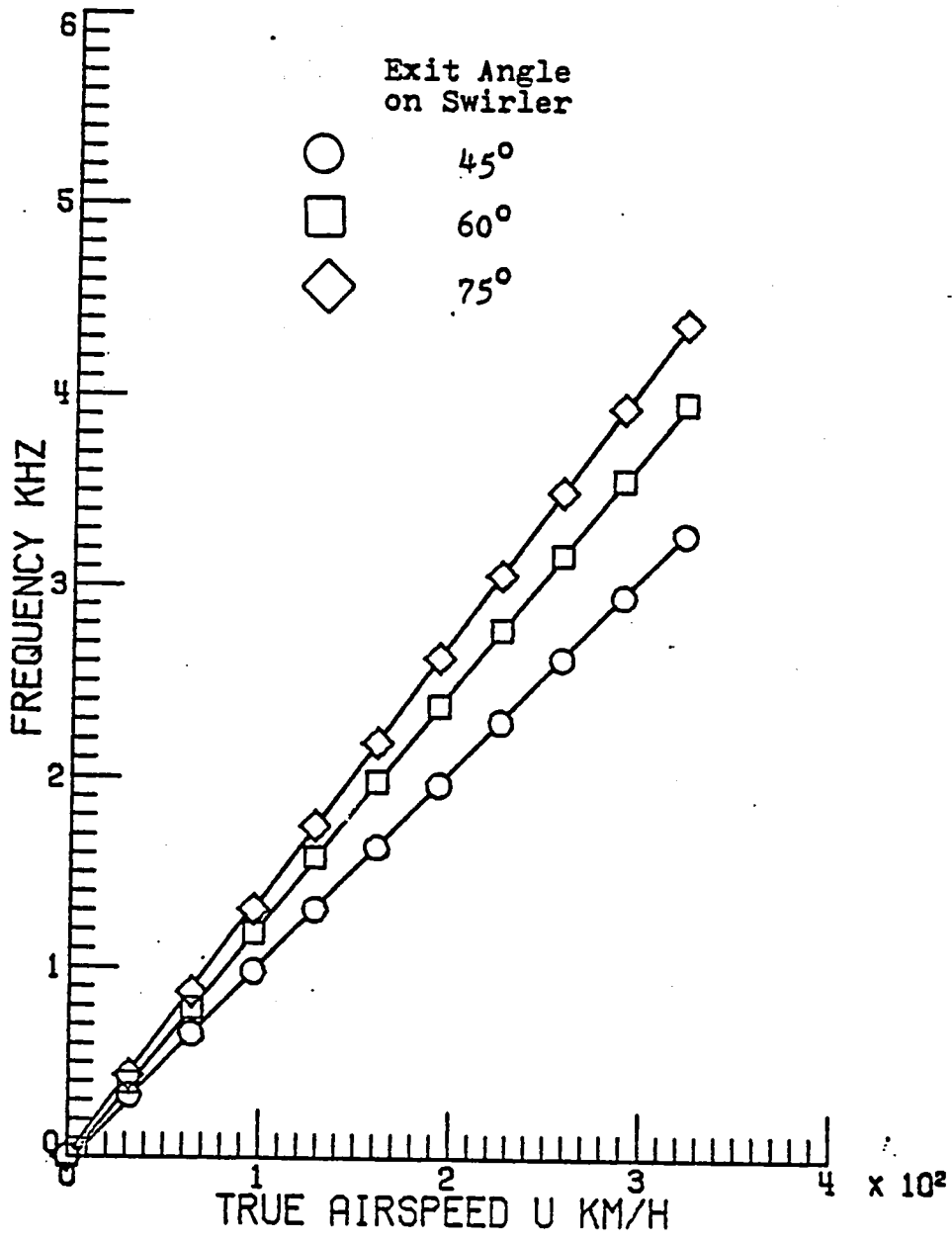
Figure 13. True airspeed versus frequency response for sensor 1
with four-flute swirlers and wavenumber k = 1.
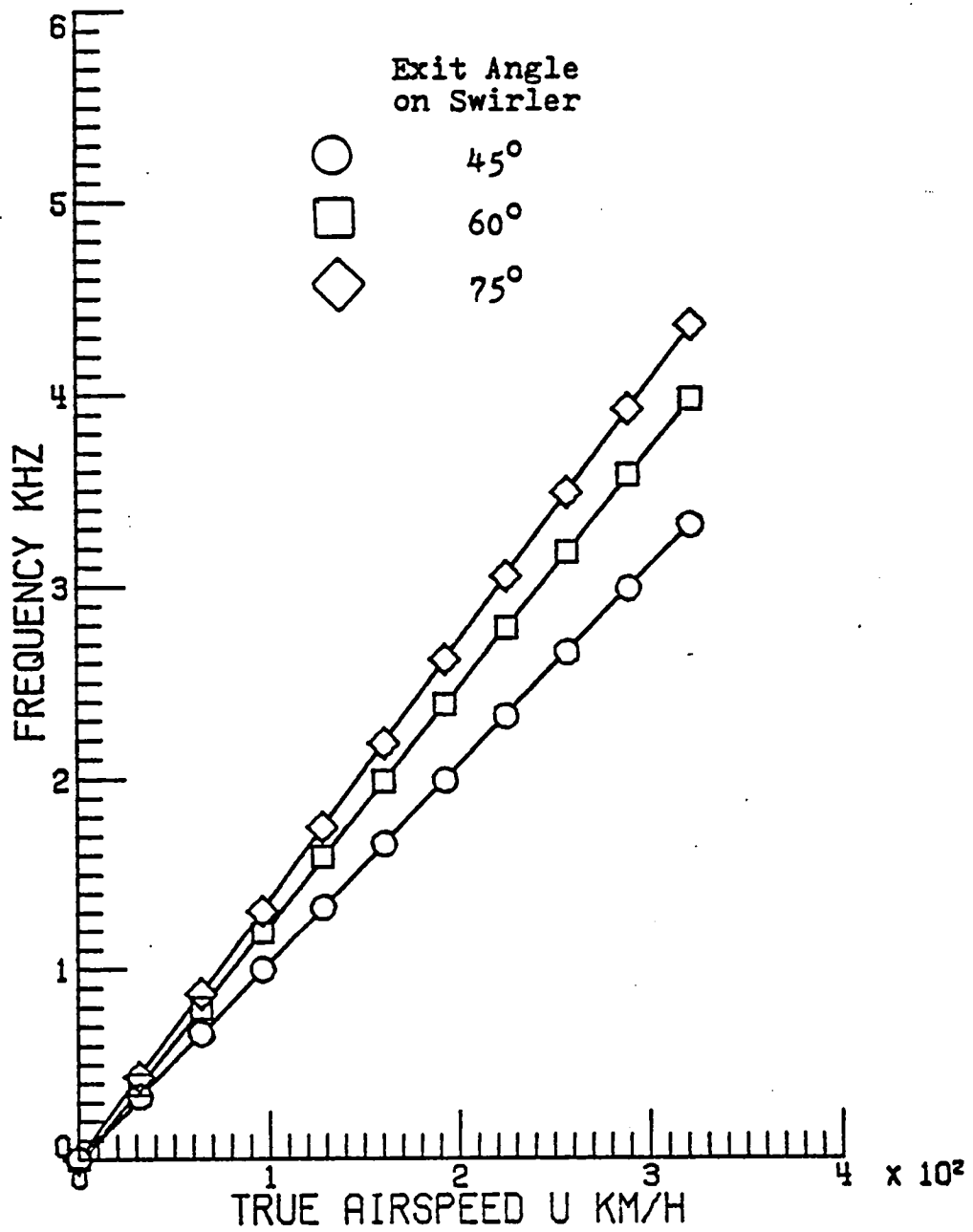
Figure 14. True airspeed versus frequency response for sensor 1
with four-flute swirlers and wavenumber k = 5.
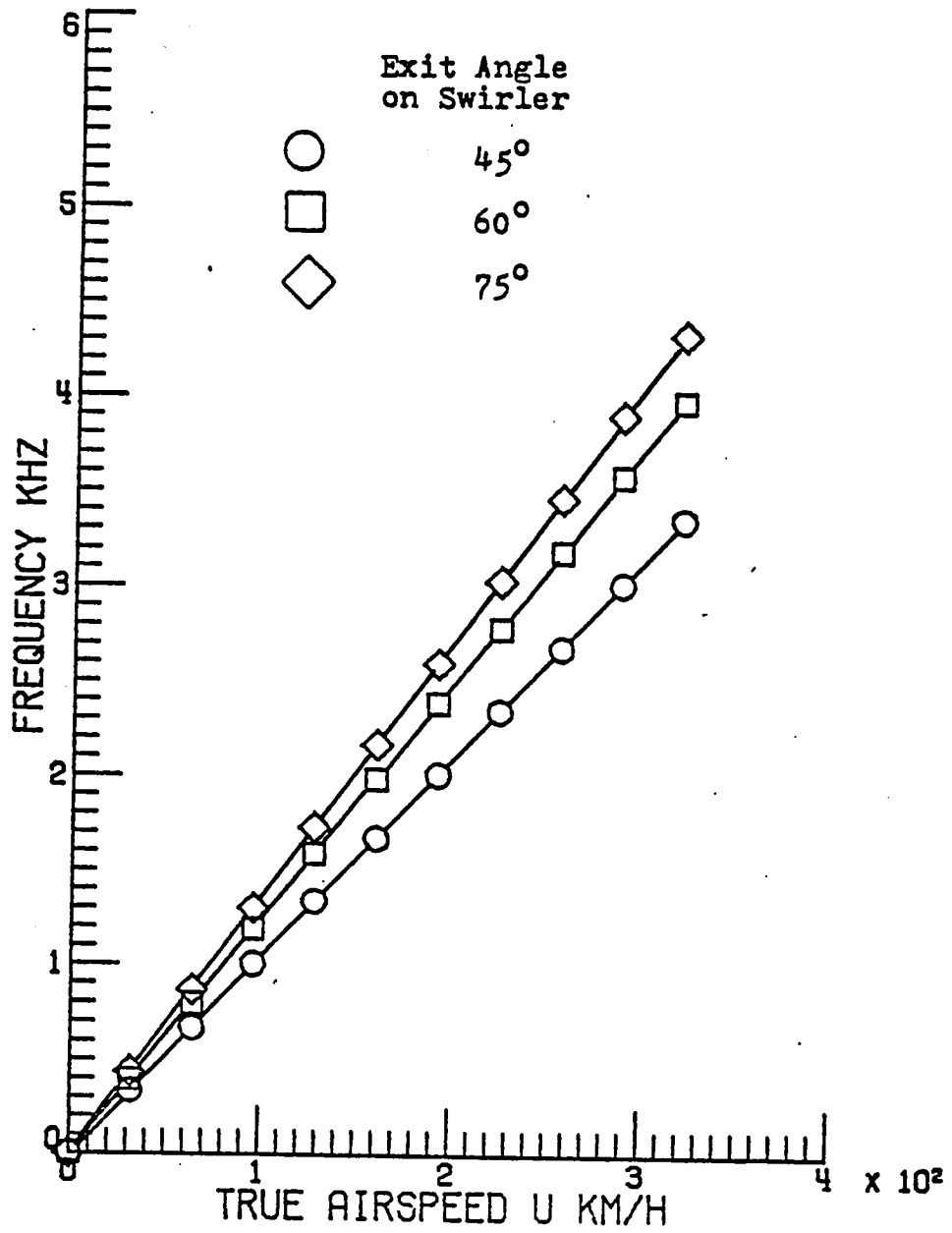
Figure 15. True airspeed versus frequency response for sensor 1
with four-flute swirlers and wavenumber k = 7.
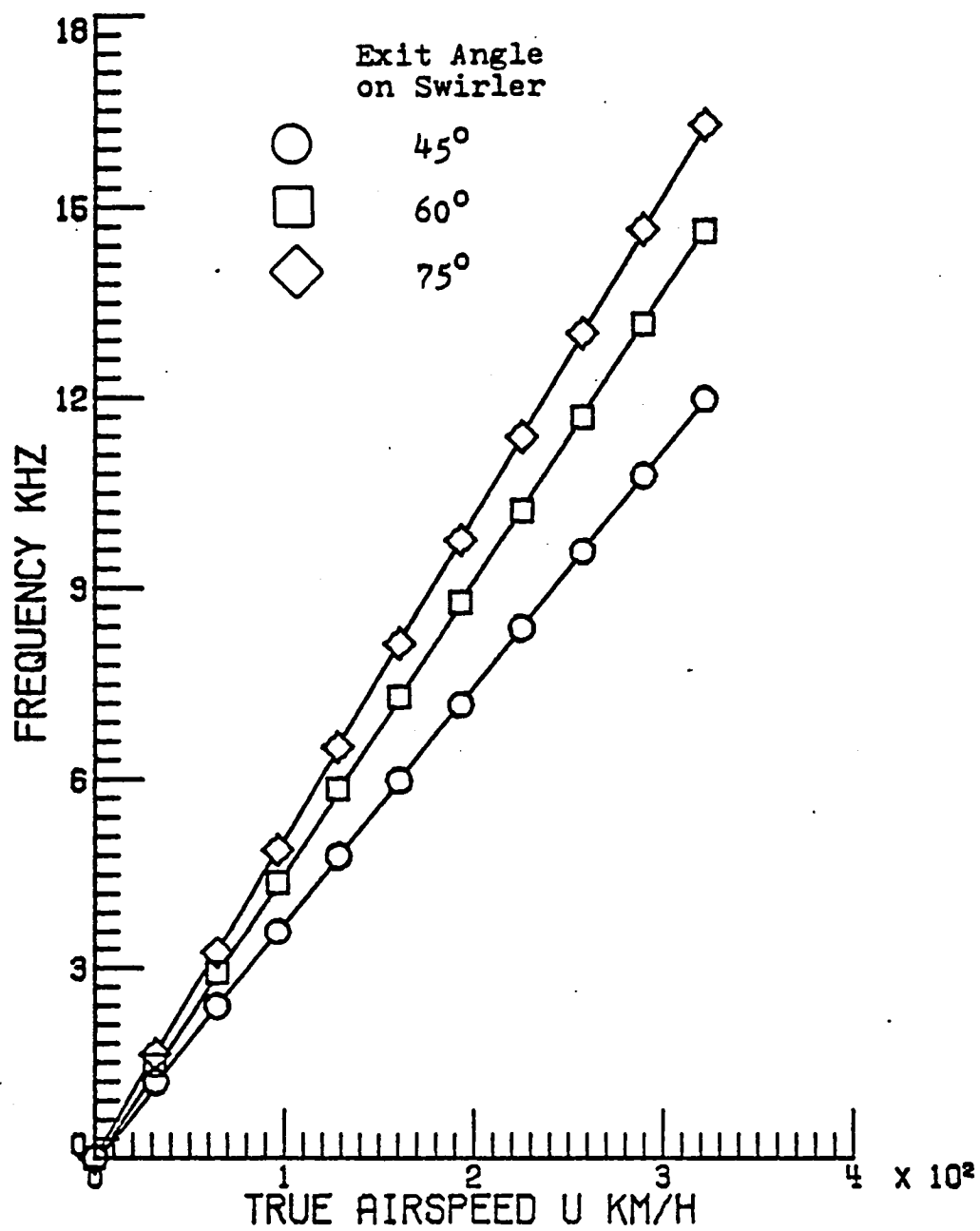
Figure 16. True airspeed versus frequency response for sensor 2
with swirlers having two flutes and various exit angles.
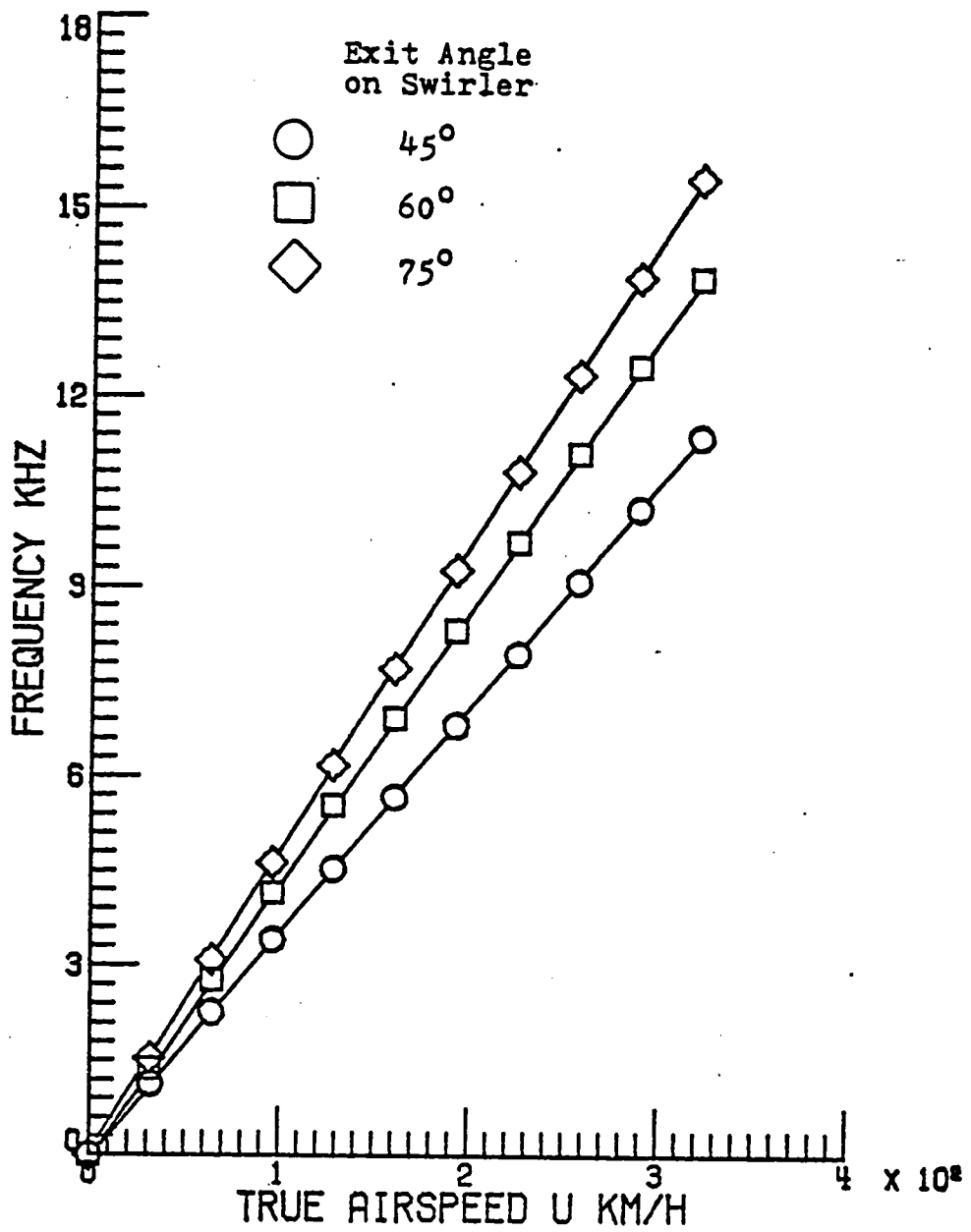
Figure 17. True airspeed versus frequency response for sensor 2 with swirlers having three flutes and various exit angles.
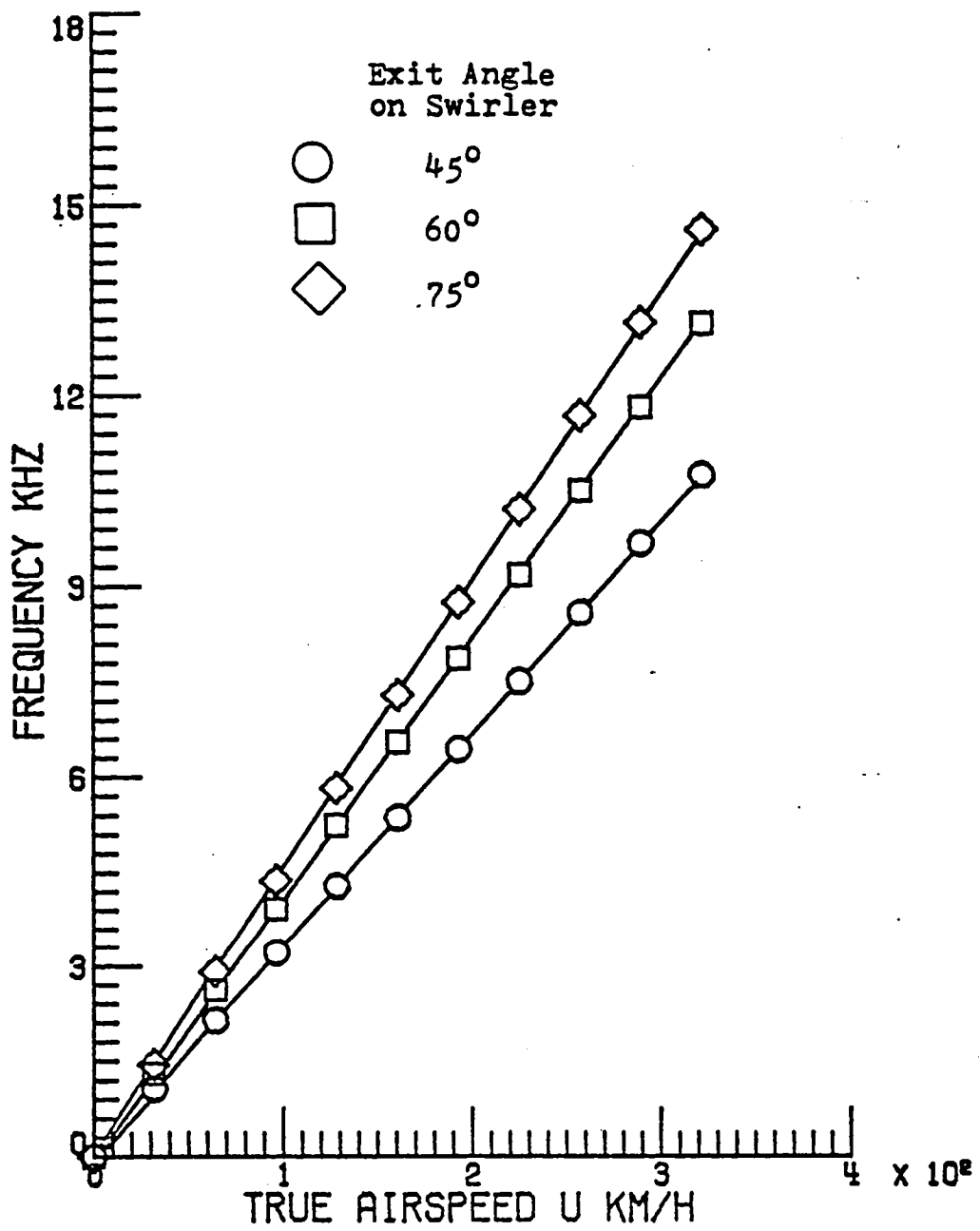
Figure 18. True airspeed versus frequency response for sensor 2 with swirlers having four flutes and various exit angles.
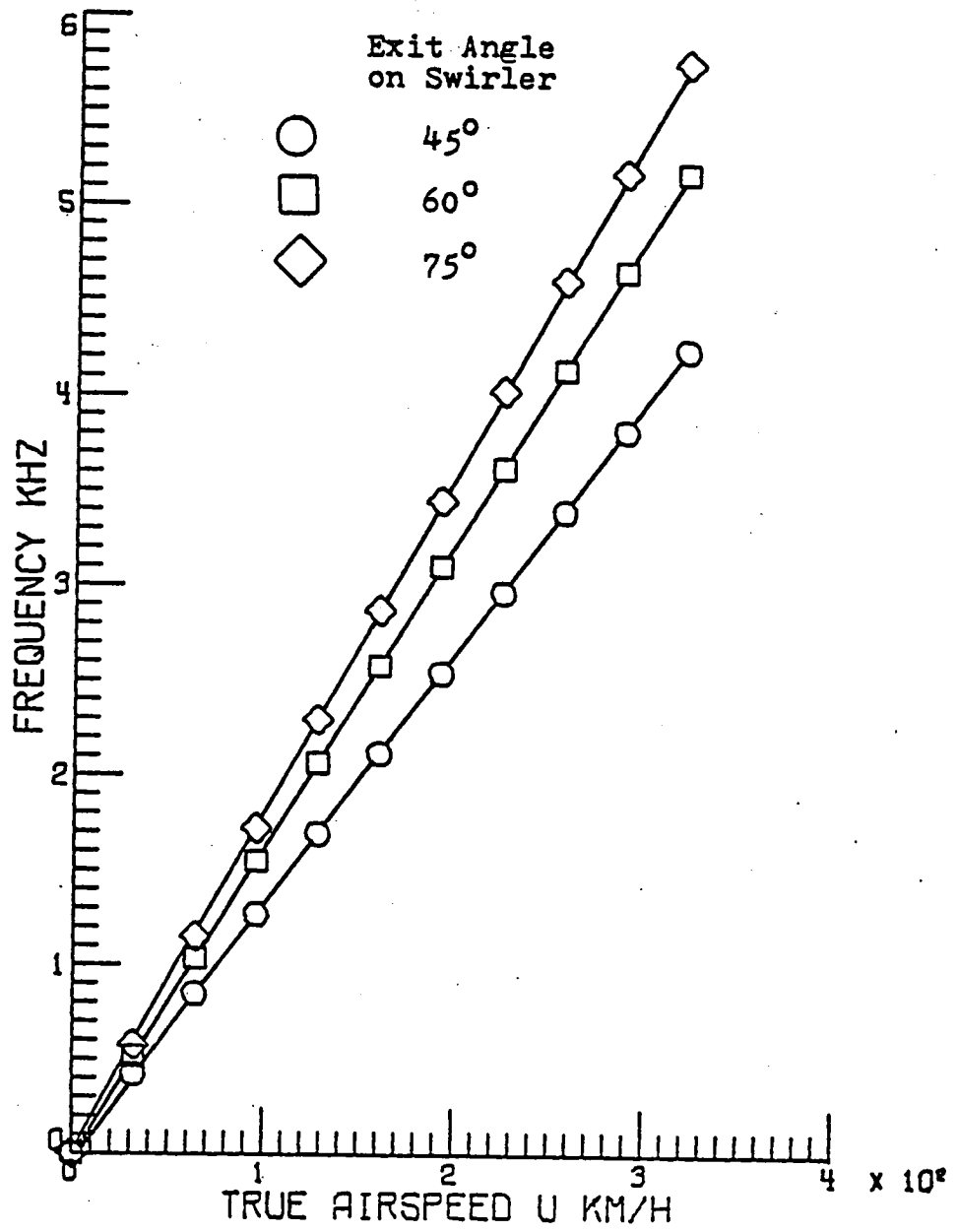
Figure 19. True airspeed versus frequency response for sensor 3 with swirlers having two flutes and various exit angles.
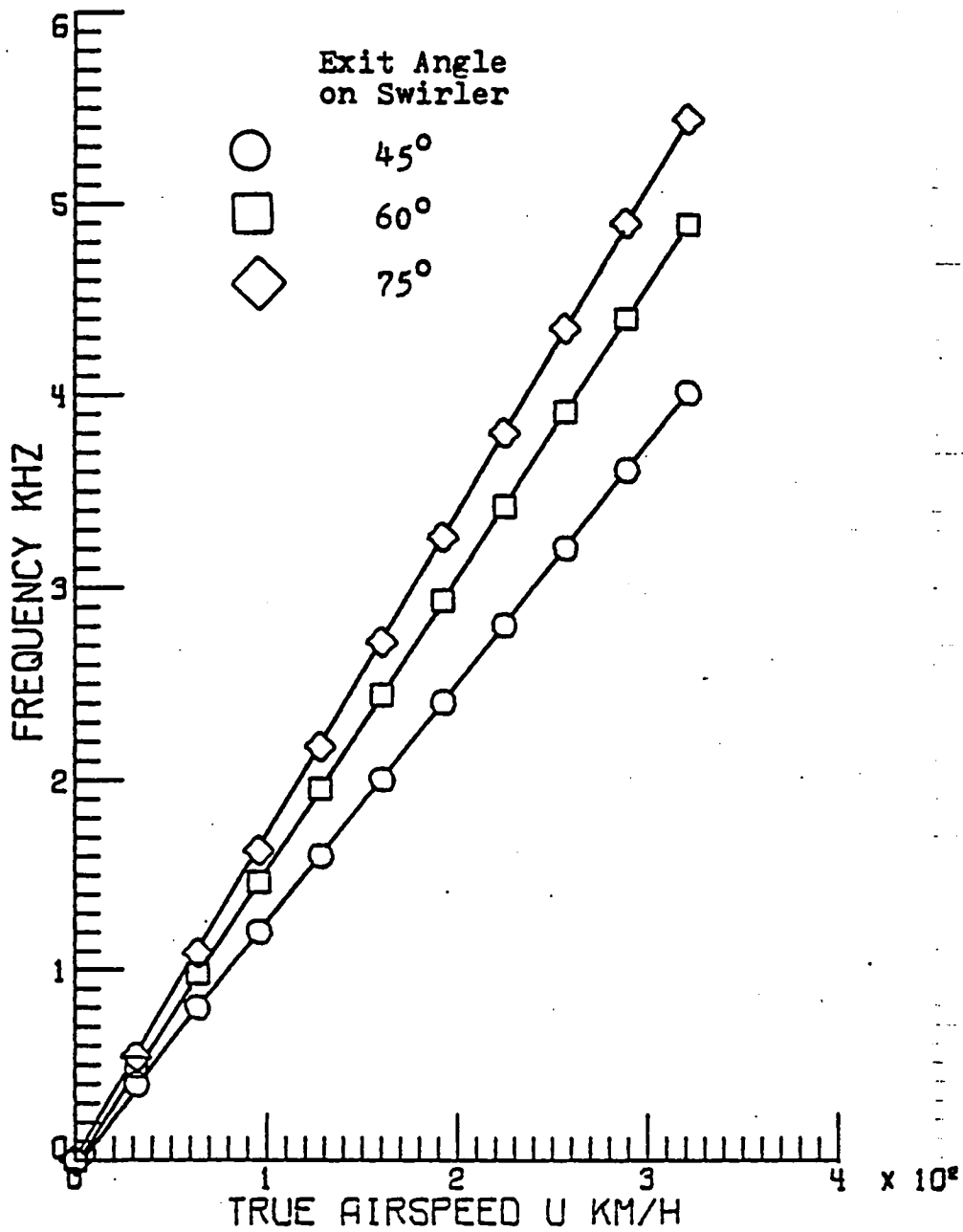
Figure 20. True airspeed versus frequency response for sensor 3 with
            swirlers having three flutes and various exit angles.
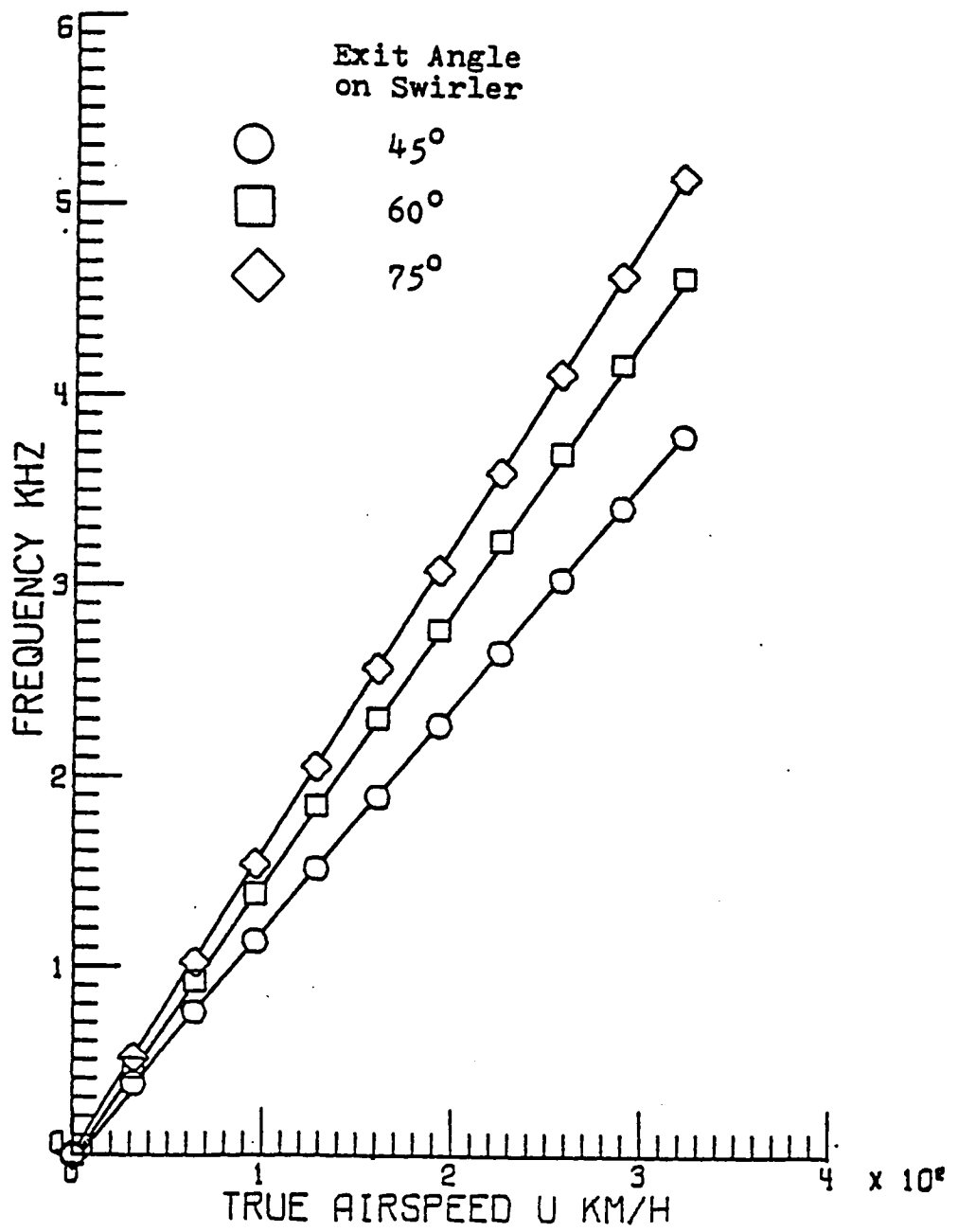
Figure 21. True airspeed versus frequency response for sensor 3 with swirlers having four flutes and various exit angles.
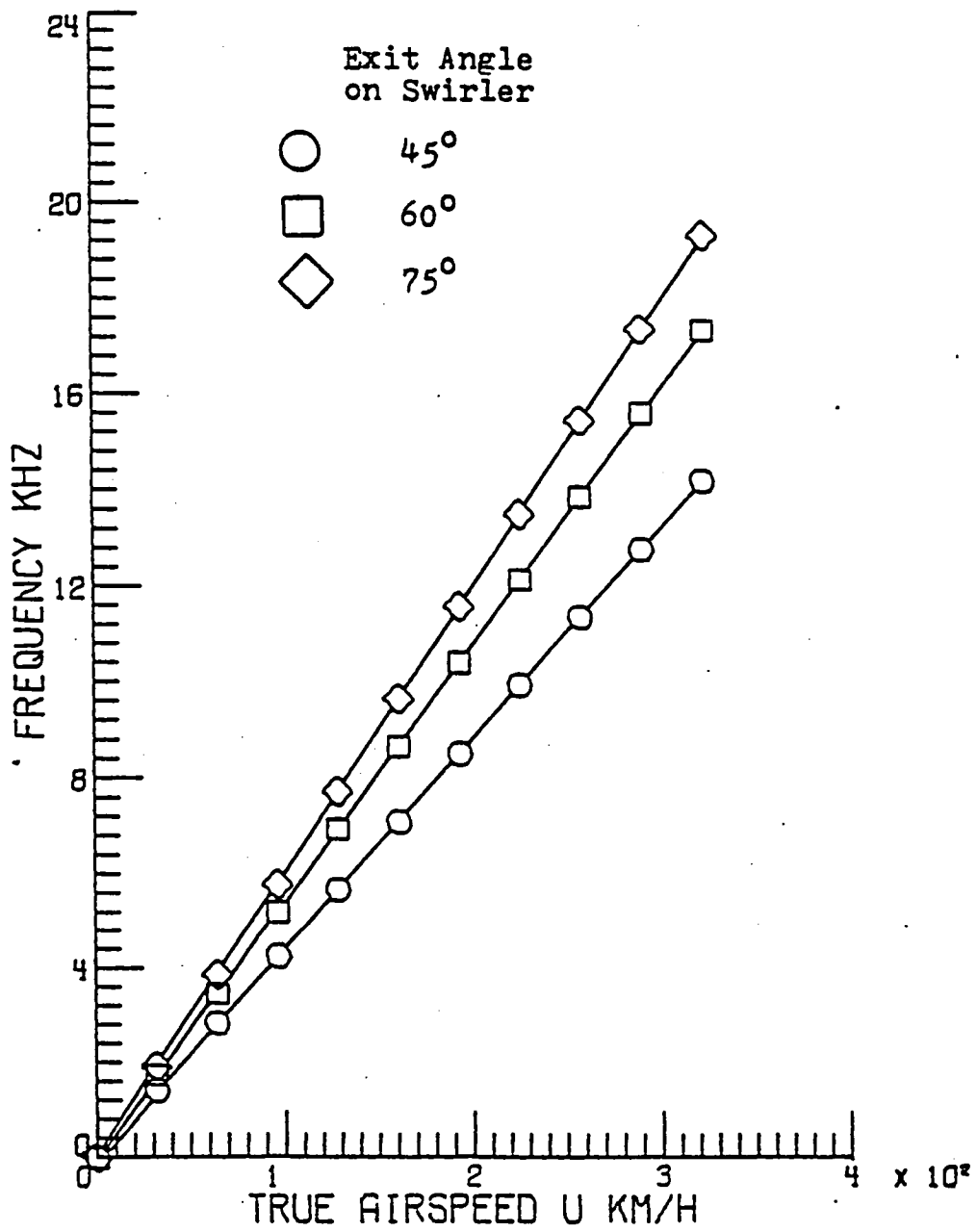
Figure 22. True airspeed versus frequency response for sensor 4 with swirlers having two flutes and various exit angles.
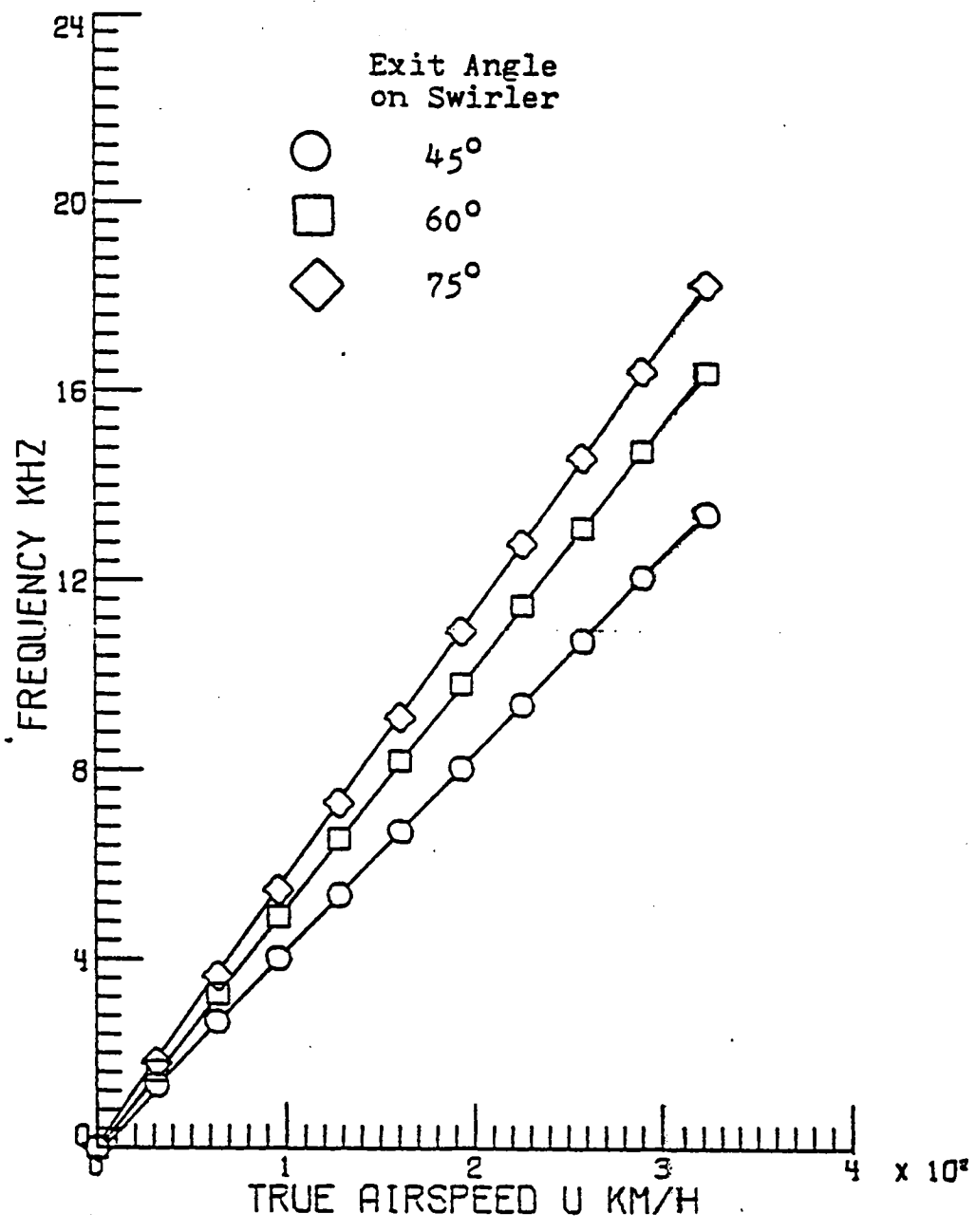
Figure 23.   True airspeed versus frequency response for sensor 4 with swirlers having three flutes and various exit angles.
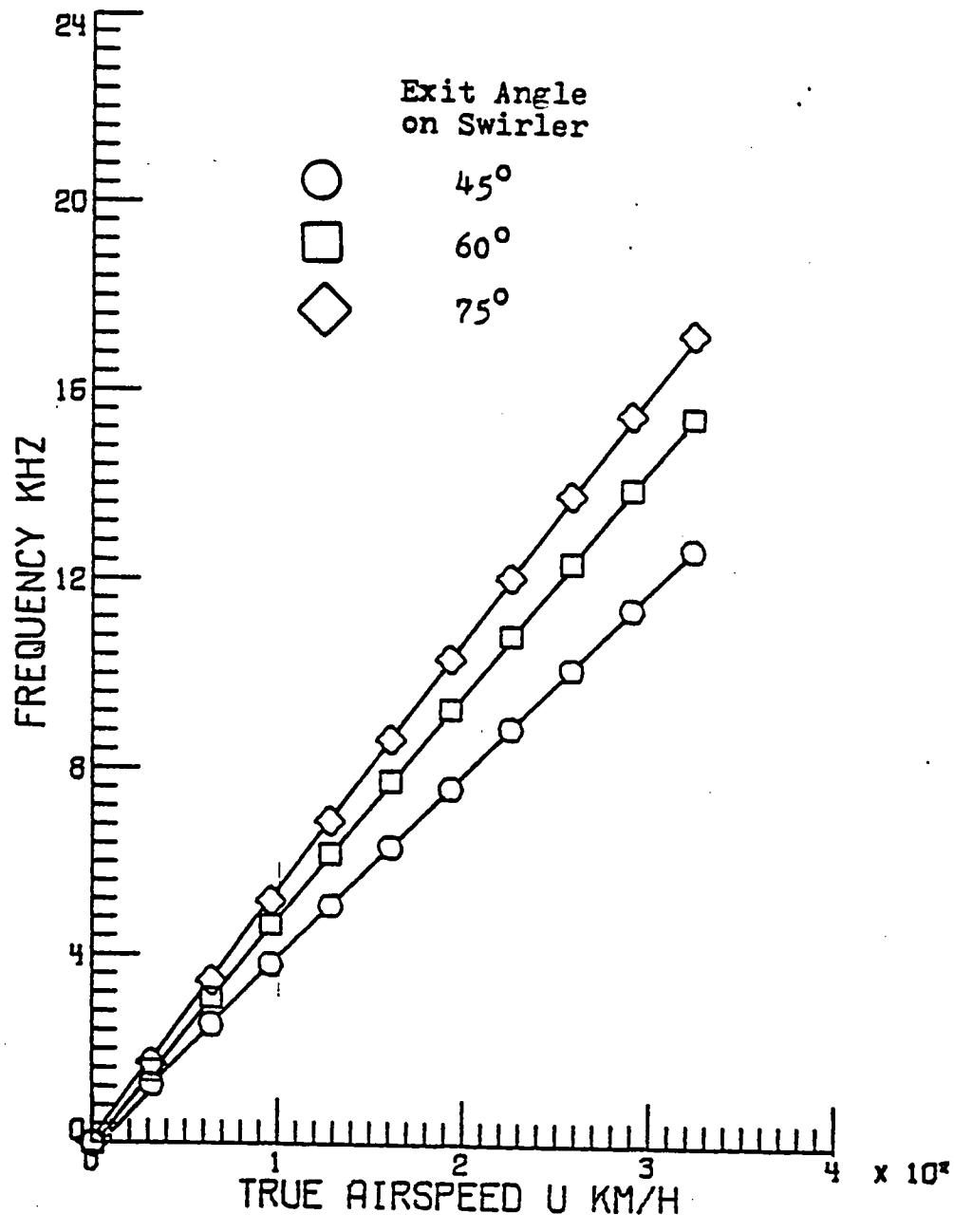
Figure 24.   True airspeed versus frequency response for sensor 4 with
swirlers having four flutes and various exit angles.
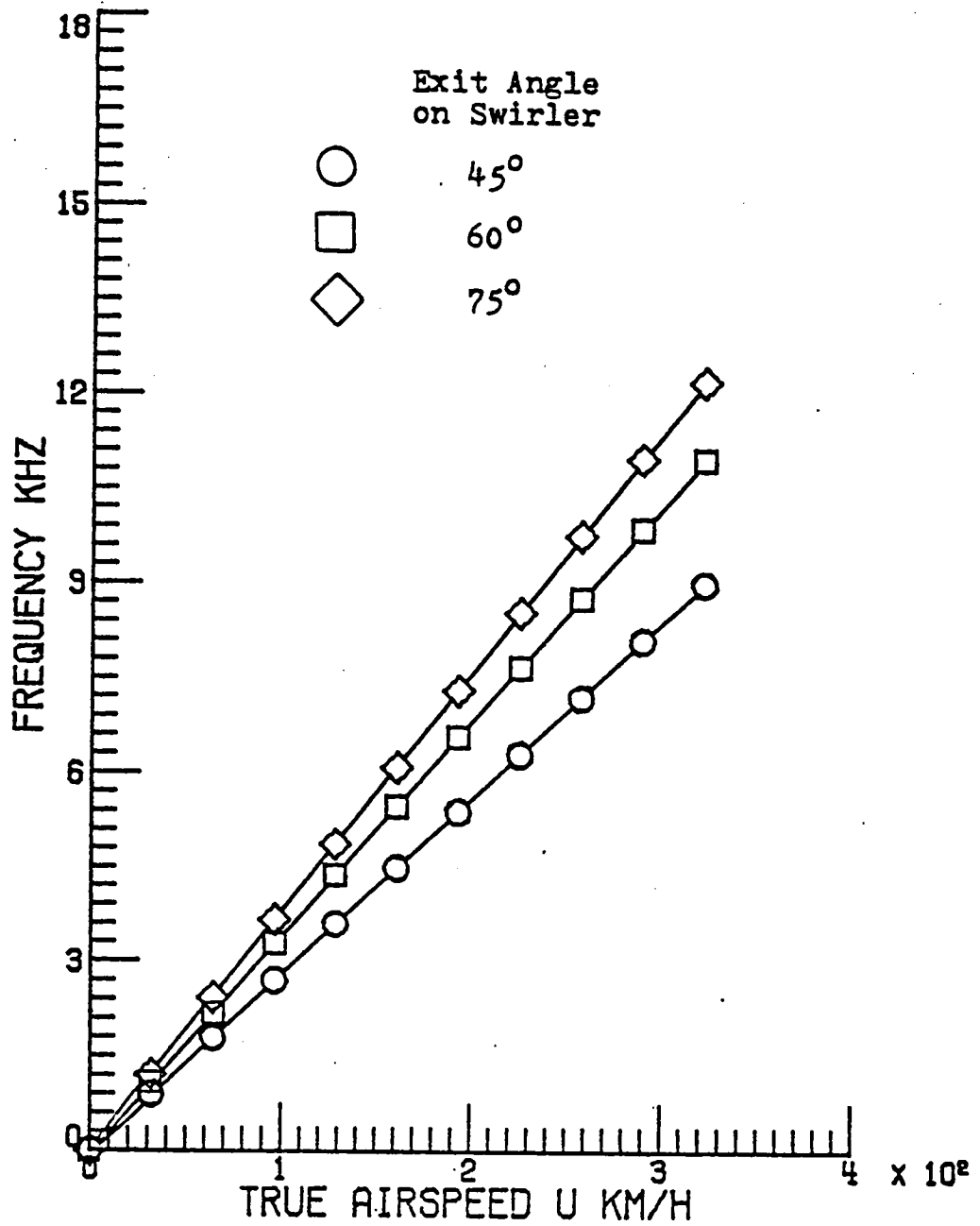
Figure 25. True airspeed versus frequency response for sensor 5 with
swirlers having two flutes and various exit angles.
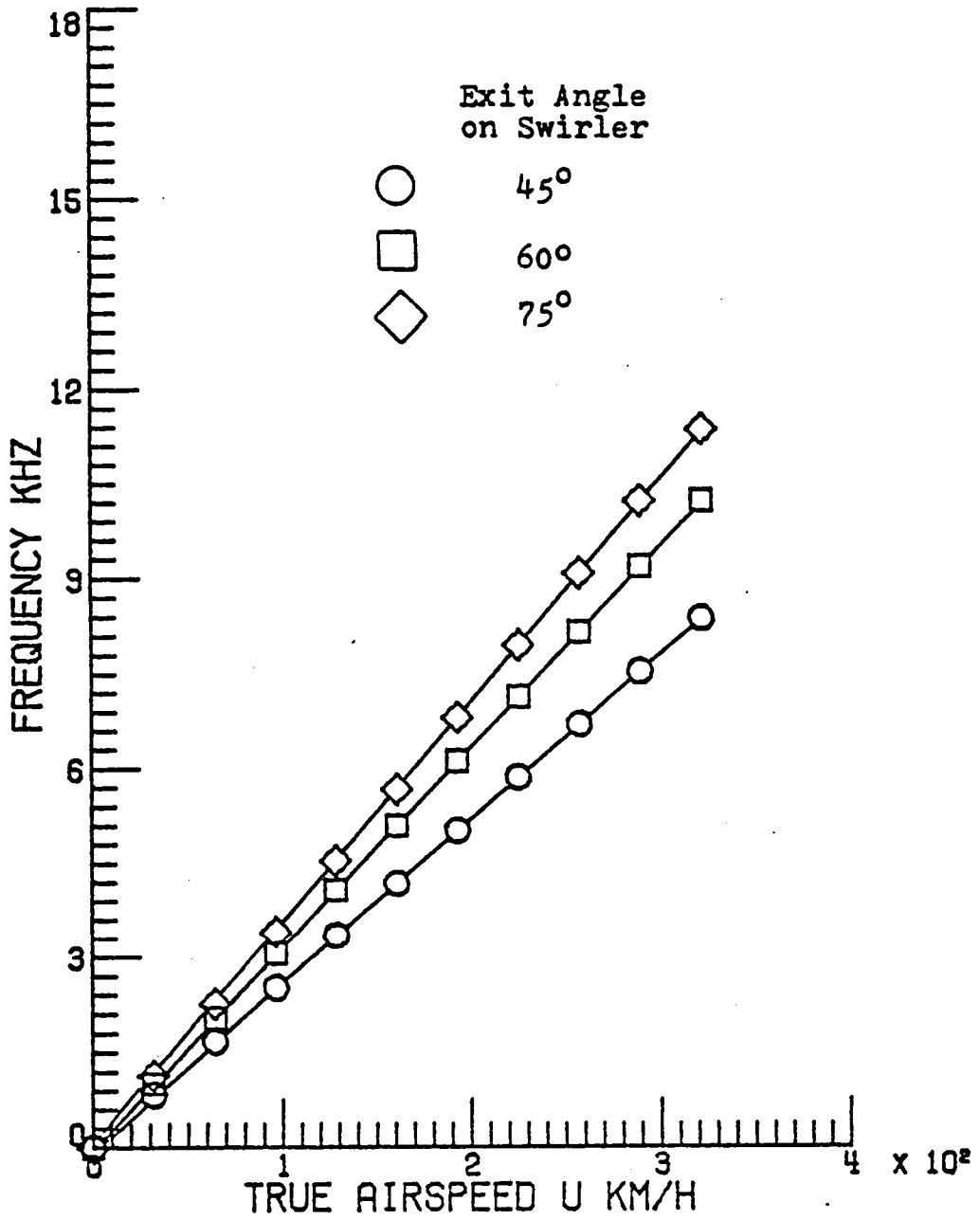
Figure 26. True airspeed versus frequency response for sensor 5 with
swirlers having three flutes and various exit angles.
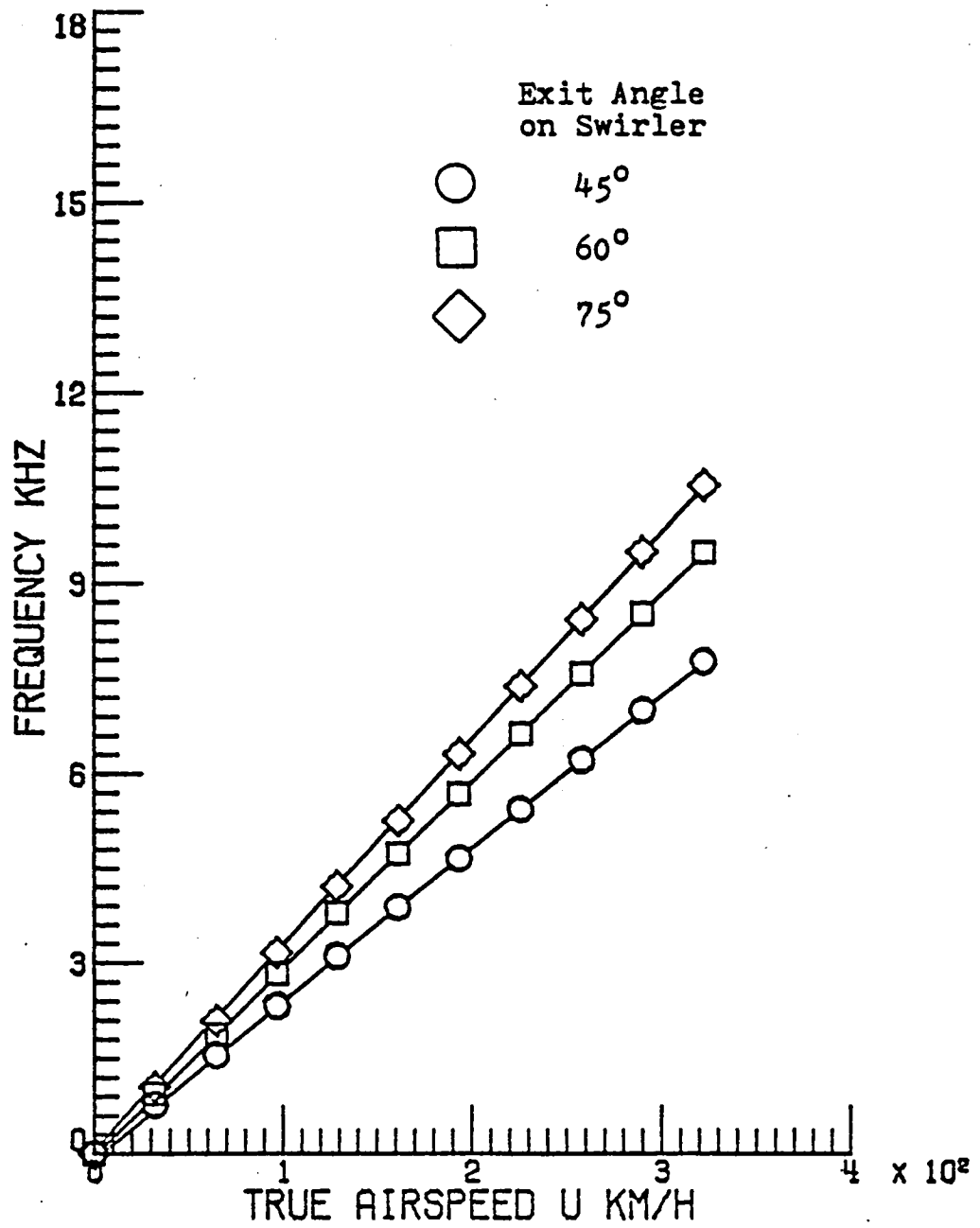
Figure 27. True airspeed versus frequency response for sensor 5 with swirlers having four flutes and various exit angles.
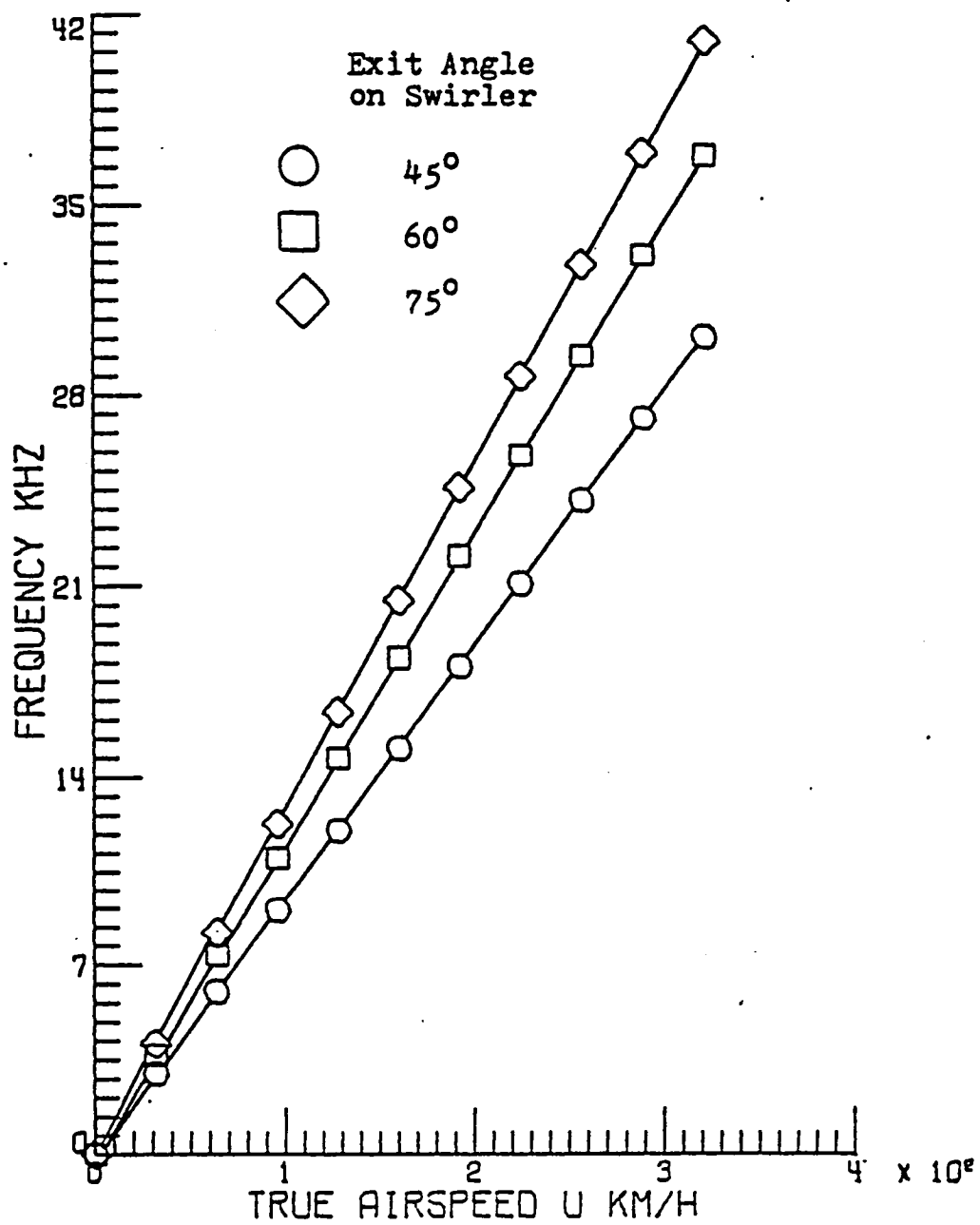
Figure 28. True airspeed versus frequency response for sensor 6 with swirlers having two flutes and various exit angles.
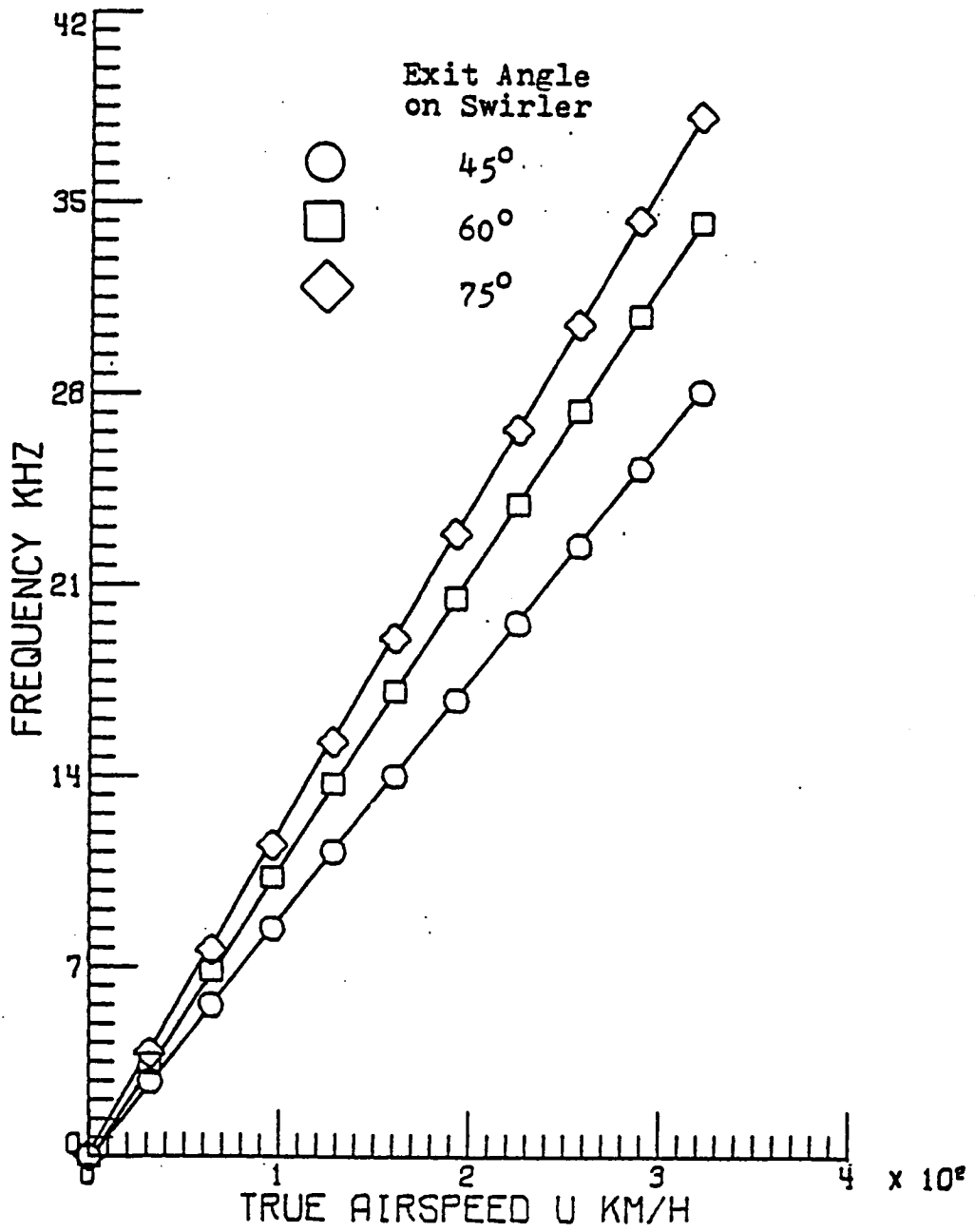
Figure 29. True airspeed versus frequency response for sensor 6 with swirlers having three flutes and various exit angles.
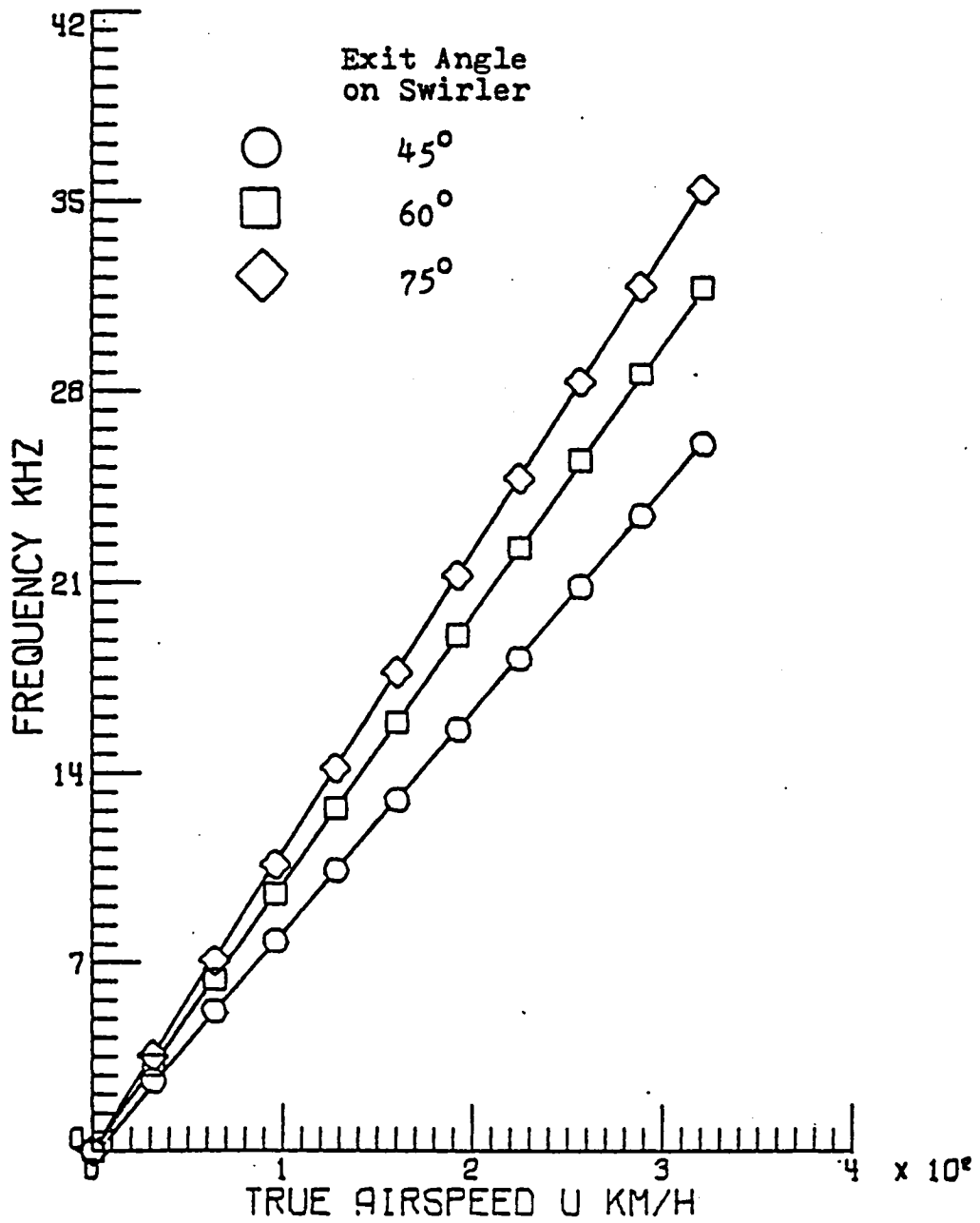
Figure 30. True airspeed versus frequency response for sensor 6 with
swirlers having four flutes and various exit angles.
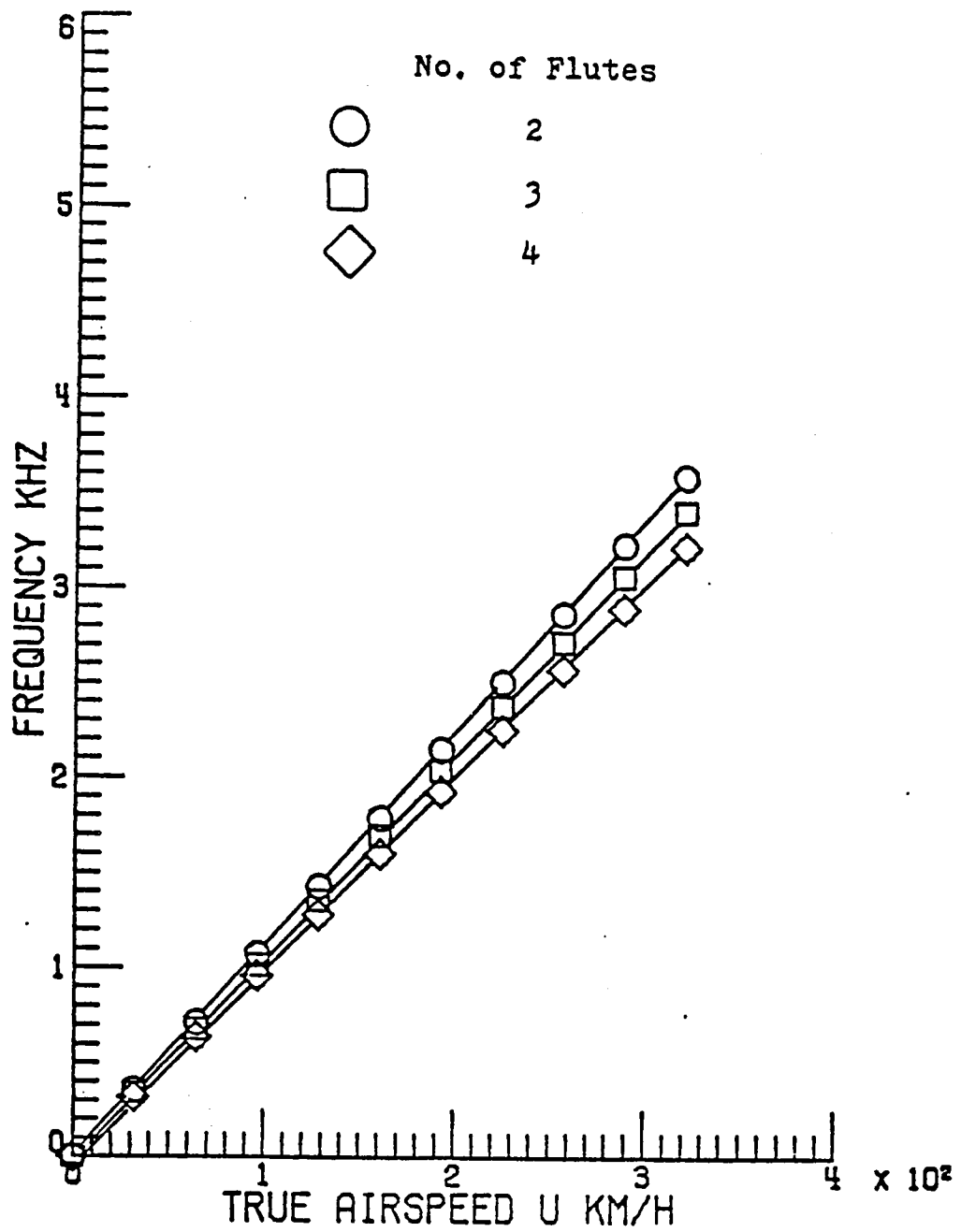
Figure 31.   True airspeed versus frequency response for sensor 1 with
swirlers having 45° exit angle and various flutes.
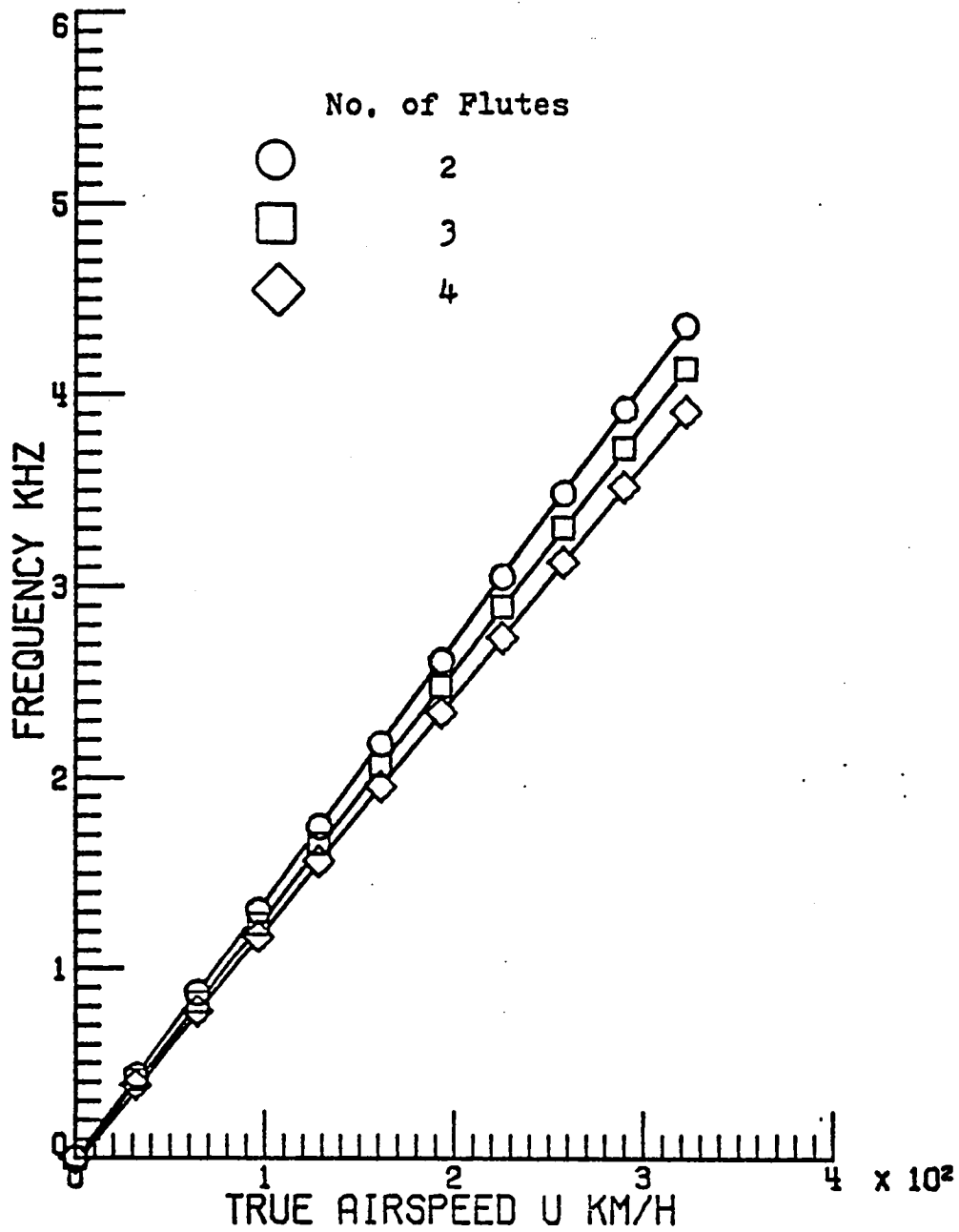
Figure 32.   True airspeed versus frequency response for sensor 1 with
swirlers having 60° exit angle and various flutes.
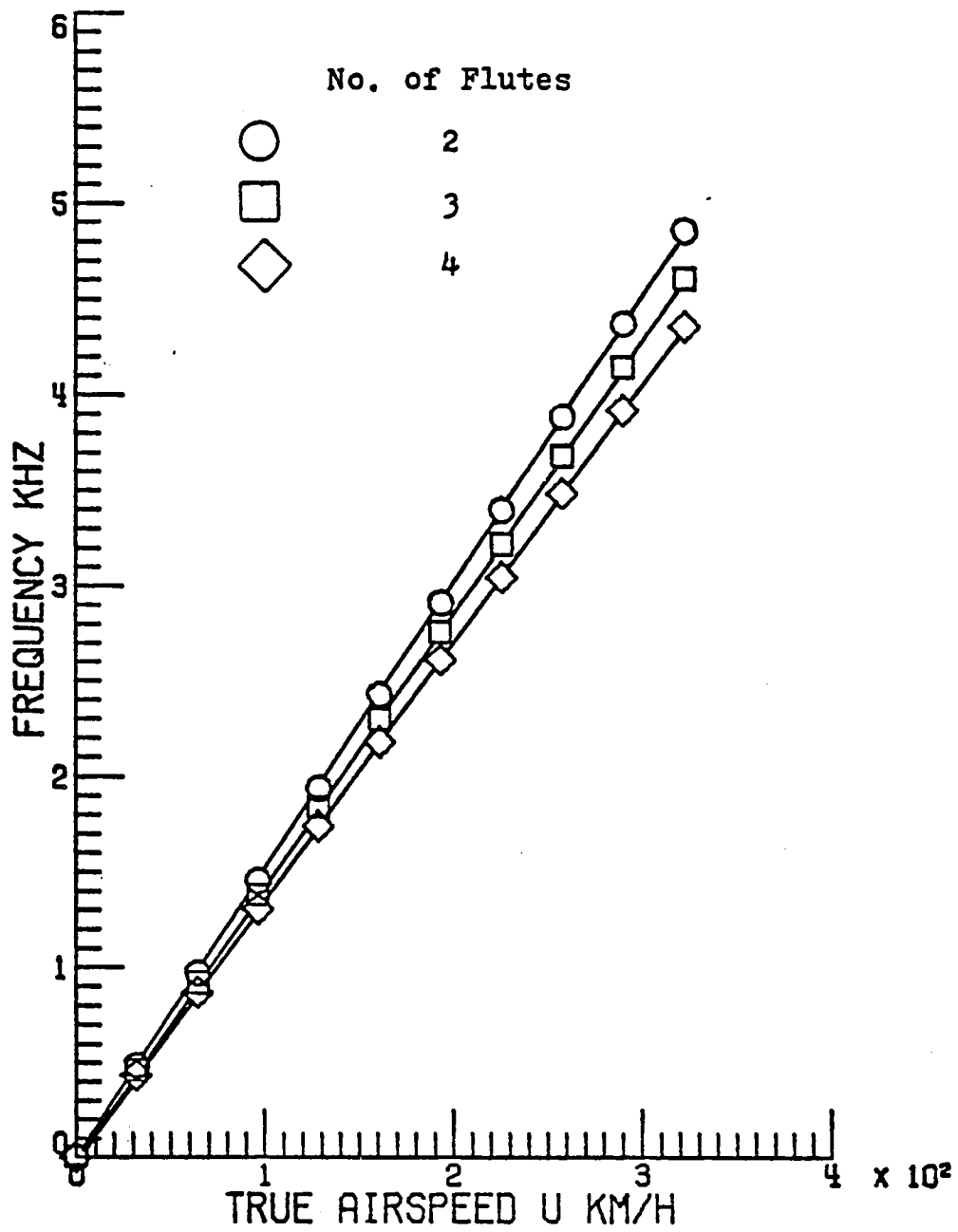
Figure 33. True airspeed versus frequency response for sensor 1 with
swirlers having 75° exit angle and various flutes.
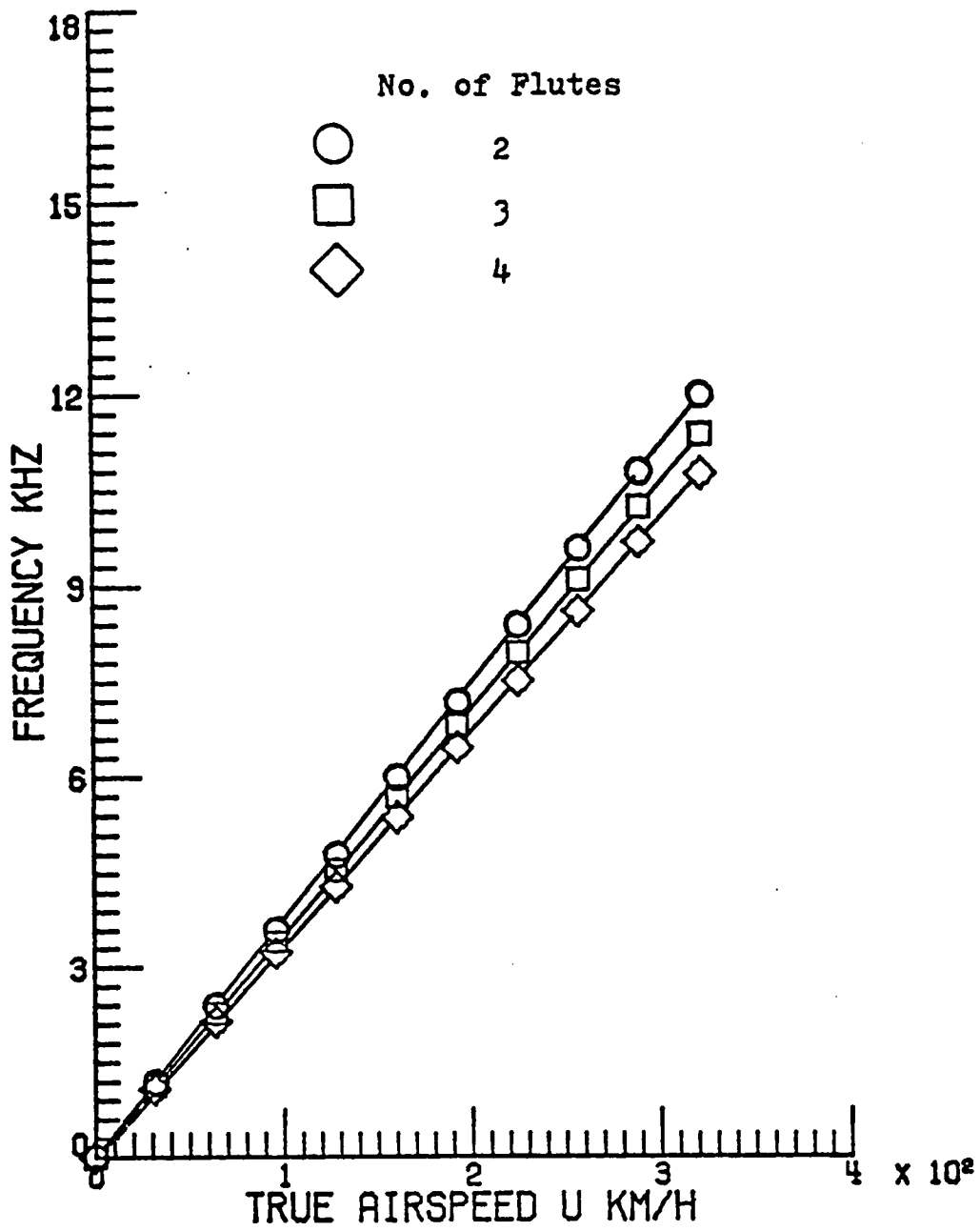
Figure 34. True airspeed versus frequency response for sensor 2 with
swirlers having 45° exit angle and various flutes.
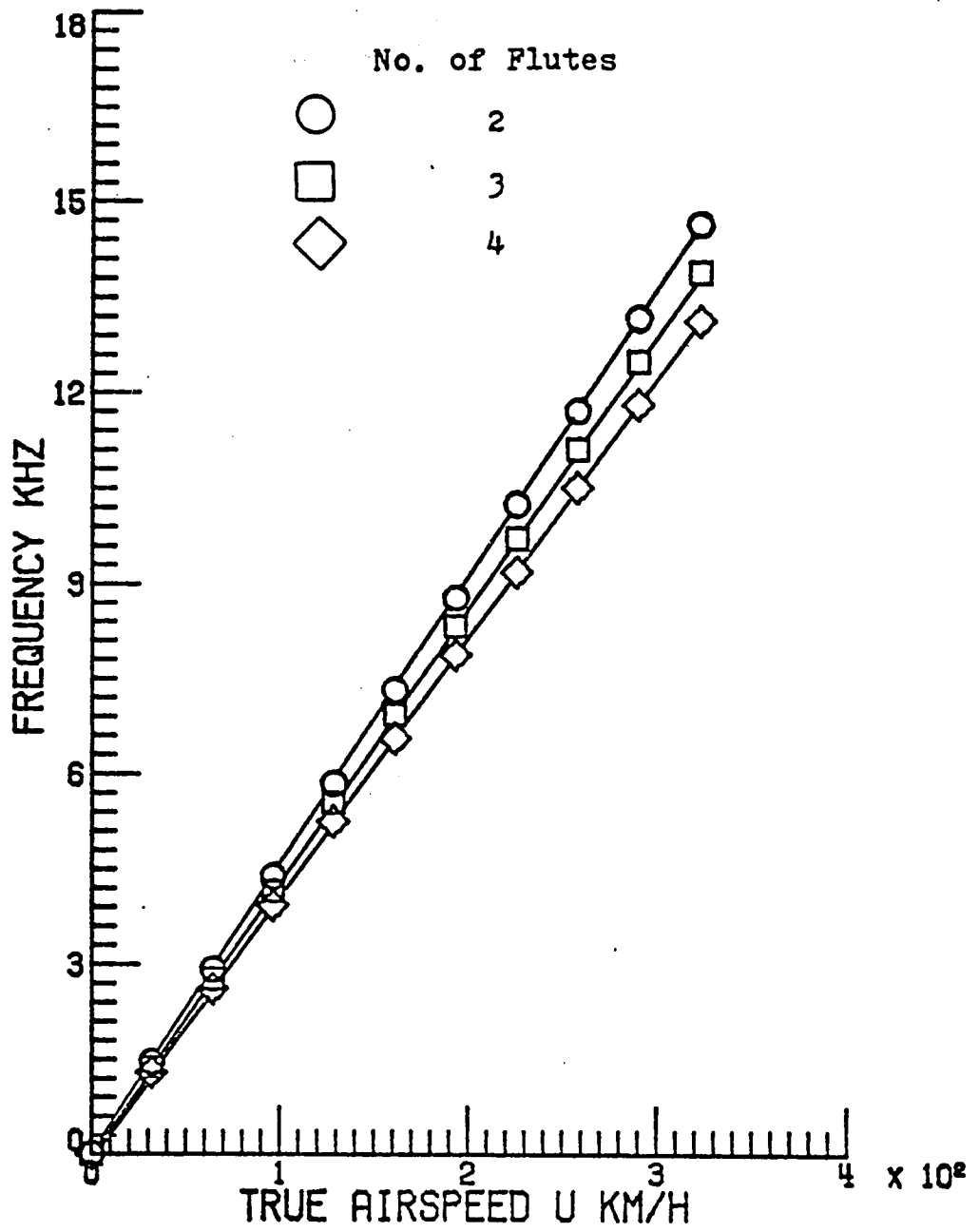
Figure 35. True airspeed versus frequency response for sensor 2 with swirlers having 60° exit angle and various flutes.
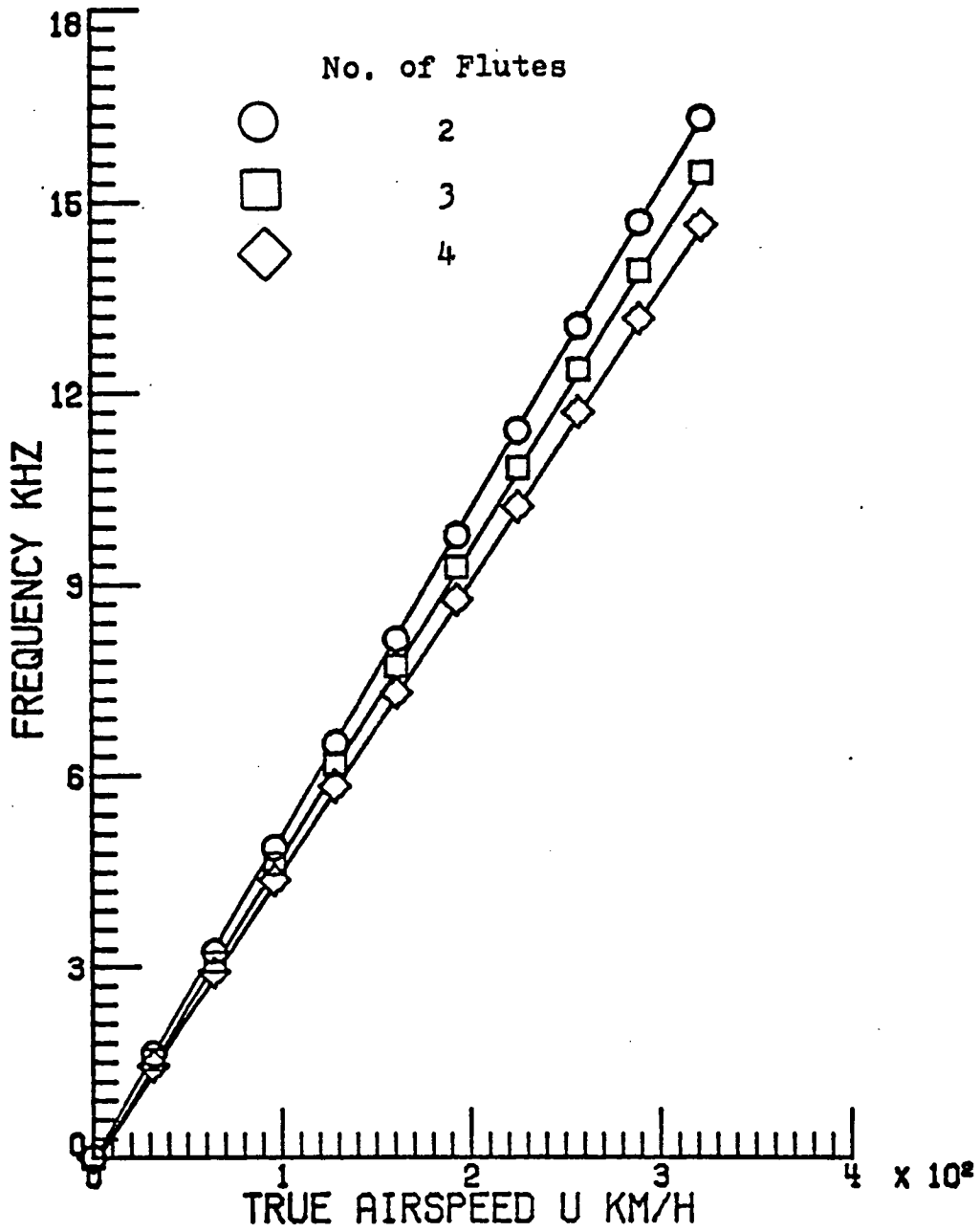
Figure 36. True airspeed versus frequency response for sensor 2 with
swirlers having 75° exit angle and various flutes.
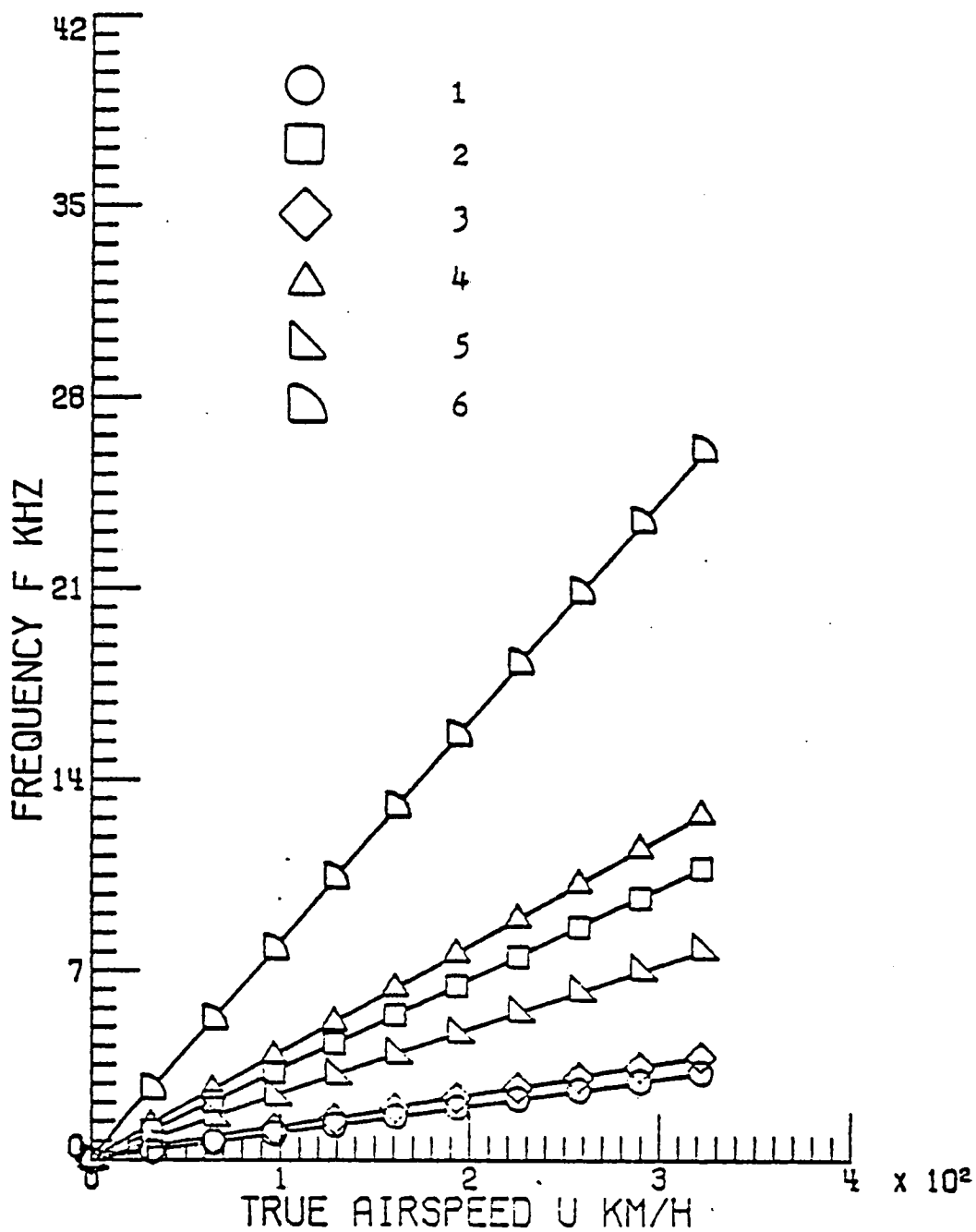
Figure 37. Comparison of size variation in the precessional flow region D_3 with 4 flutes and exit angle 45° swirler.
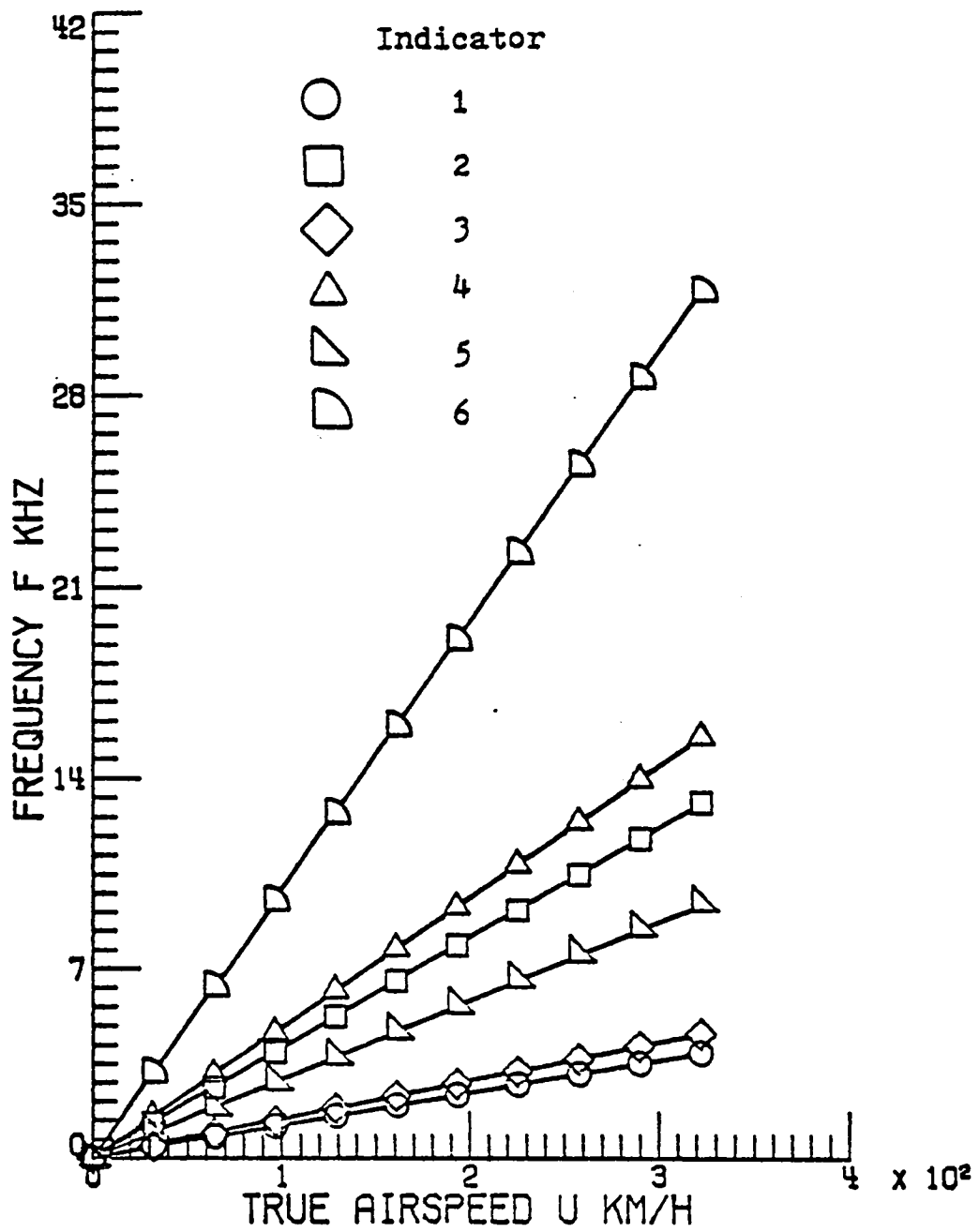
Figure 38. Comparison of size variation in the precessional flow region
D_3 with 4 flutes and exit angle 60° swirler.

120
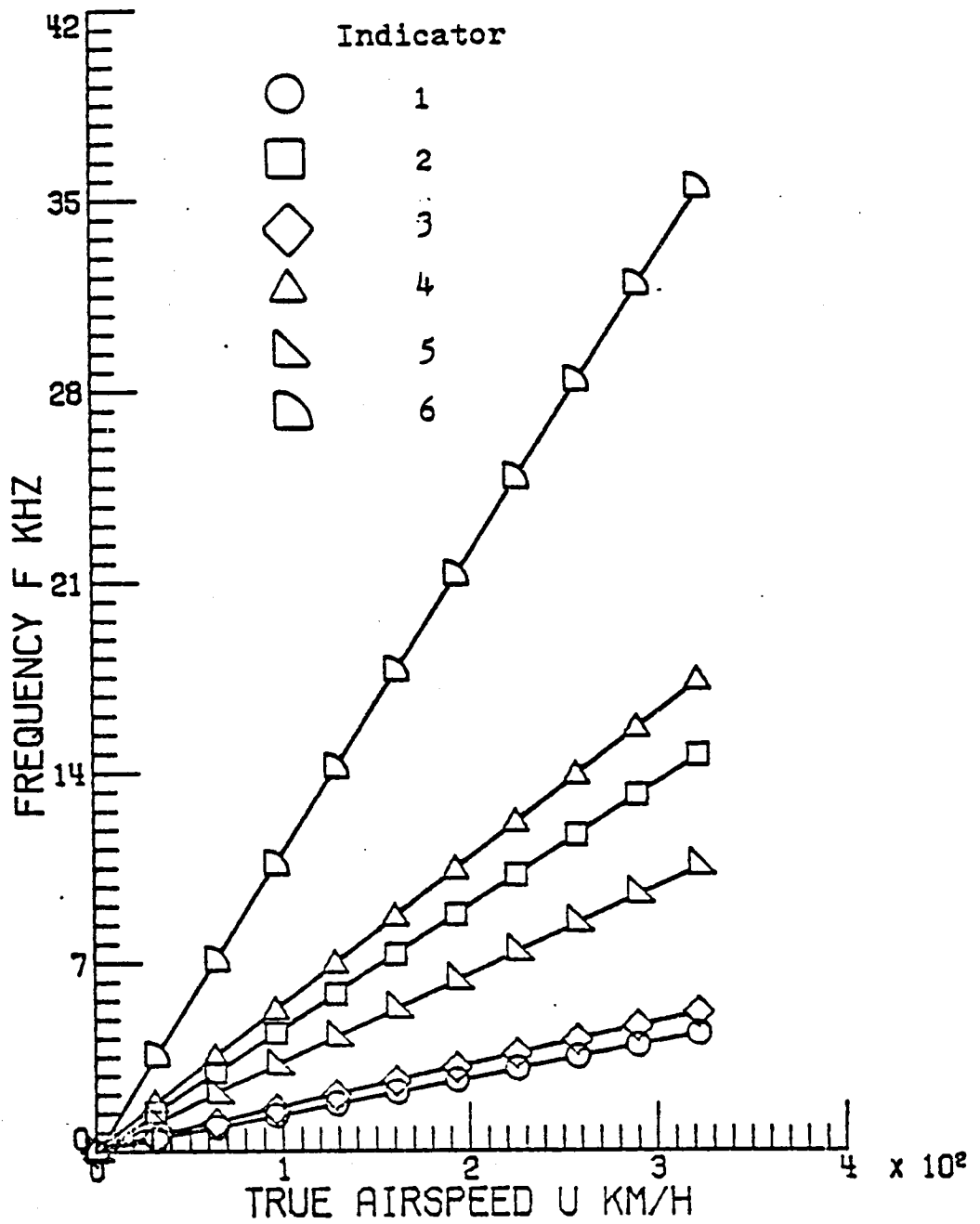
Figure 39. Comparison of size variation in the precessional flow region D_3 with 4 flutes and exit angle 75° swirler.
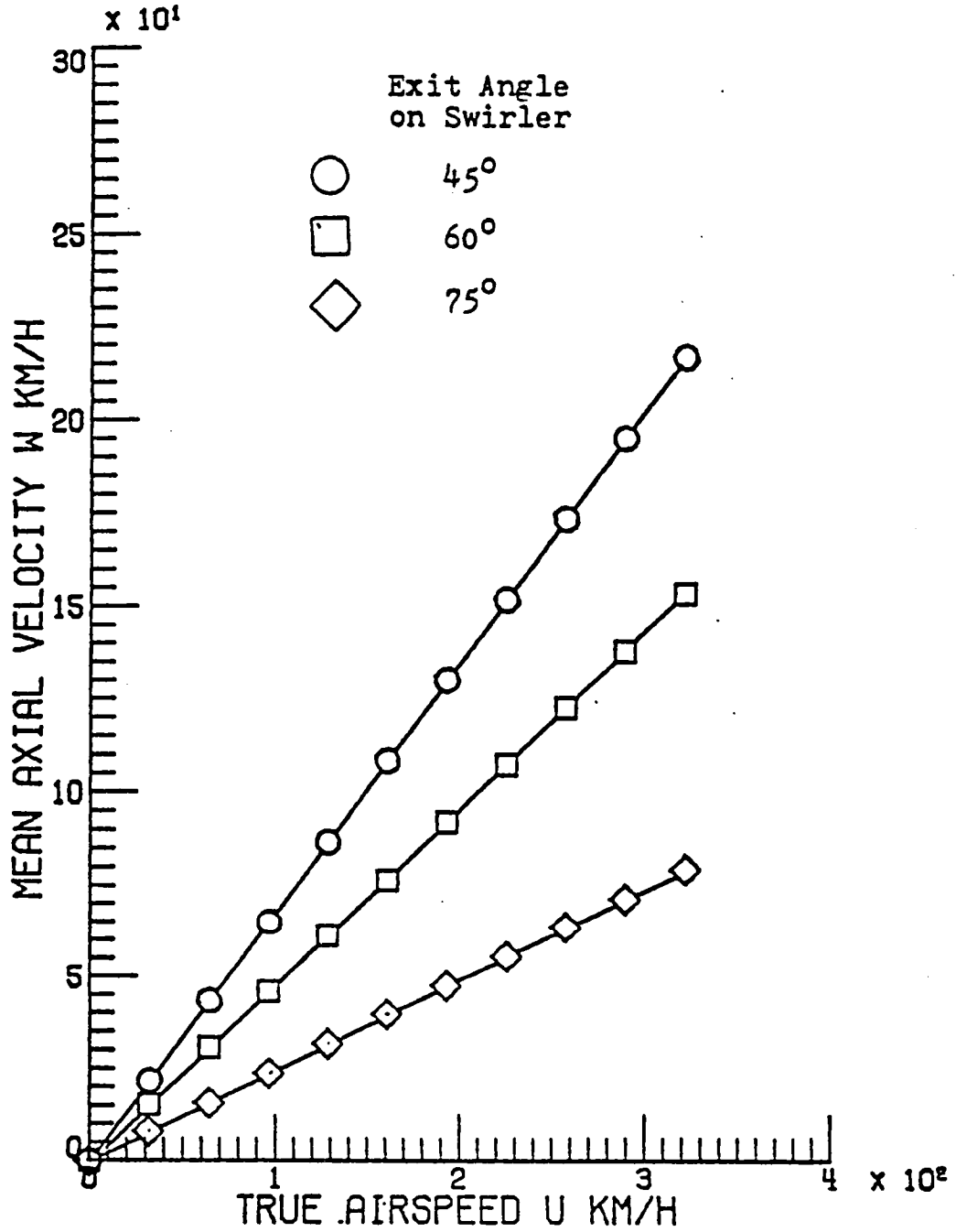
Figure 40. True airspeed versus mean axial velocity for sensor 1 with swirlers having four flutes and various exit angles.
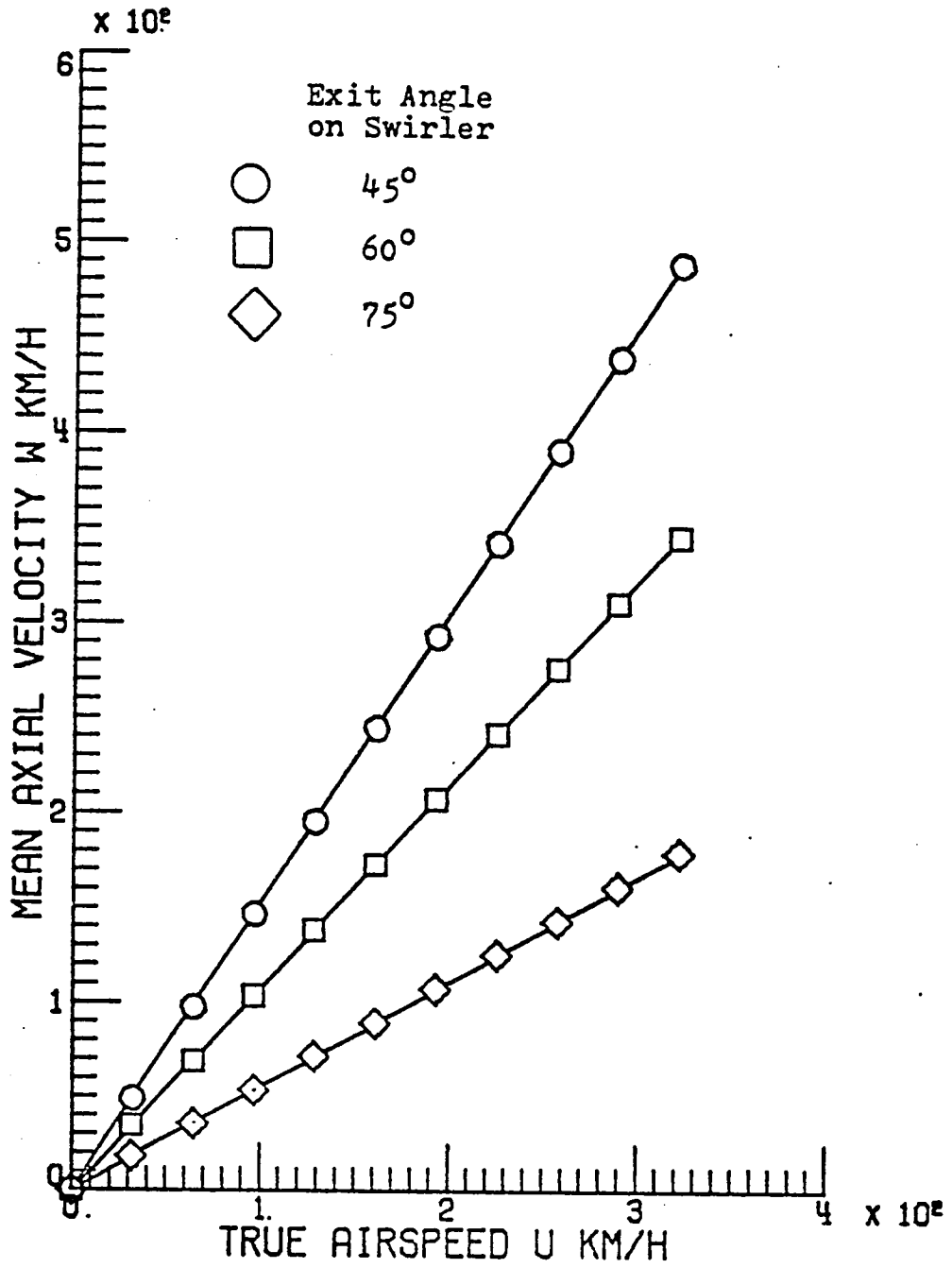
Figure 41. True airspeed versus mean axial velocity for sensor 2 with swirlers having four flutes and various exit angles.
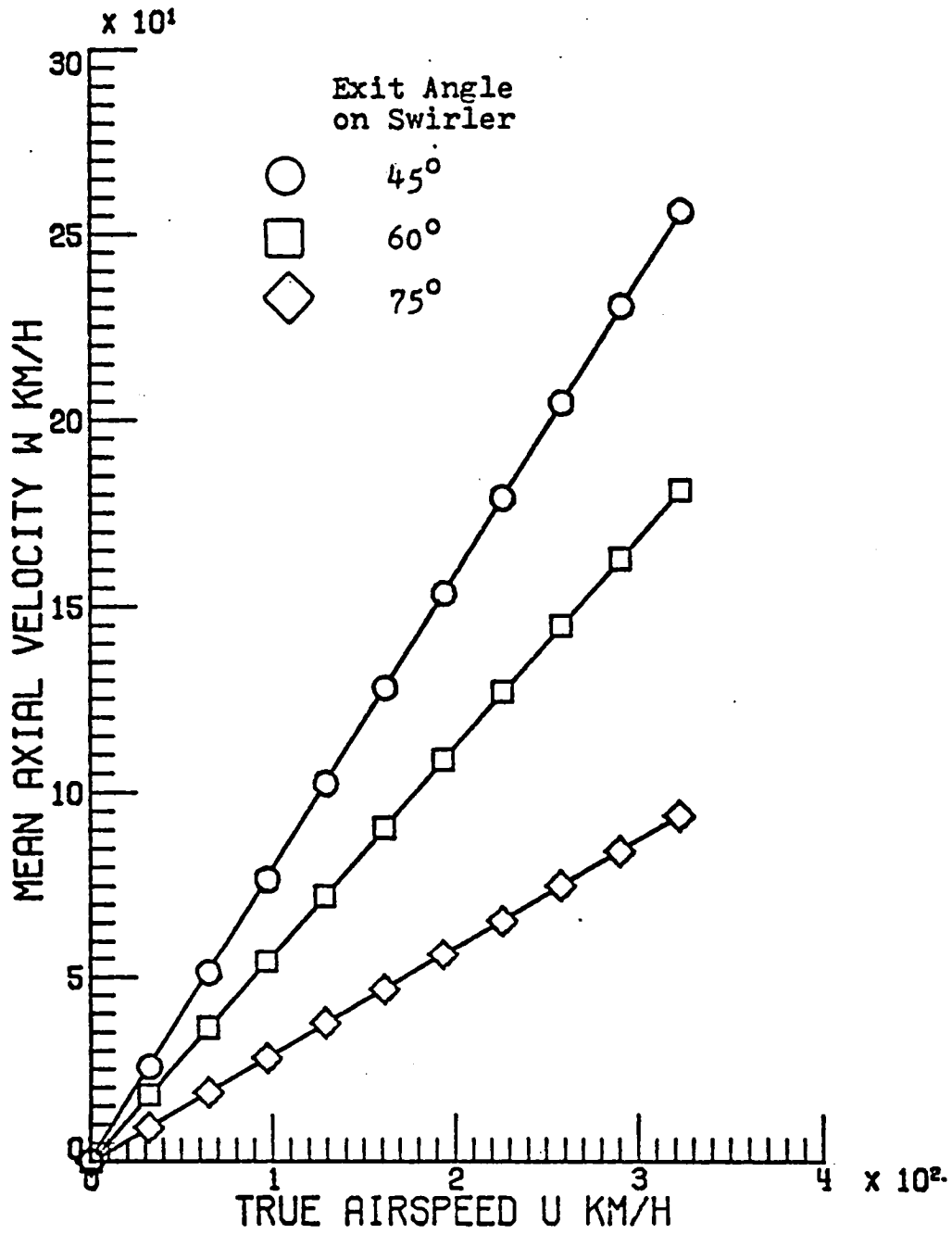
Figure 42. True airspeed versus mean axial velocity for sensor 3 with swirlers having four flutes and various exit angles.
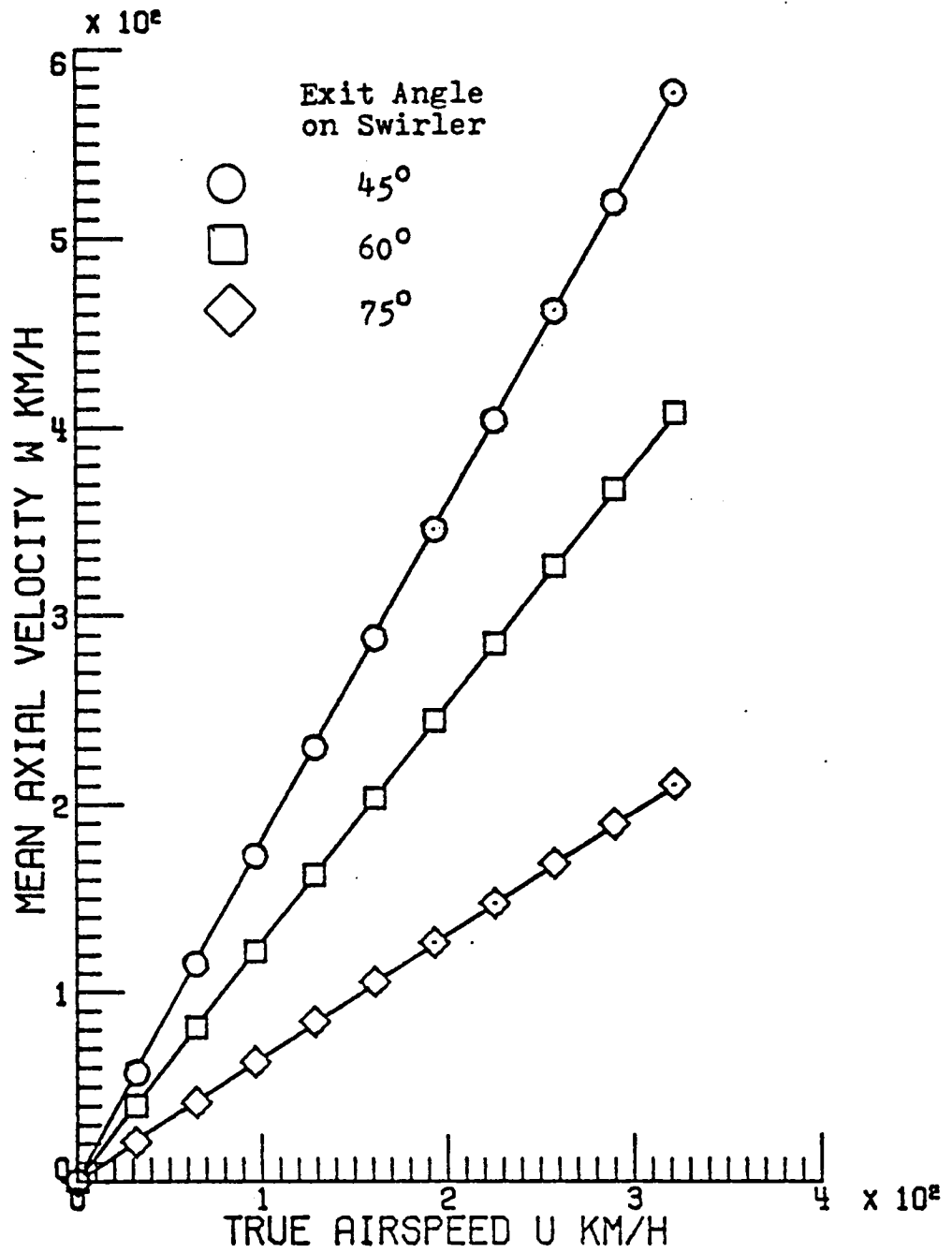
Figure 43.   True airspeed versus mean axial velocity for sensor 4 with swirlers having four flutes and various exit angles.
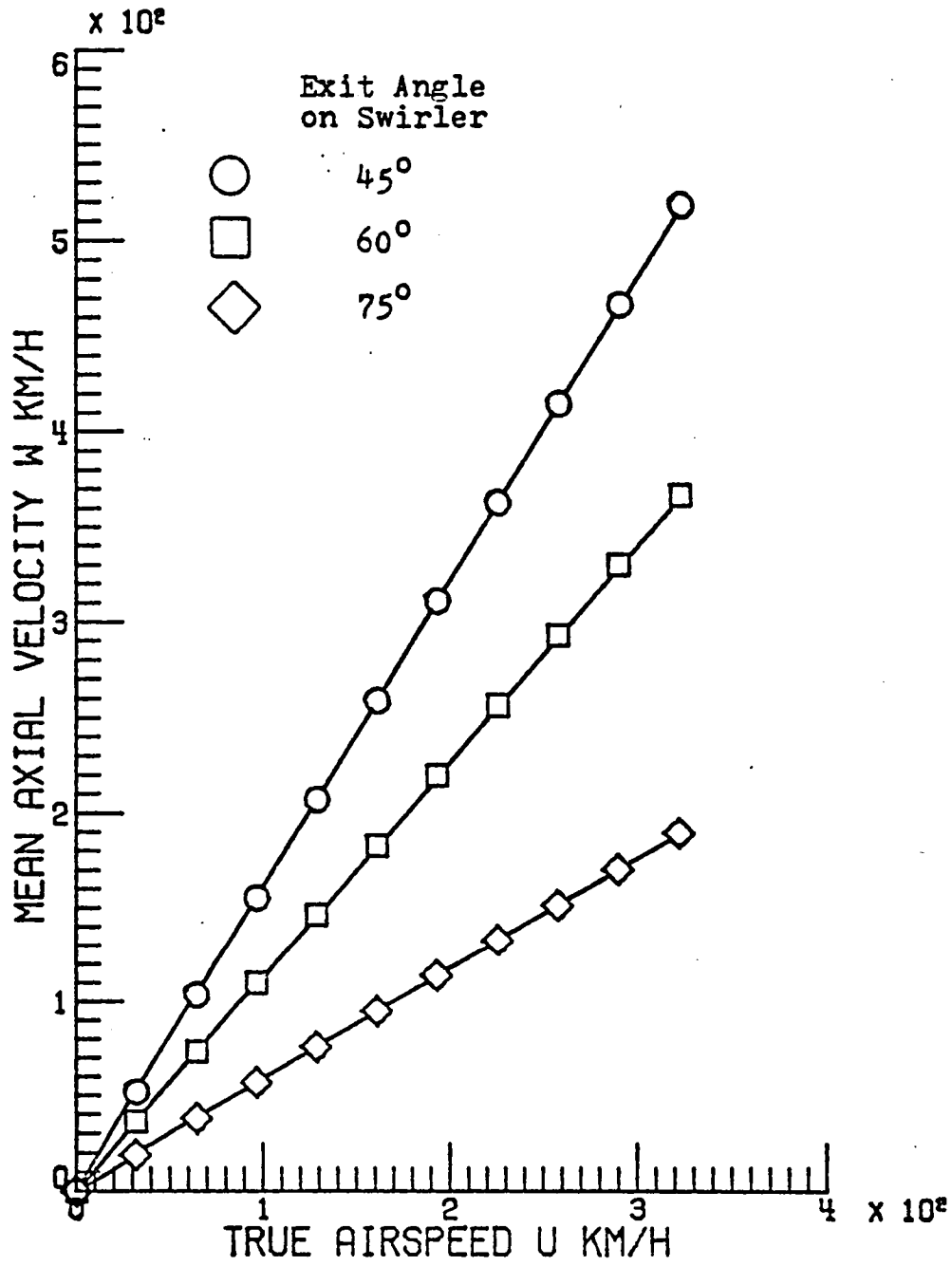
Figure 44. True airspeed versus mean axial velocity for sensor 5 with swirlers having four flutes and various exit angles.
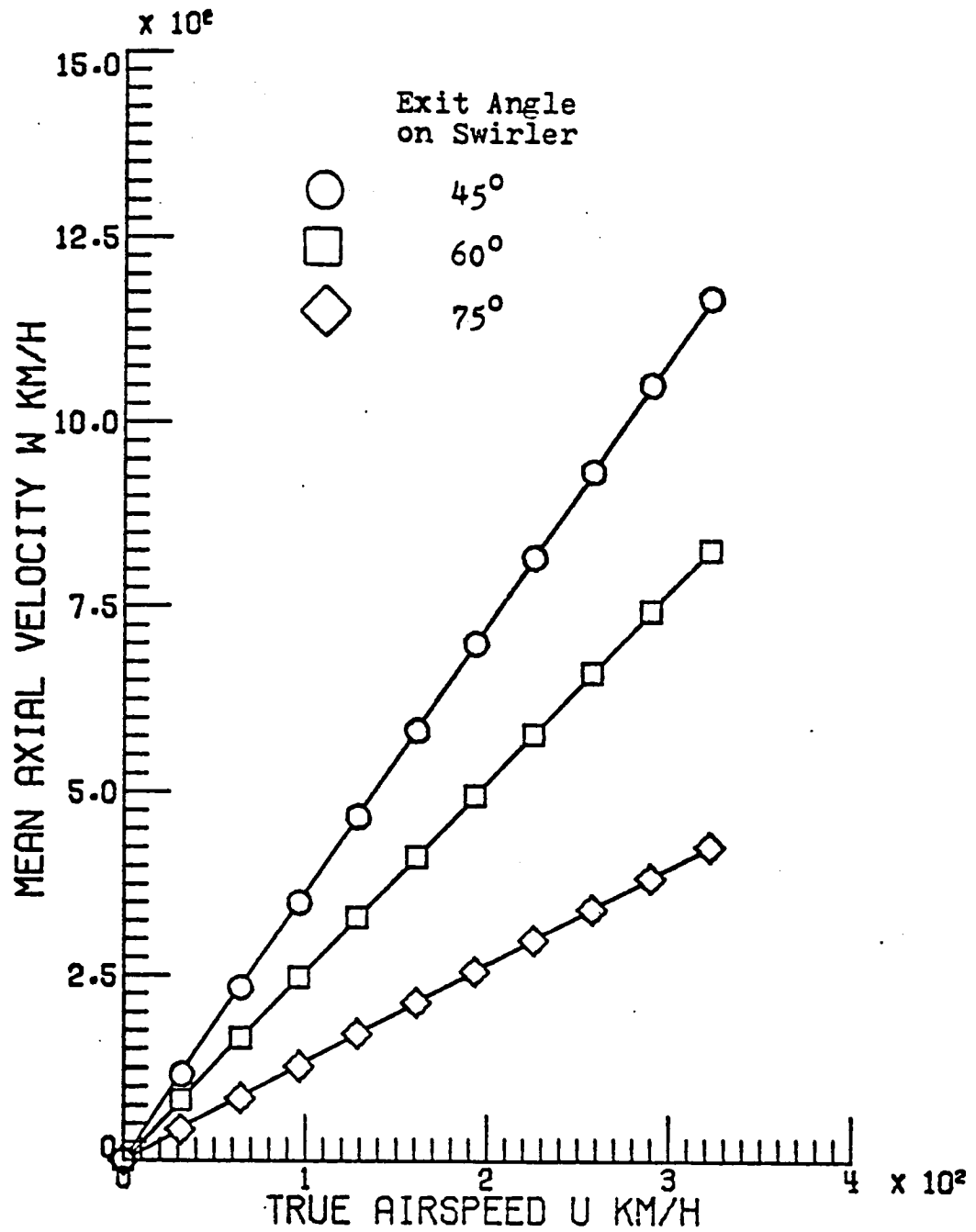
Figure 45.   True airspeed versus mean axial velocity for sensor 6 with
swirlers having four flutes and various exit angles.
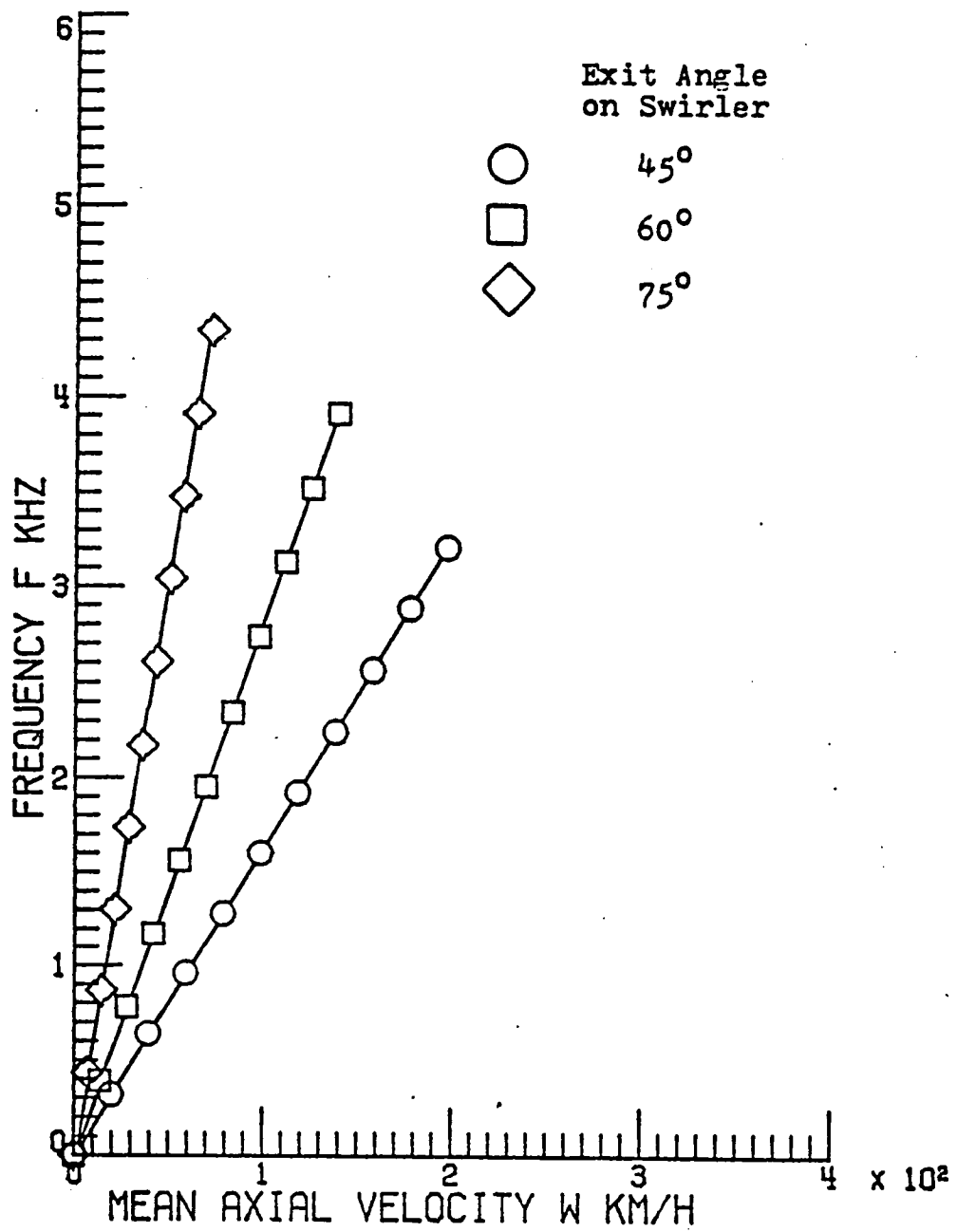
Figure 46.   Relationship between mean axial velocity and frequency
             response for sensor 1 with swirlers having four flutes
             and various exit angles.
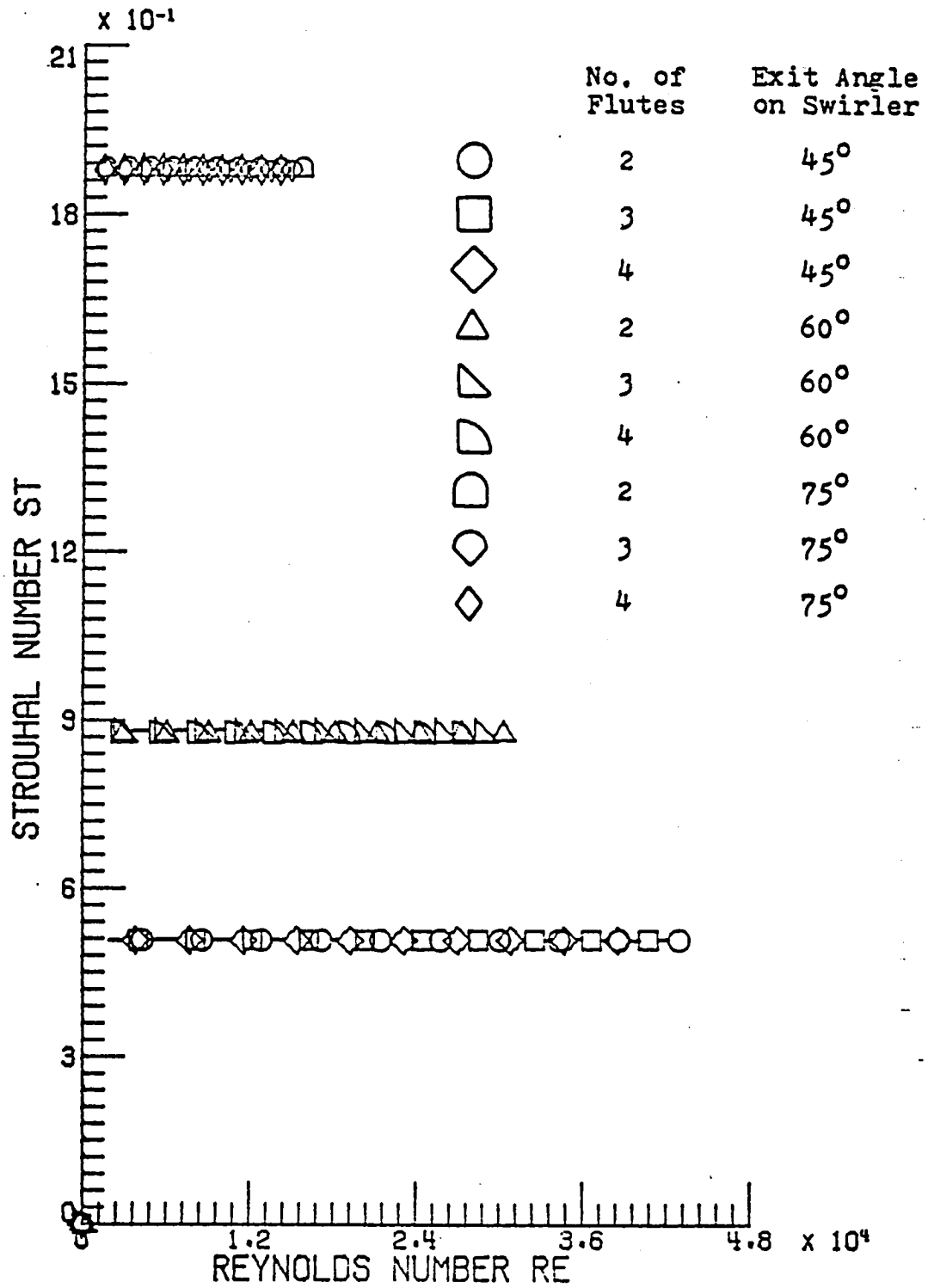
Figure 47. Reynolds number versus Strouhal number for sensor 1.
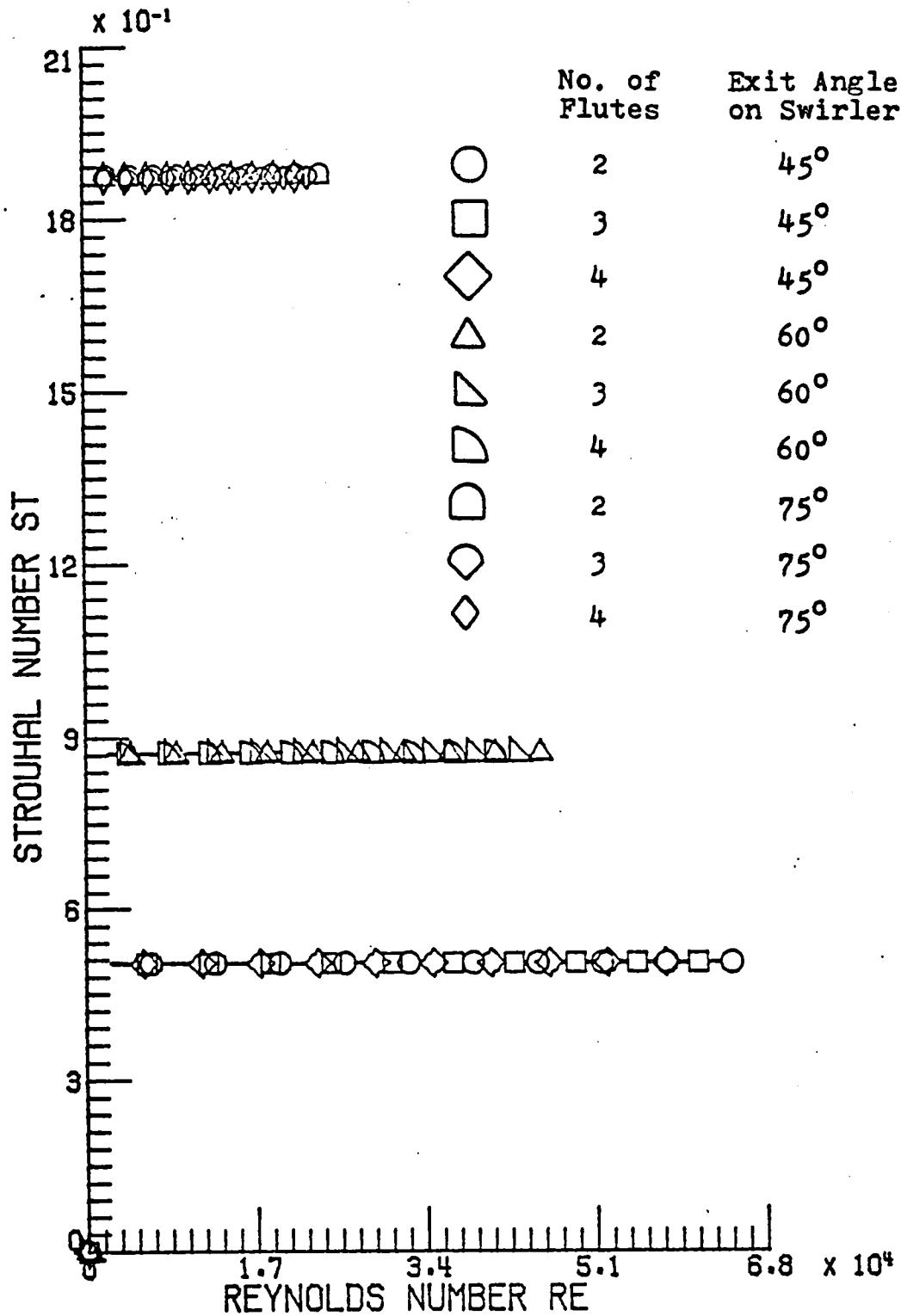
Figure 48. Reynolds number versus Strouhal number for sensor 2.
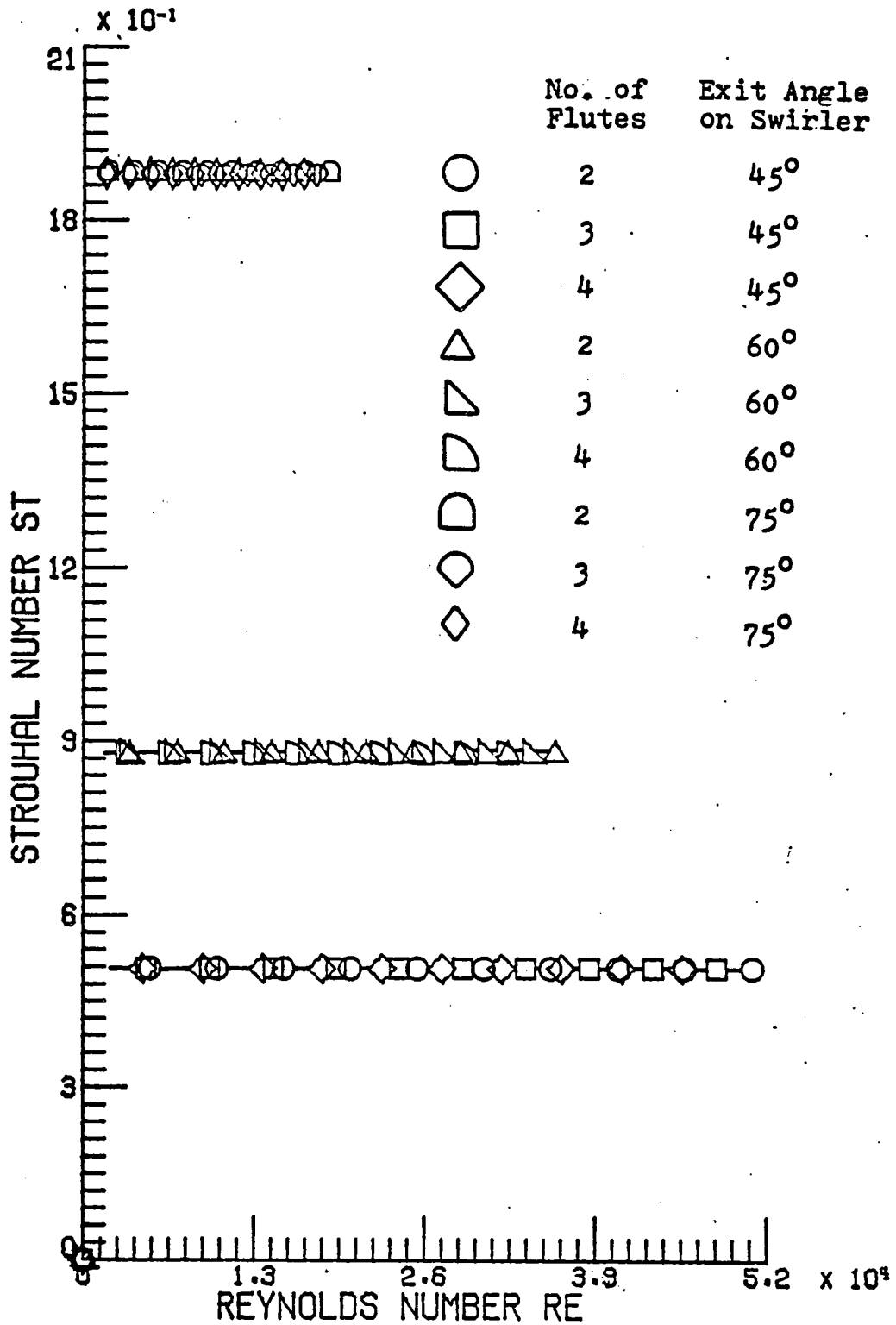
Figure 49. Reynolds number versus Strouhal number for sensor 3.
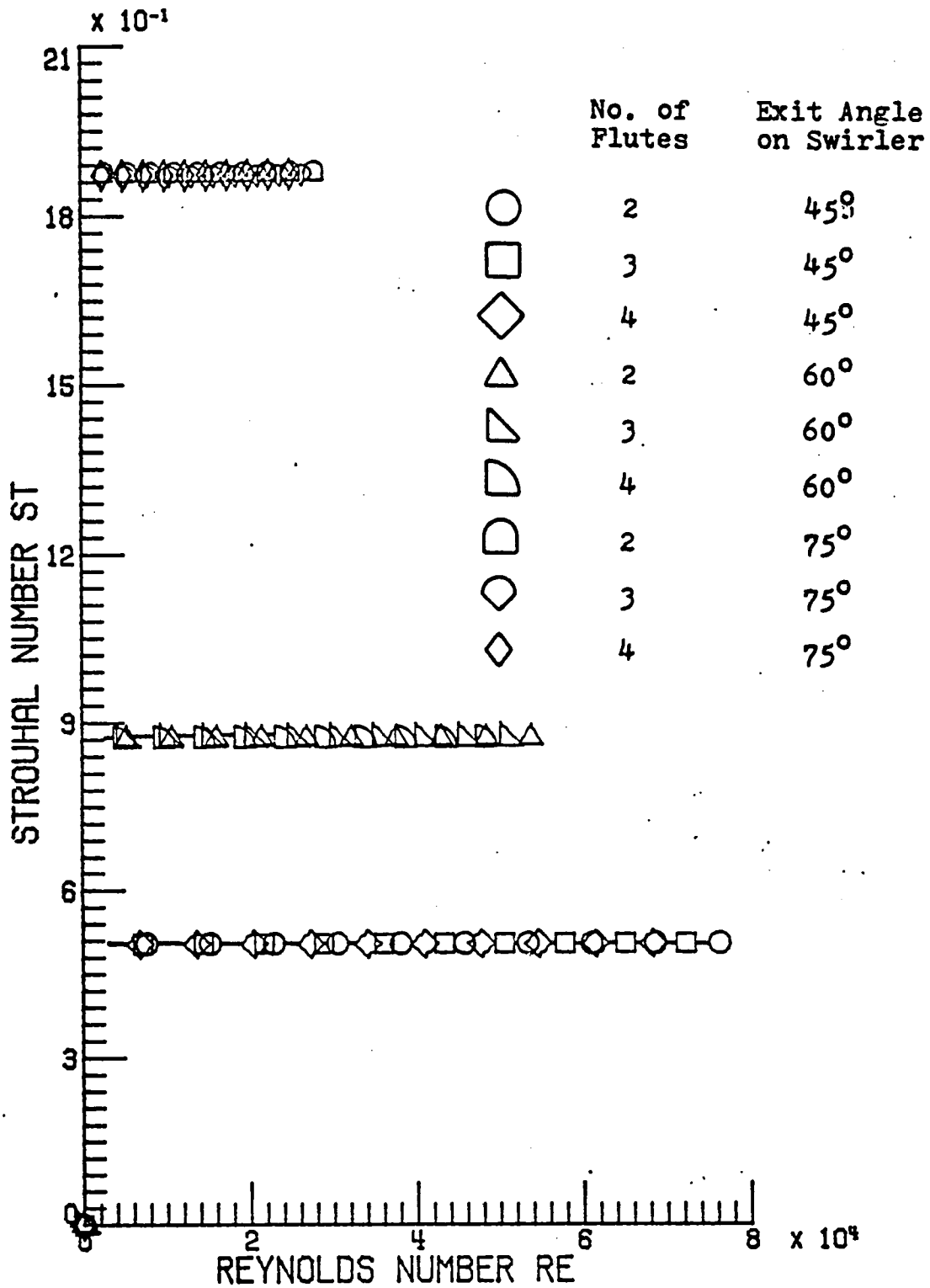
Figure 50.   Reynolds number versus Strouhal number for sensor 4.
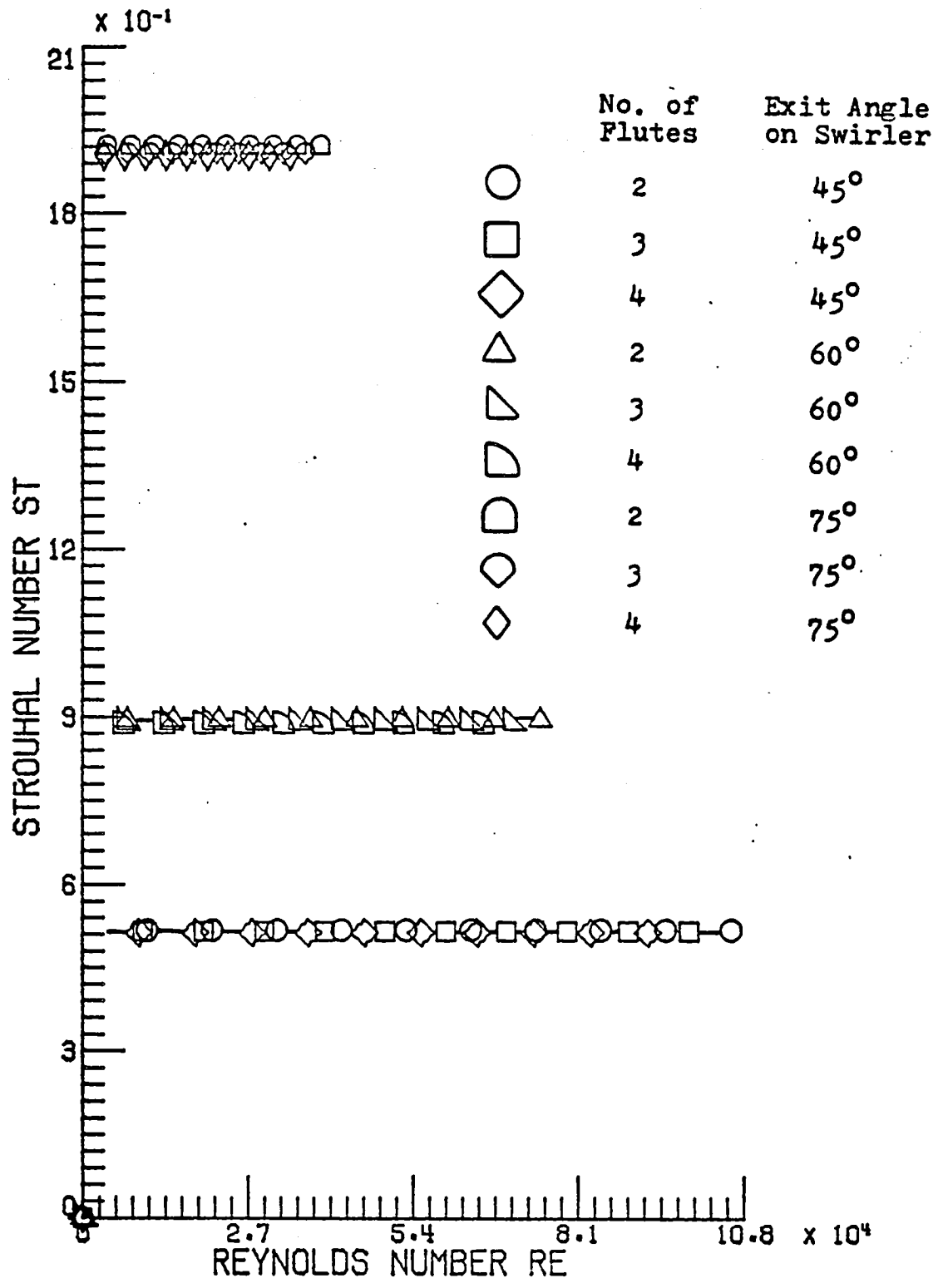
Figure 51. Reynolds number versus Strouhal number for sensor 5.
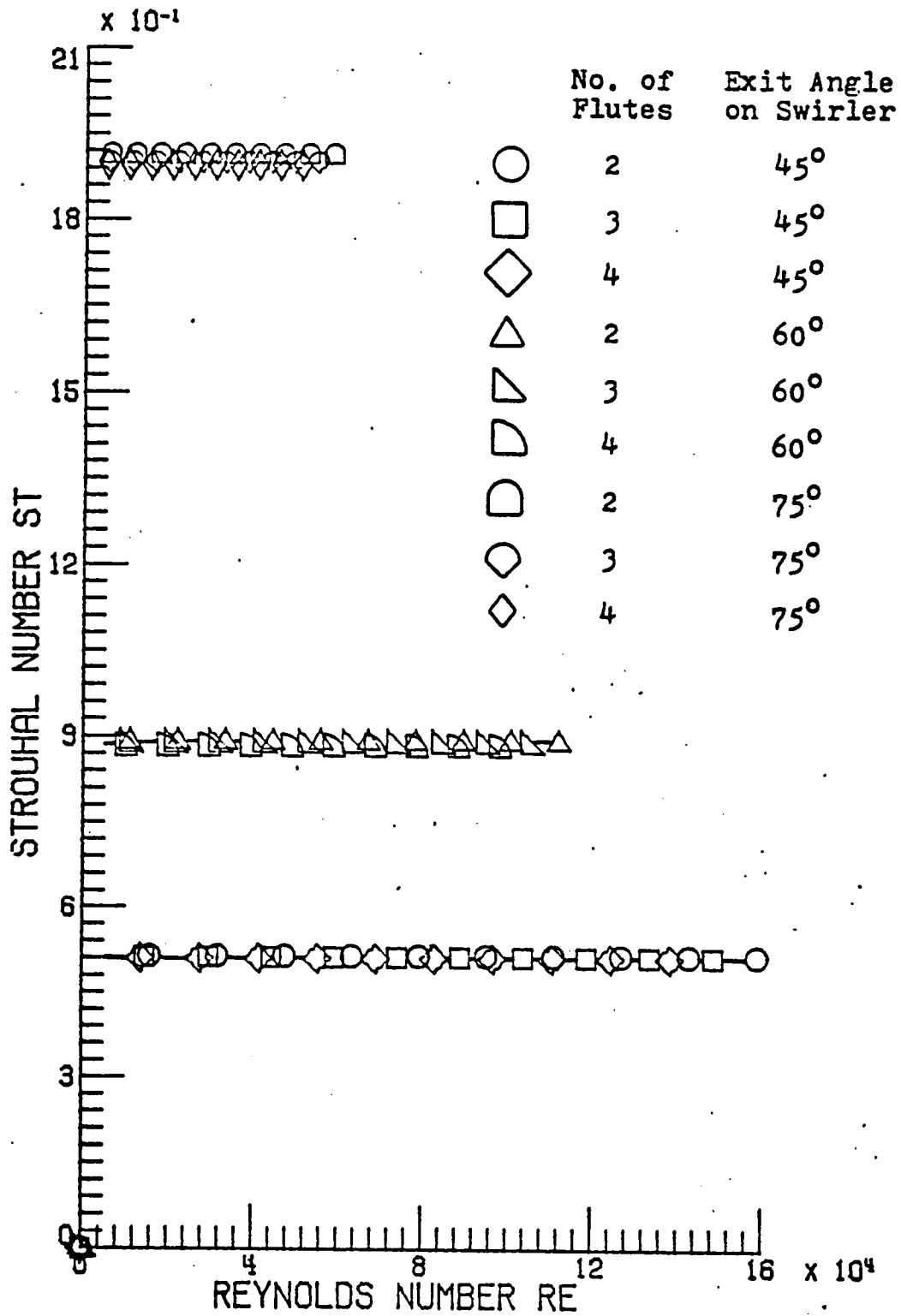
Figure 52. Reynolds number versus Strouhal number for sensor 6.
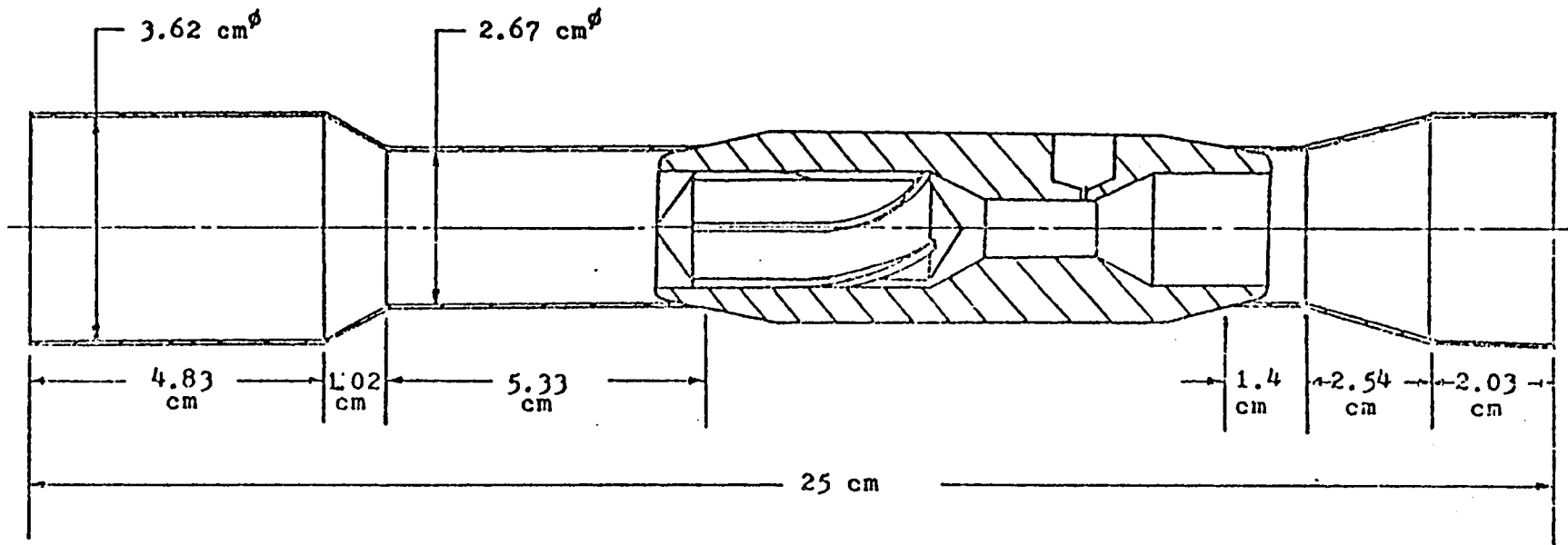
Fiugre 53. Vortex tube for flow visualization.

Valve

Eight tubes

Water supply

Air bubbles injected here

Vortex tube

Container

Drain
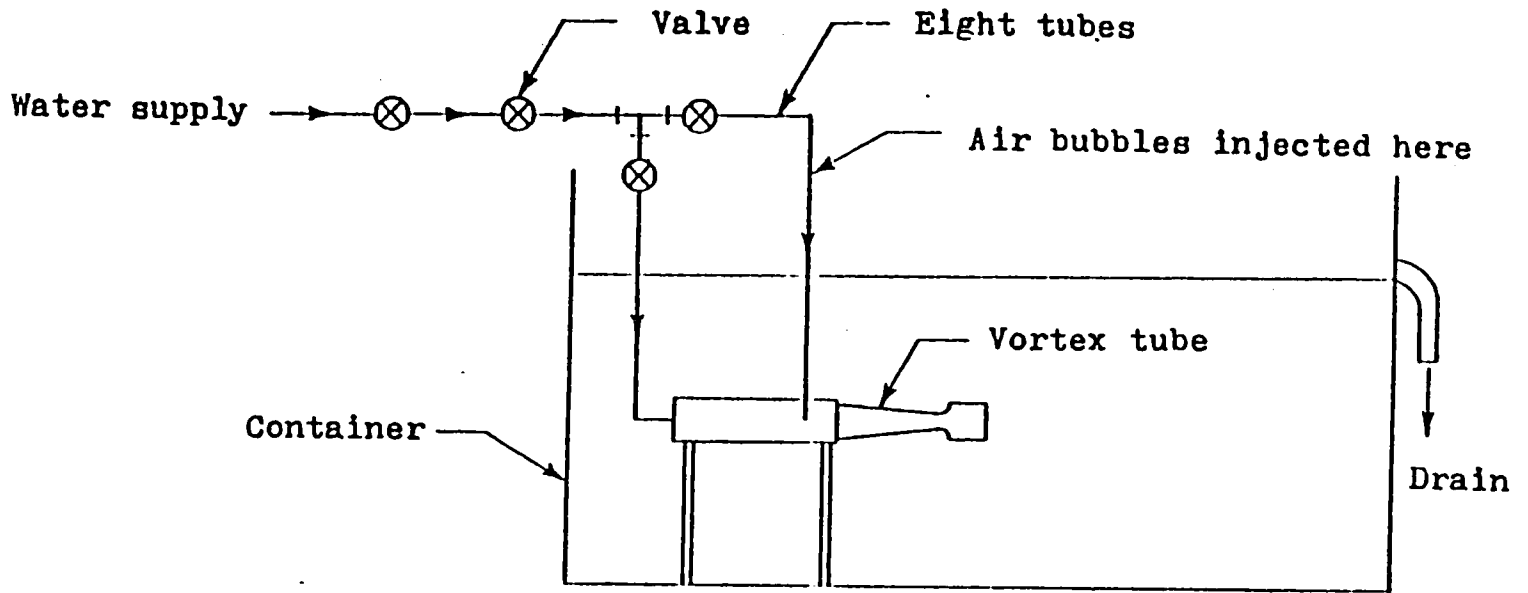
Figure 54. Water model setup.
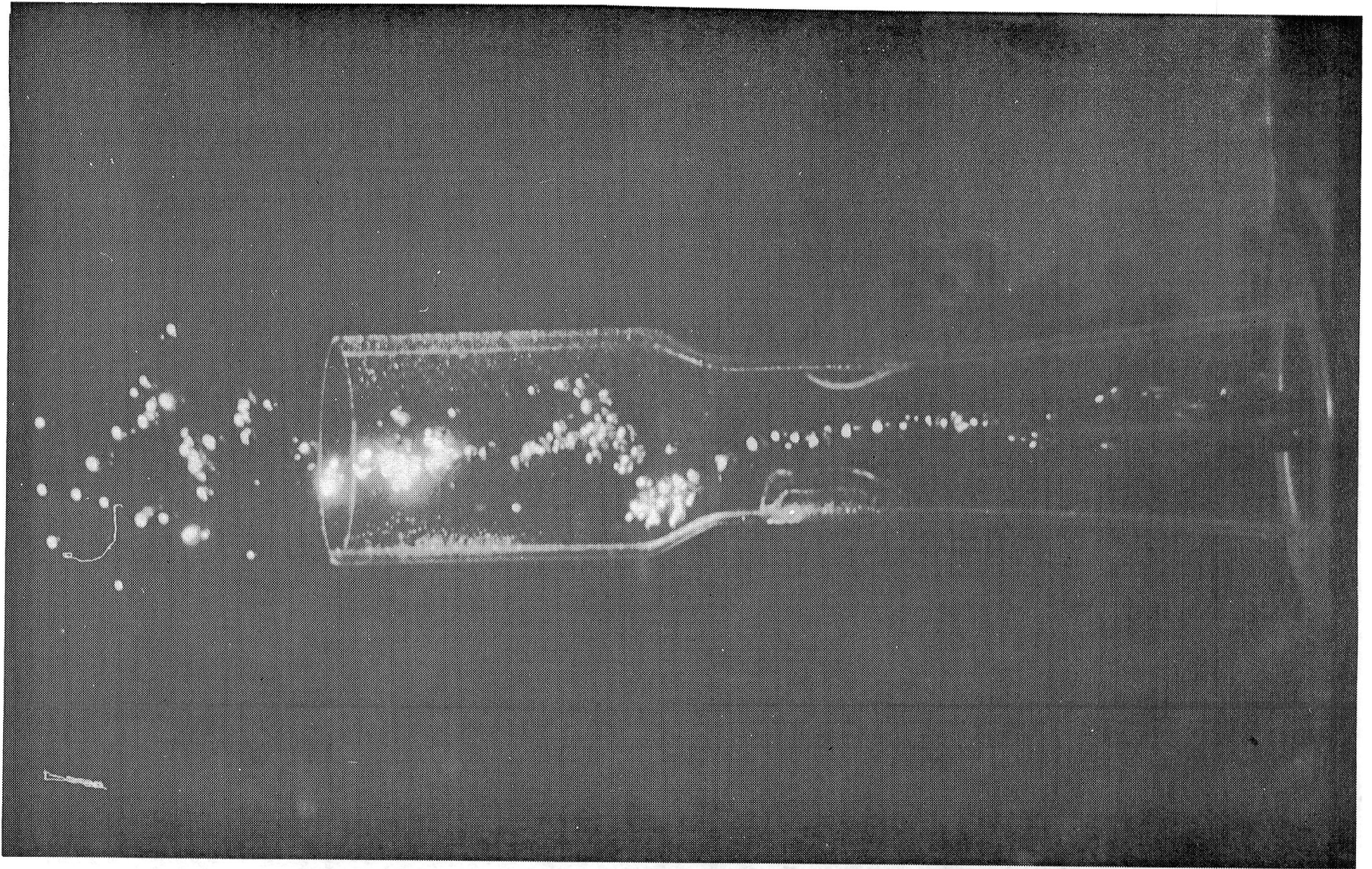
Figure 55. Fluid flow phenomenon-precession.
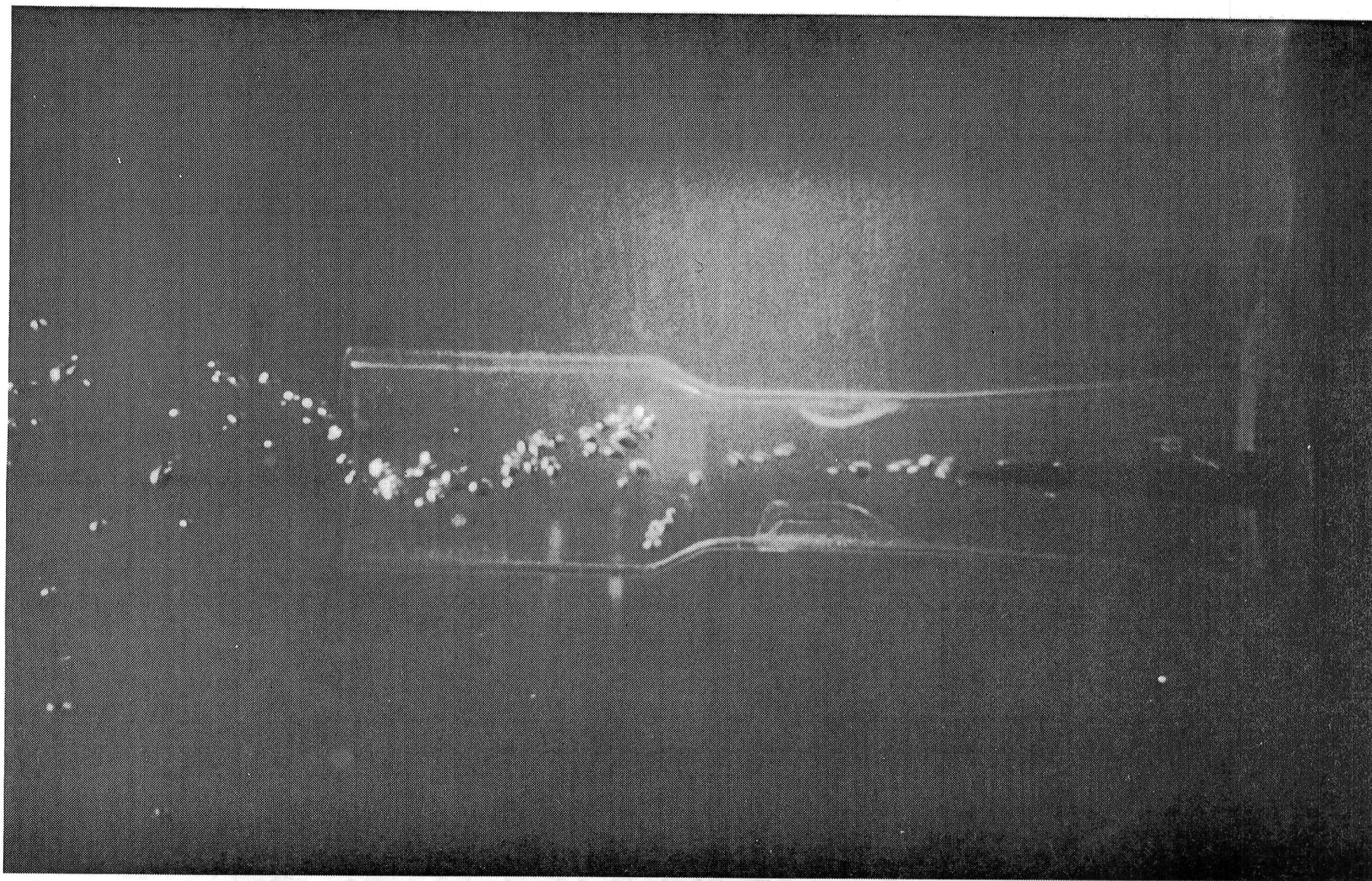
Figure 56. Fluid flow phenomenon-precession.
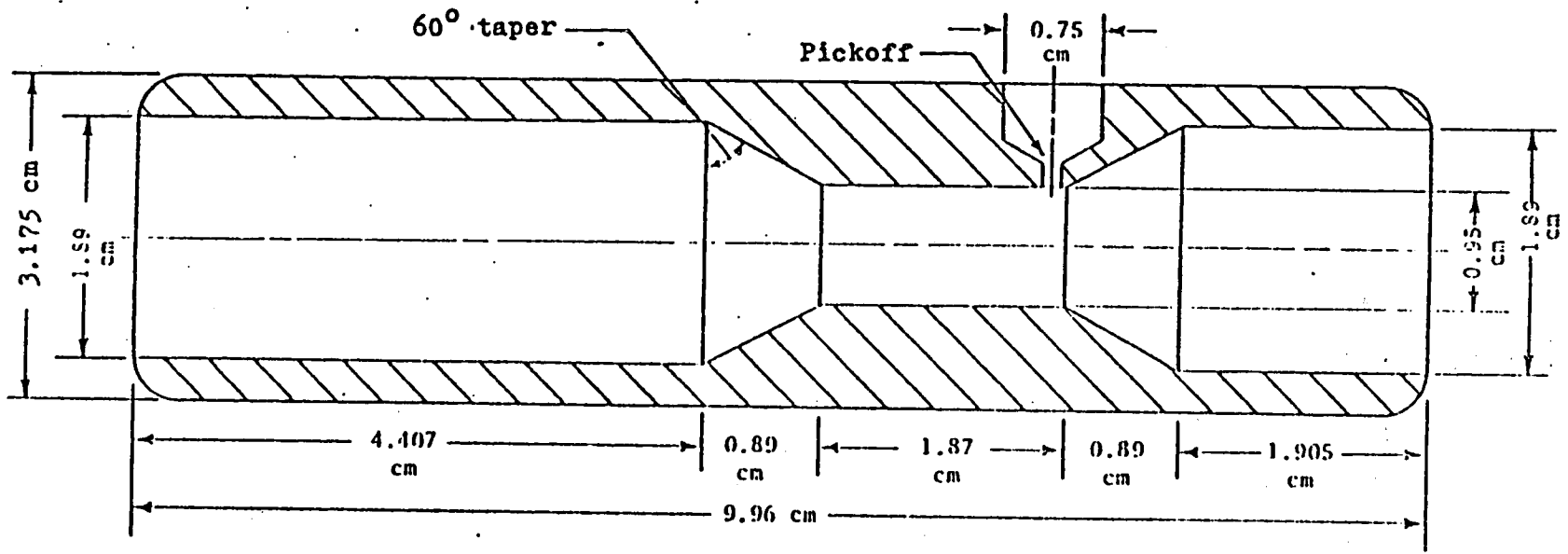
Figure 57. Dimensions of the vortex tube.
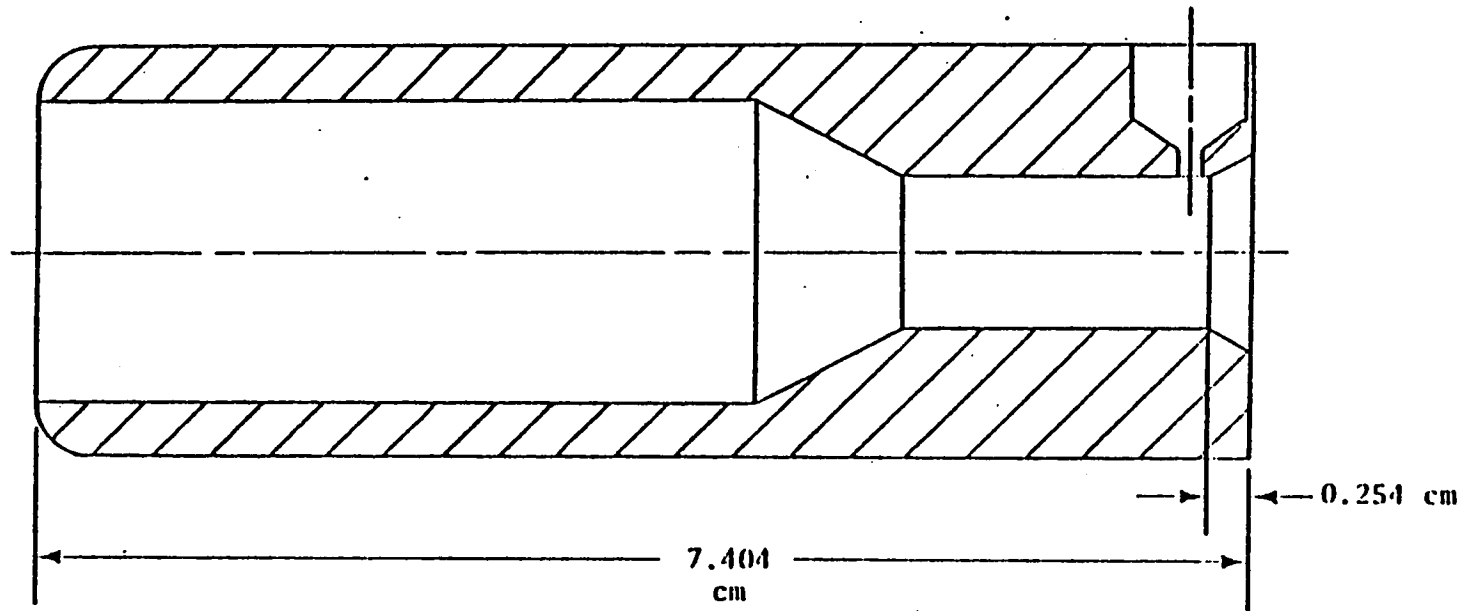
Figure 58.   Dimensions of the vortex tube with abrupt enlargement in the rear.
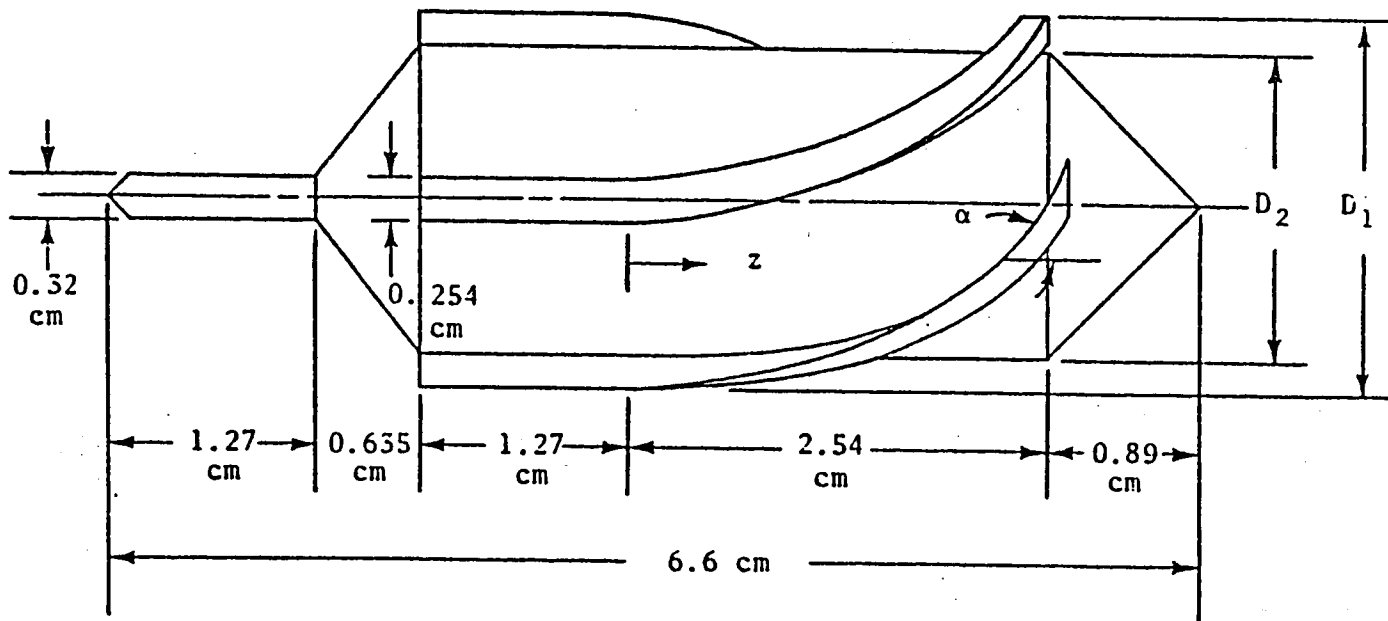
$$\text{For } \alpha = 45^{\circ}, \quad \theta = 76.9 \, z^2 \text{ degree}$$

$$\text{For } \alpha = 60^{\circ}, \quad \theta = 133.2 \, z^2 \text{ degree}$$

$$\text{For } \alpha = 75^{\circ}, \quad \theta = 191.4 \, z^2 \text{ degree}$$

Figure 59.   Design and dimensions of the swirler.
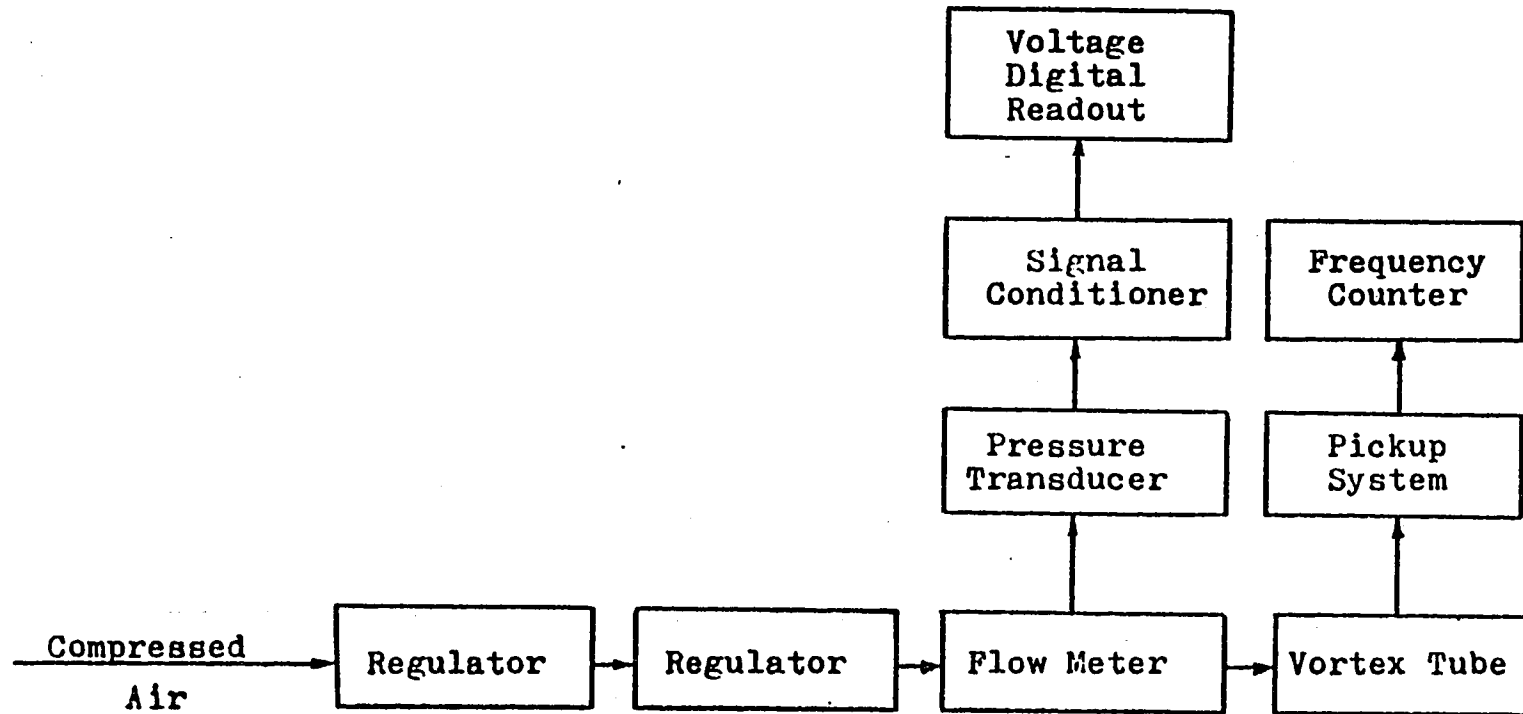
Figure 60. Esperimental test setup.
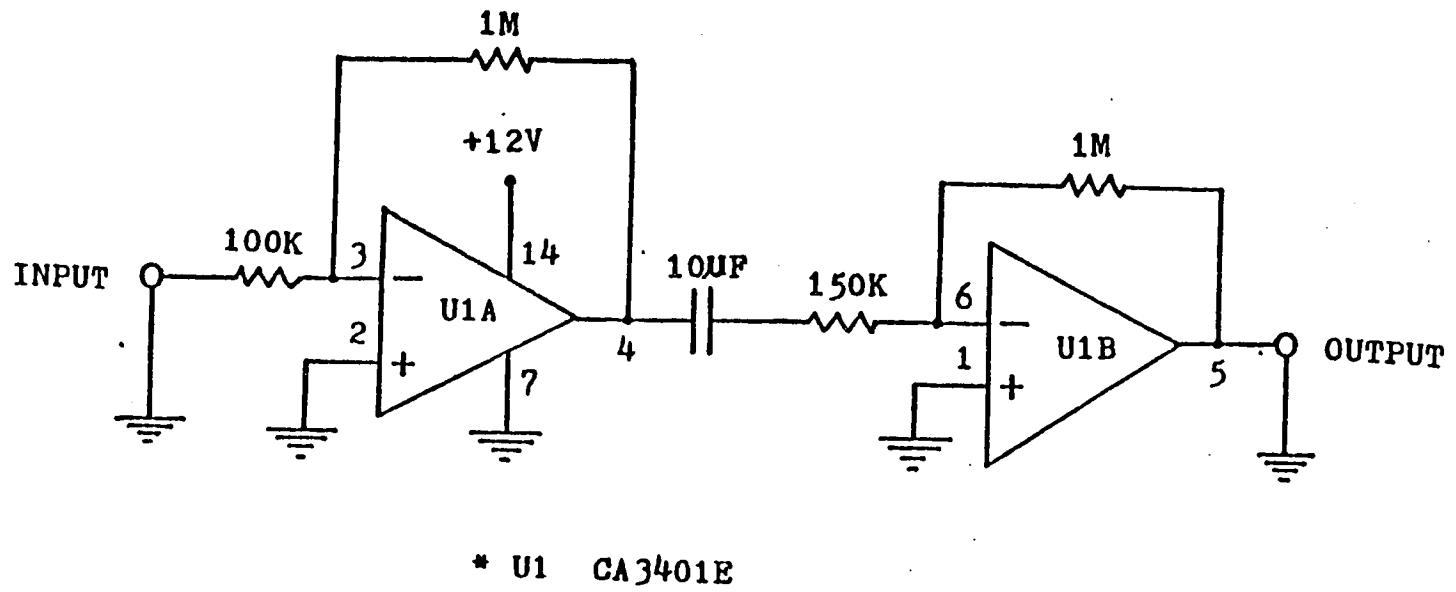
Figure 61.   Schematic diagram of input amplifier.

OUTER DIMENSIONS
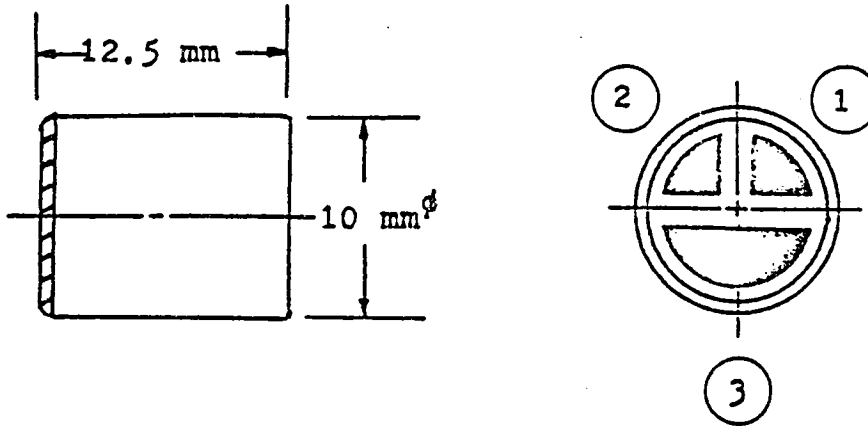
CIRCUIT DIAGRAM
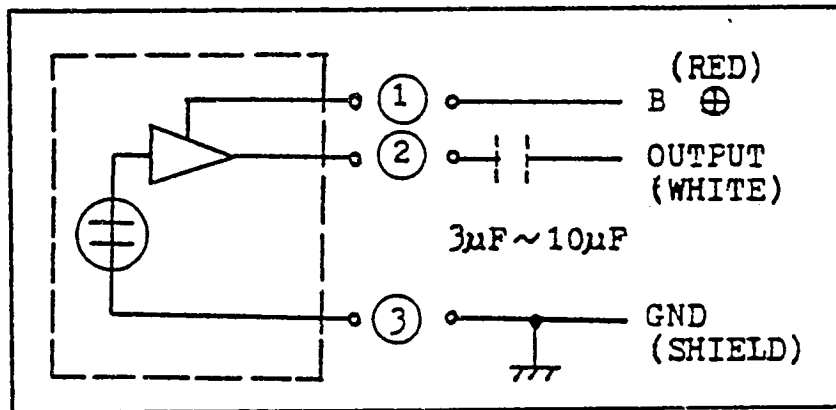
ELECTRICAL CHARACTERISTICS

Sensitivity: -65dB ± 4dB (0dB REF 1V/μbar at 1 KHz)

Output Impedance: 600 Ohms

Omni-directional Response

Supply Voltage: 2.0 V Min., 10 V Max.

Nominal Supply: 4.5 V

Current Drain: 0.5 mA Max.

Figure 62.   Description of electric condenser microphone made by
Radio Shack.
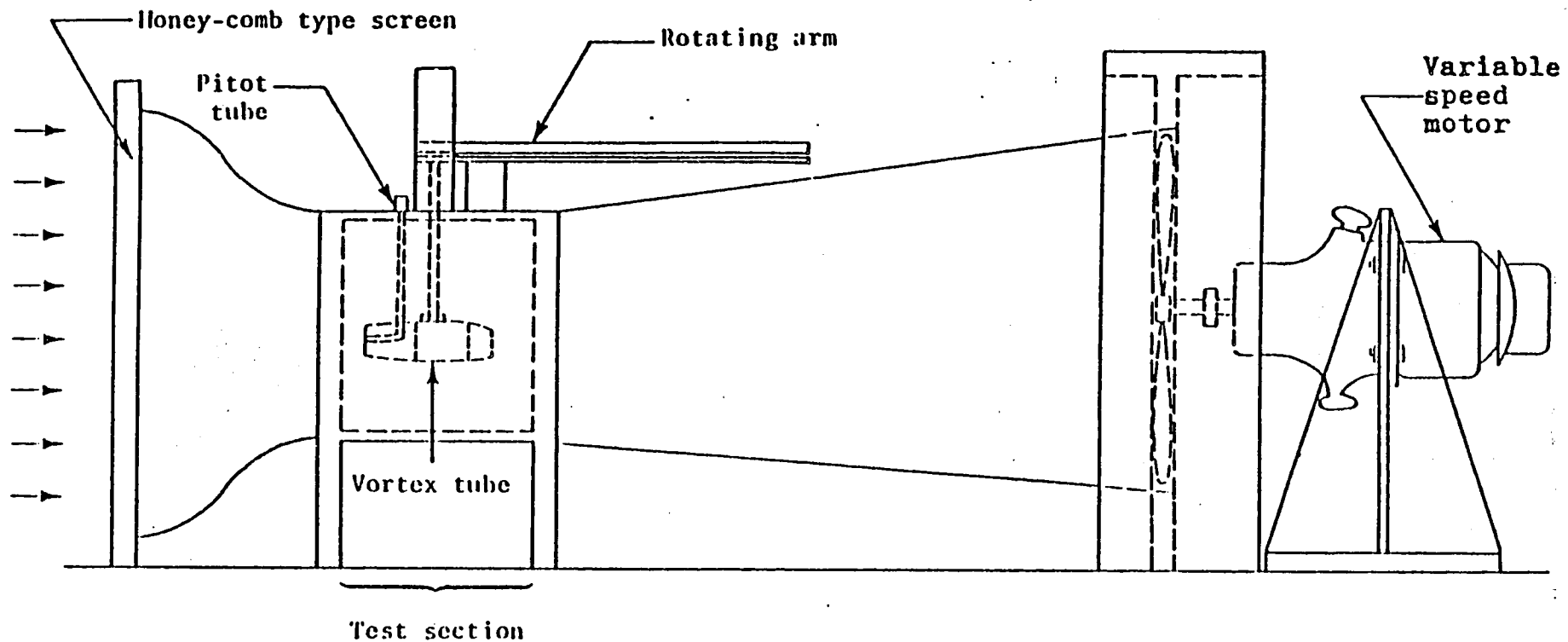
Figure 63. Wind tunnel (15.24 cm by 15.24 cm).
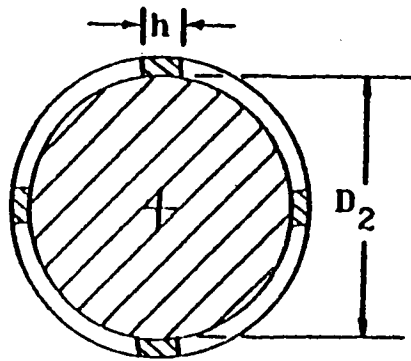
Swirler Type / D₂ Diameter	4 Flutes 45°	4 Flutes 60°	4 Flutes 75°
1.5875 cm (0.625 in.)	0.3429 cm (0.135 in.)	0.5080 cm (0.200 in.)	0.6096 cm (0.240 in.)
1.5240 cm (0.600 in.)	0.3429 cm (0.135 in.)	0.5080 cm (0.200 in.)	0.6096 cm (0.240 in.)

Figure 64.   Actual flute width h on swirler used in the experimental test.

Areas Type of Swirlers		Designed Area A_d cm^2	Actual Area A_a cm^2	Ratio of A_a/A_d
D_2=1.5875 cm	45°	0.7096	0.6532	0.9205
	60°	0.7096	0.5483	0.7727
	75°	0.7096	0.4838	0.6818
D_2=1.5240 cm	45°	0.8325	0.7648	0.9186
	60°	0.8325	0.6390	0.7675
	75°	0.8325	0.5616	0.6745

Figure 65. Comparison of designed and actual areas of different
swirlers with four flutes.

0.127 cm (0.05 in)

D_3 D_1

Vortex Tube
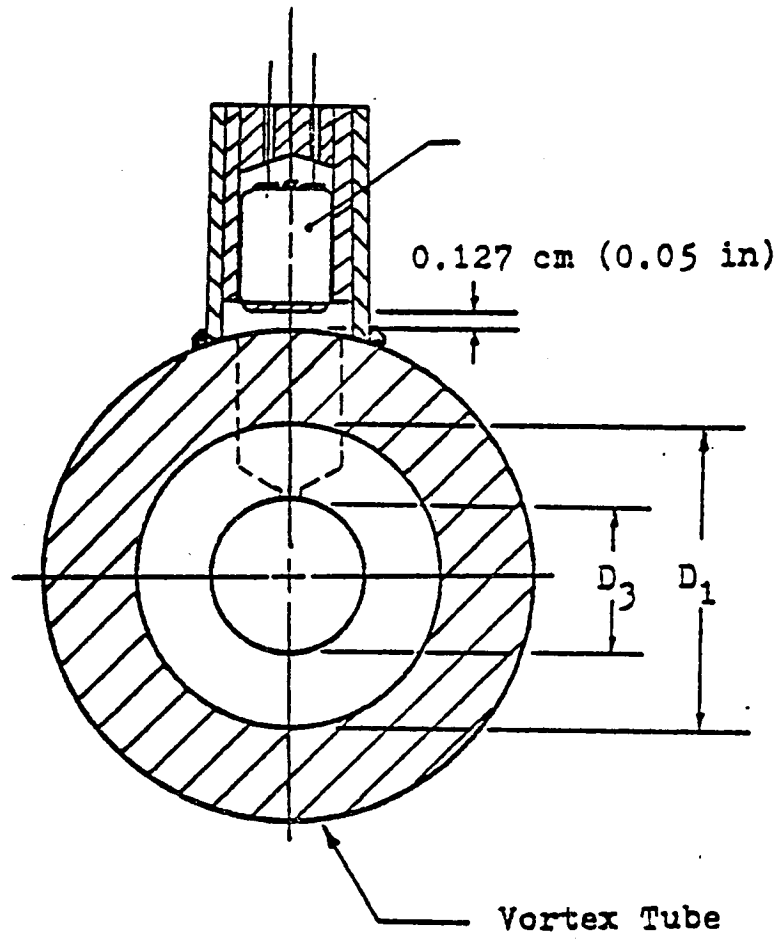
Figure 66. Microphone position used in experimental test.
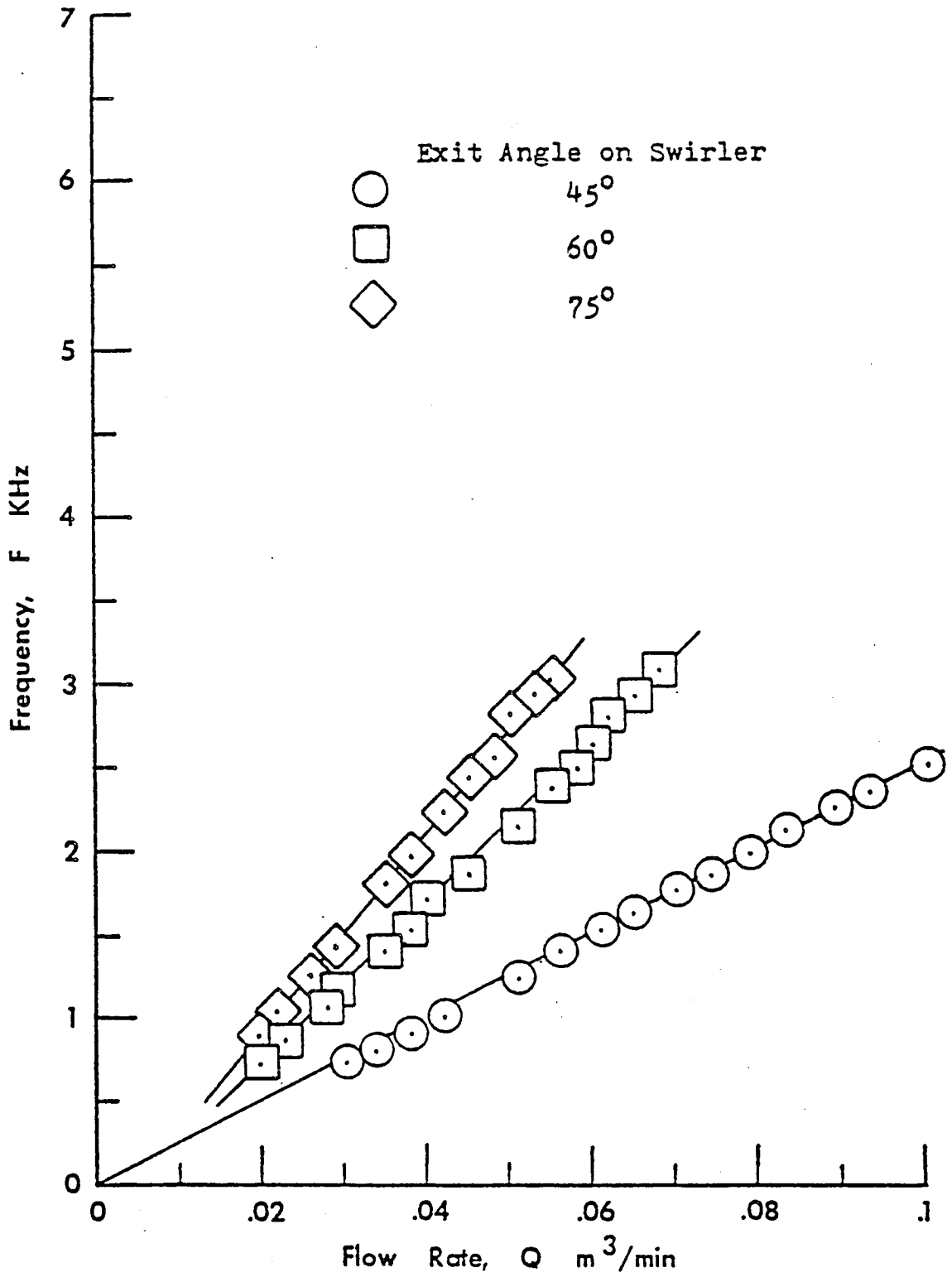
Figure 67. Experimental data for sensor 1 with swirlers having four flutes and various exit angles.
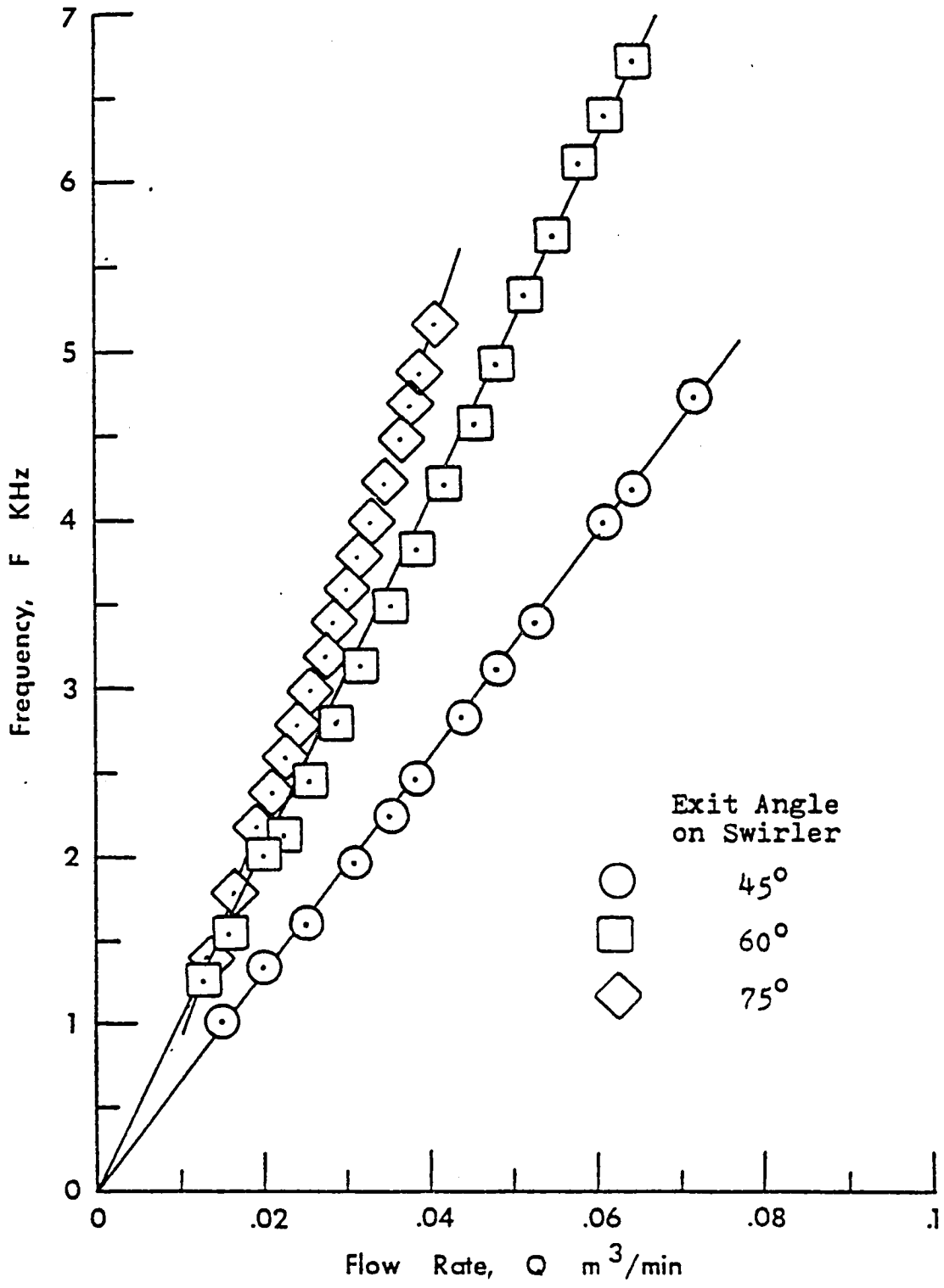
Figure 68. Experimental data for sensor 2 with swirlers having four flutes and various exit angles.

150
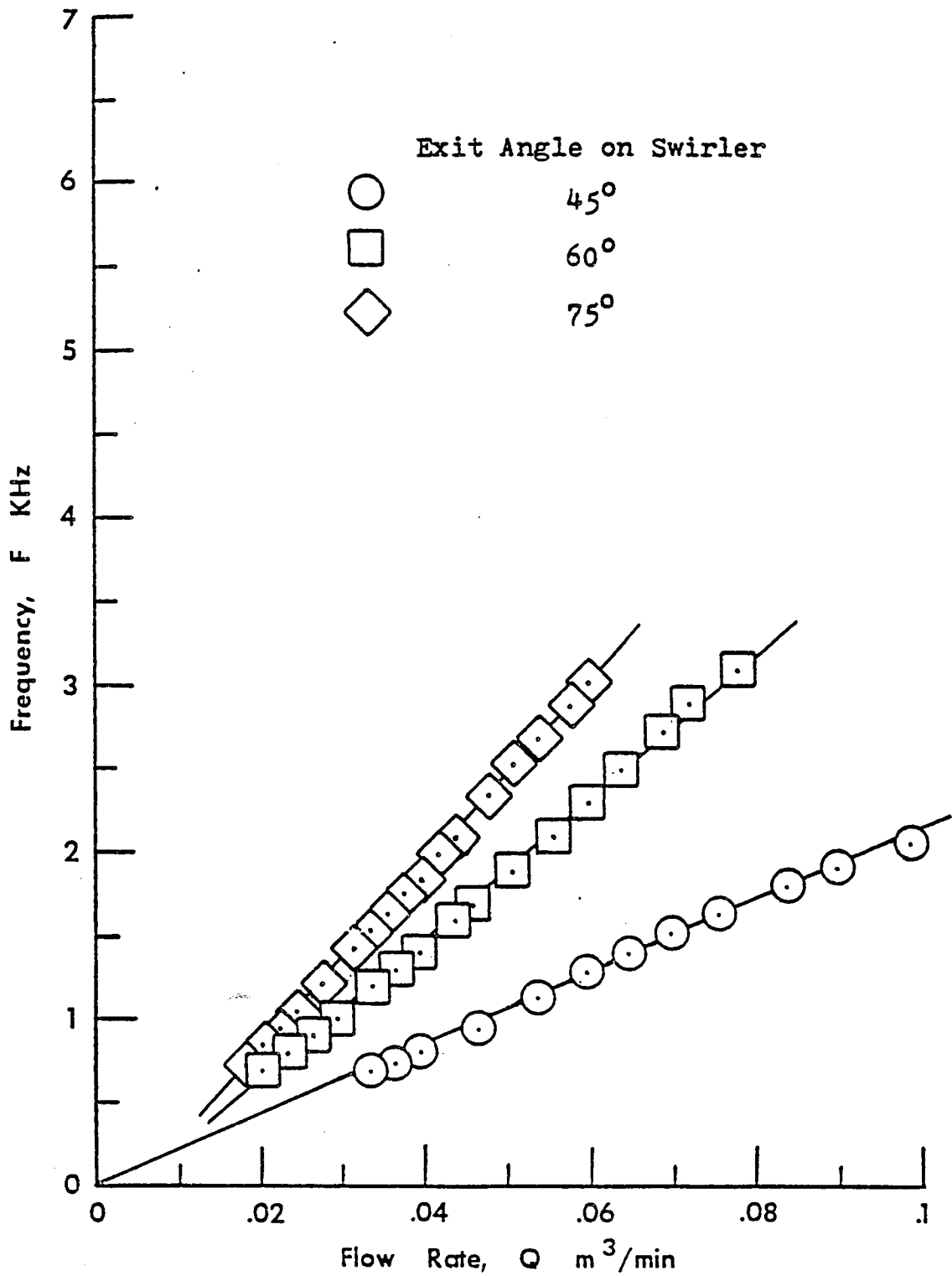
Figure 69. Experimental data for sensor 3 with swirlers having four flutes and various exit angles.

151
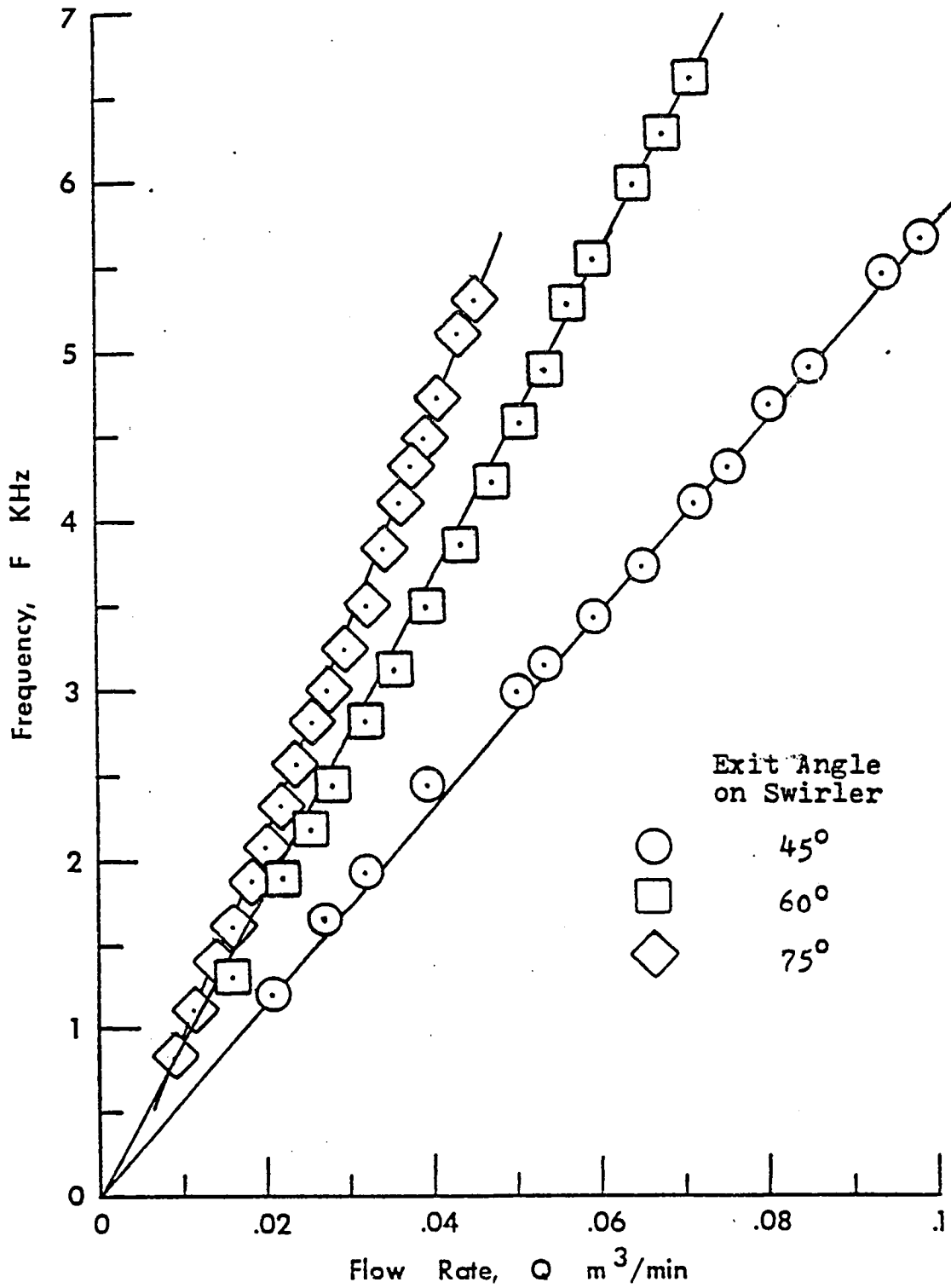
Figure 70. Experimental data for sensor 4 with swirlers having four flutes and various exit angles.
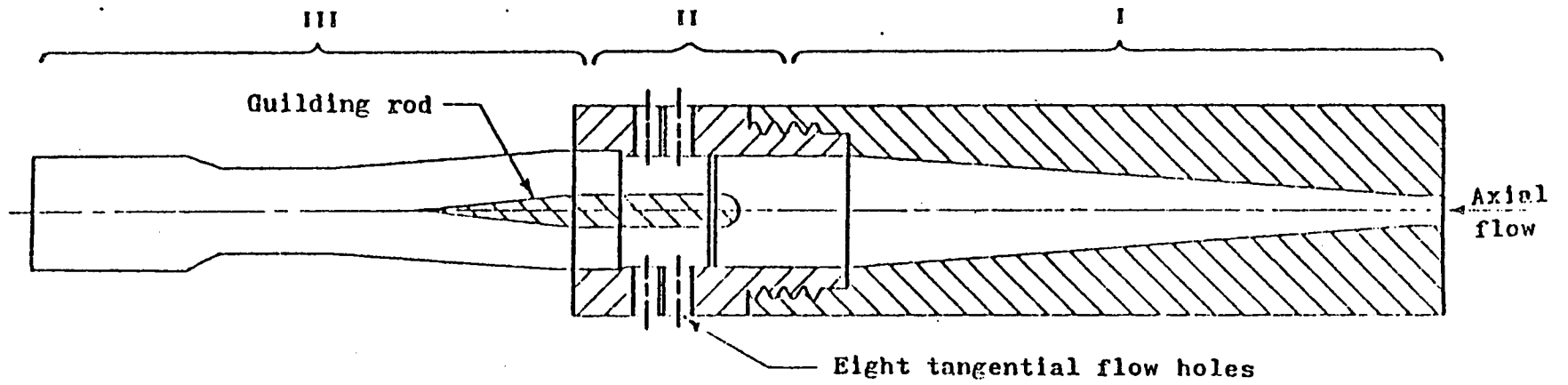
Figure 71. Modified version of vortex tube for wind-tunnel test.
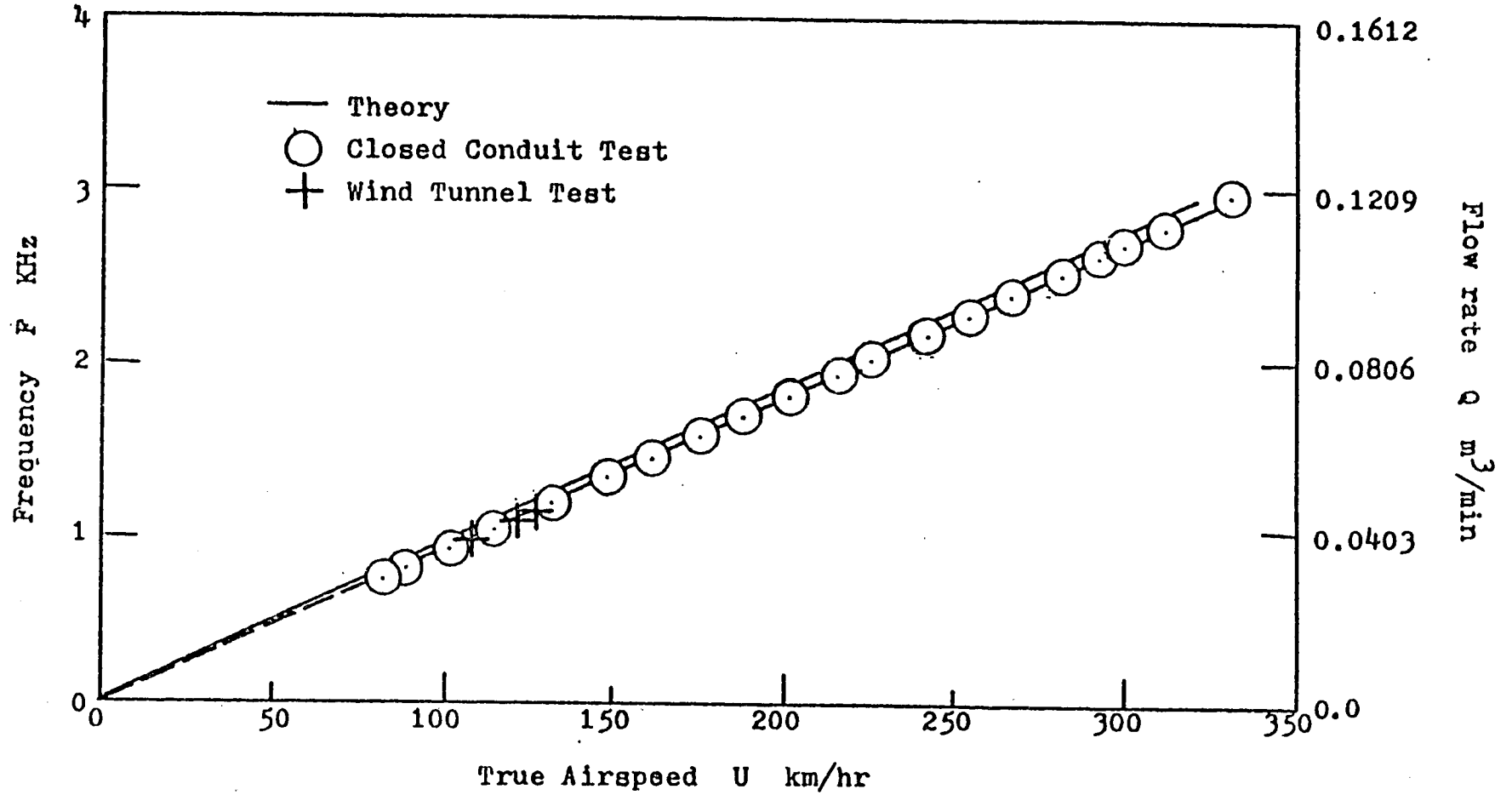
Figure 72. Performance of sensor 1 with swirler having 4 flutes and exit angle 45°.
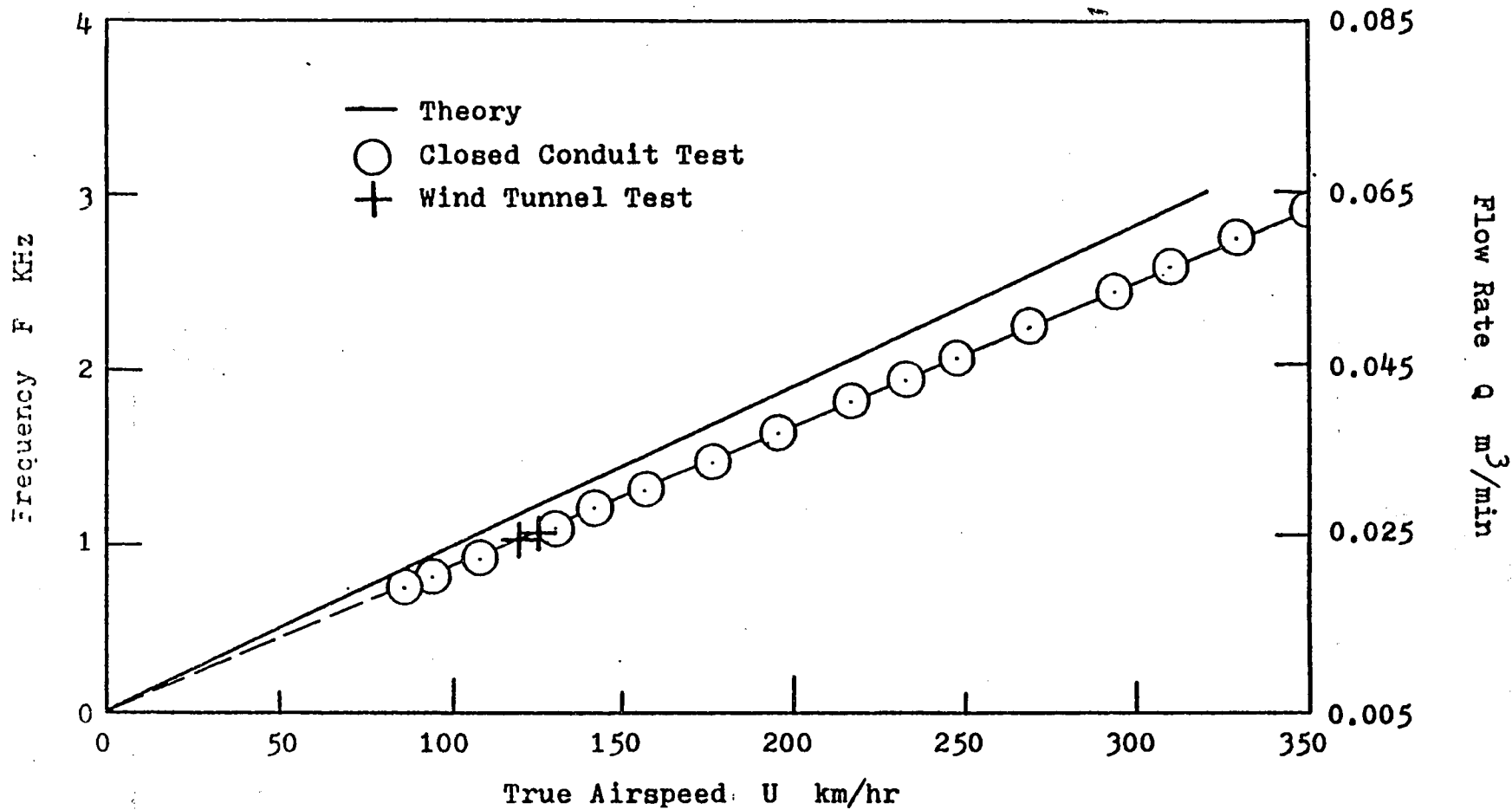
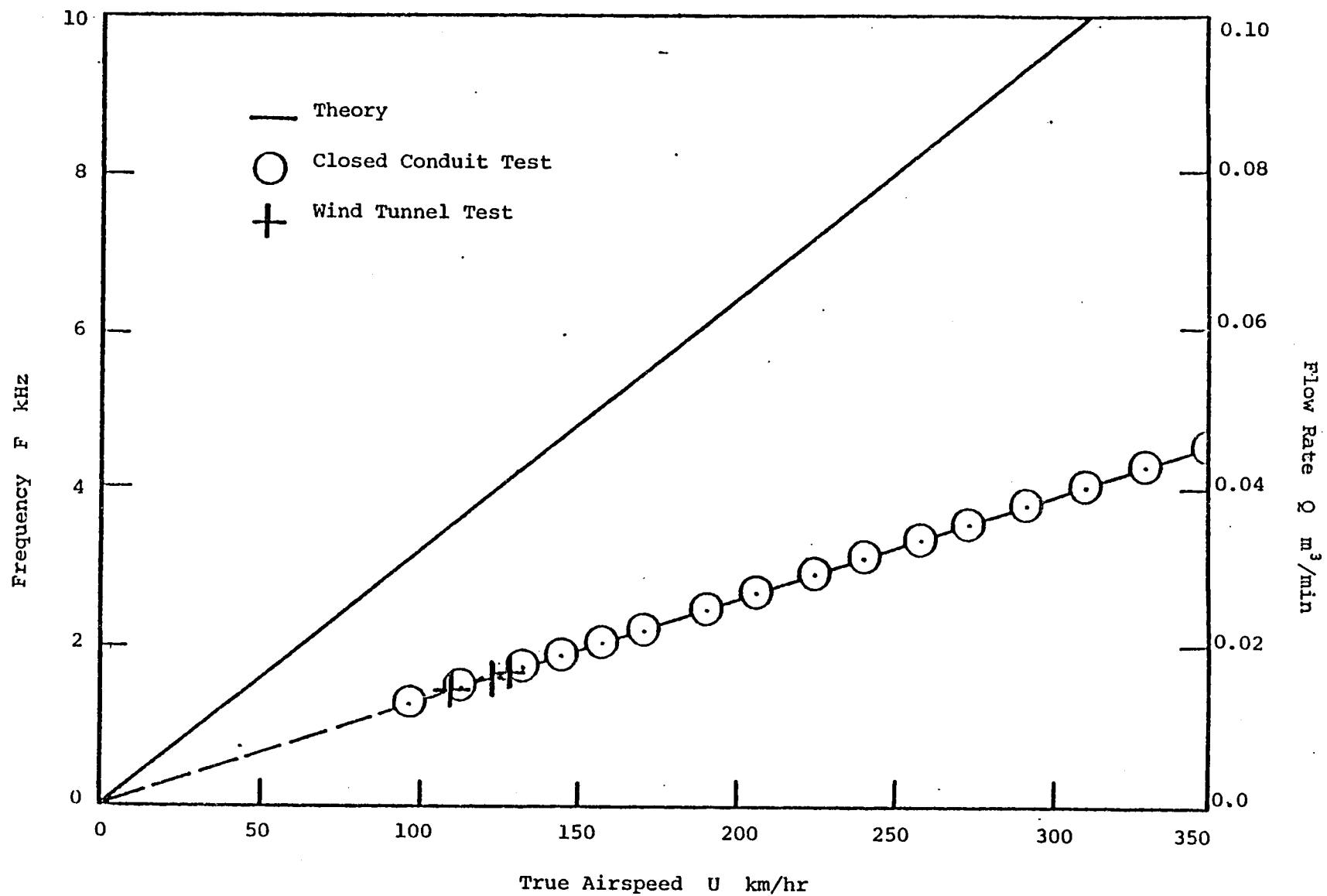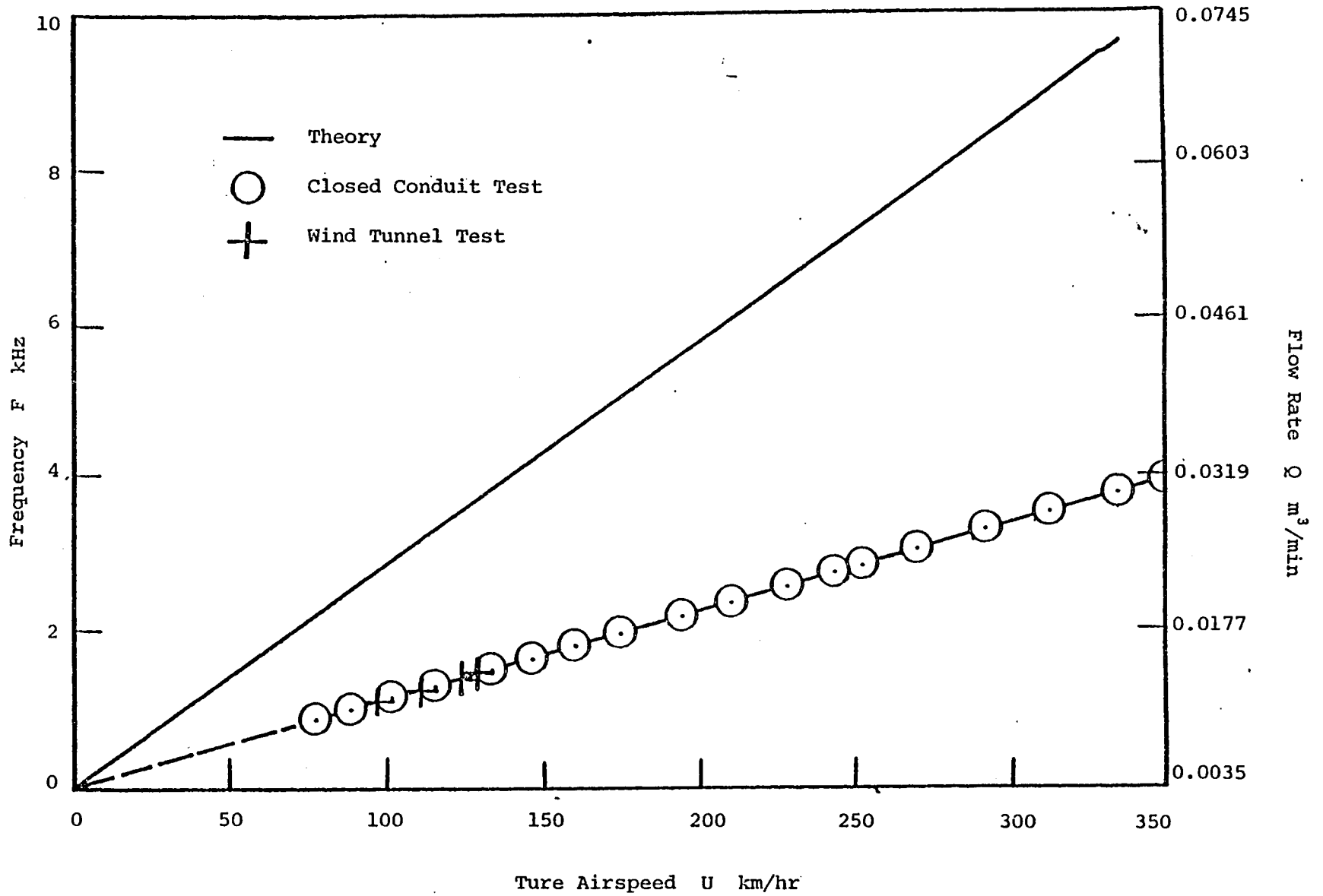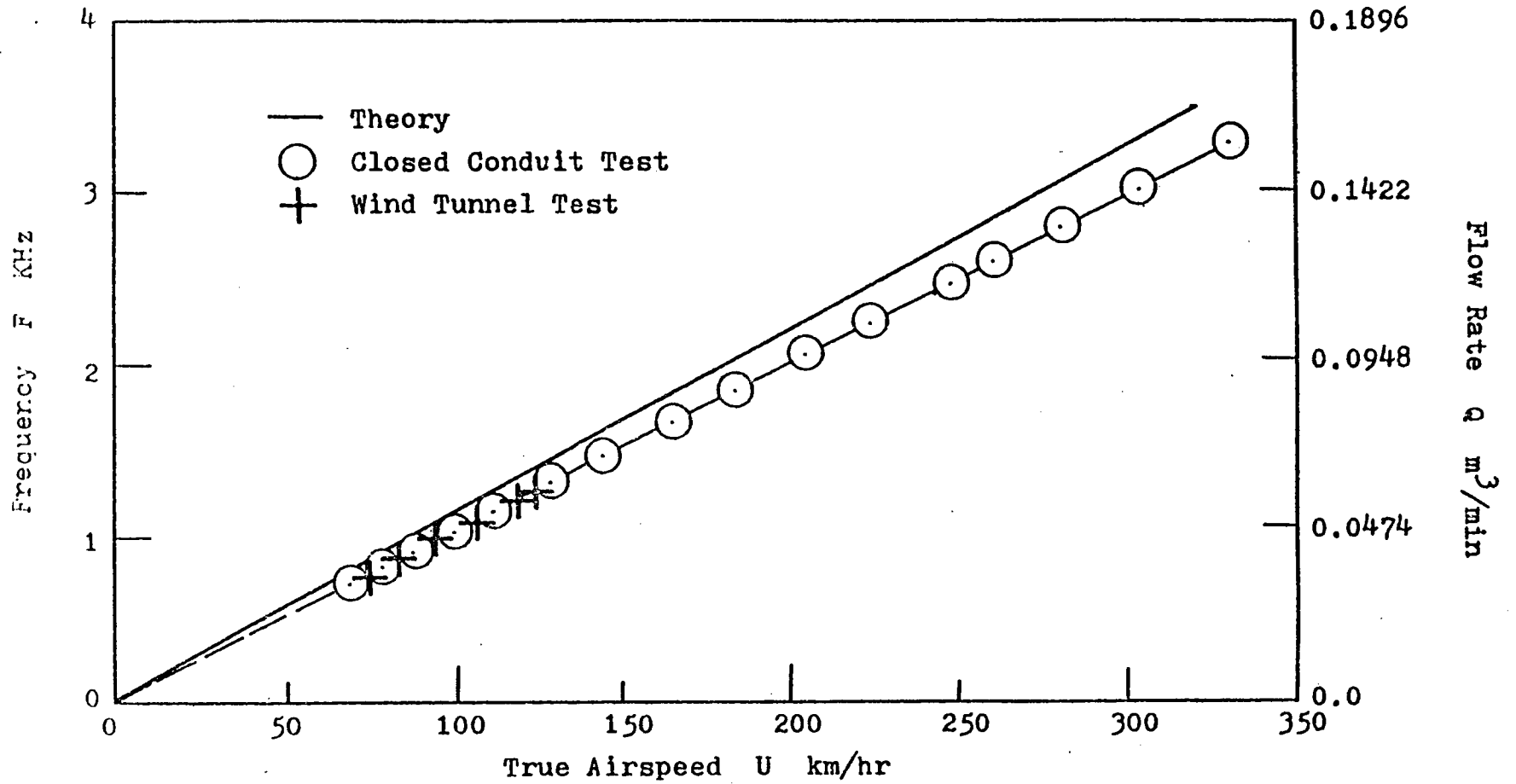Figure 73. Performance of sensor 1 with swirler having 4 flutes and exit angle 60°.
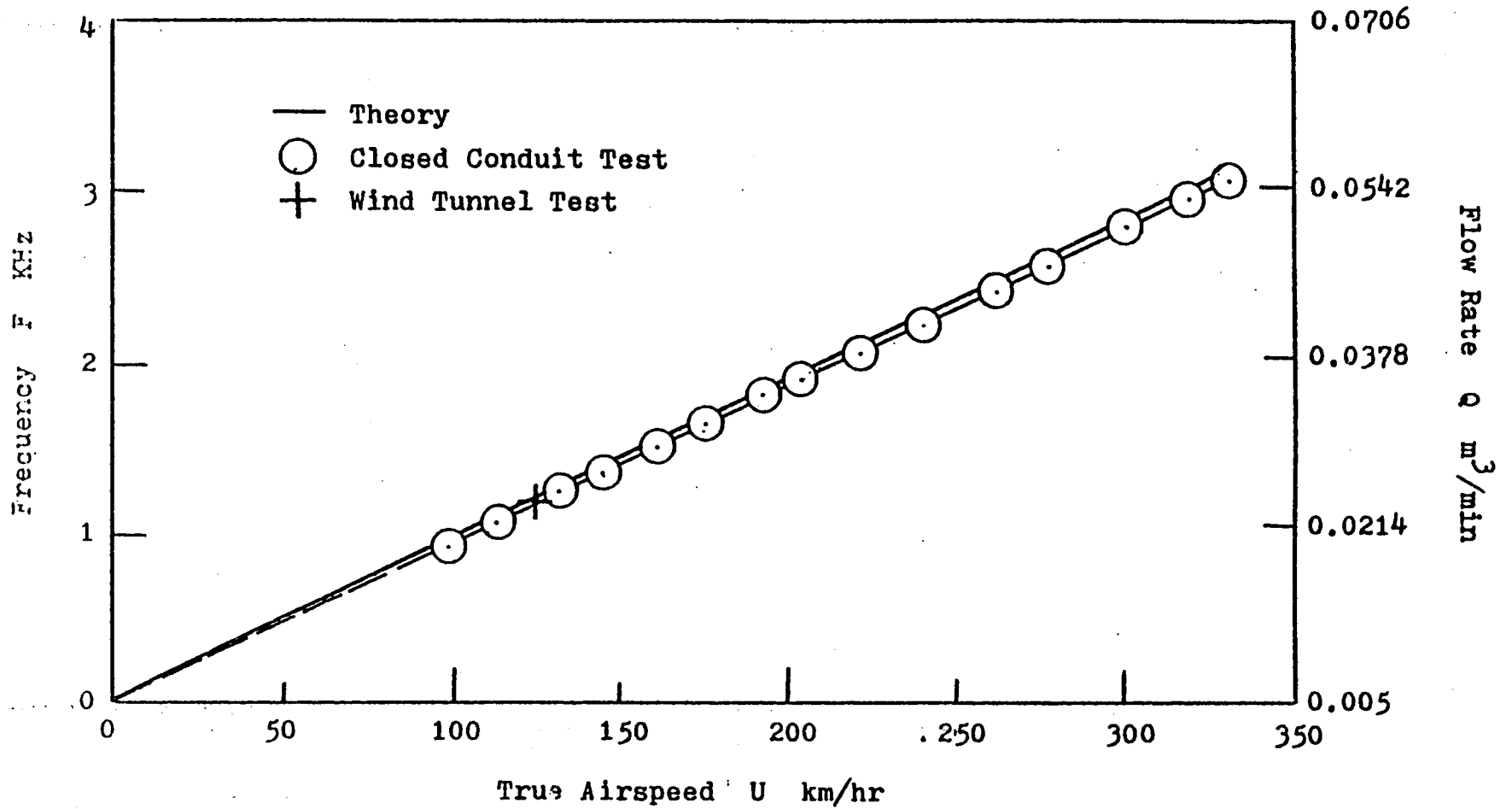
Figure 74. Performance of sensor 1 with swirler having 4 flutes and exit angle 75°.
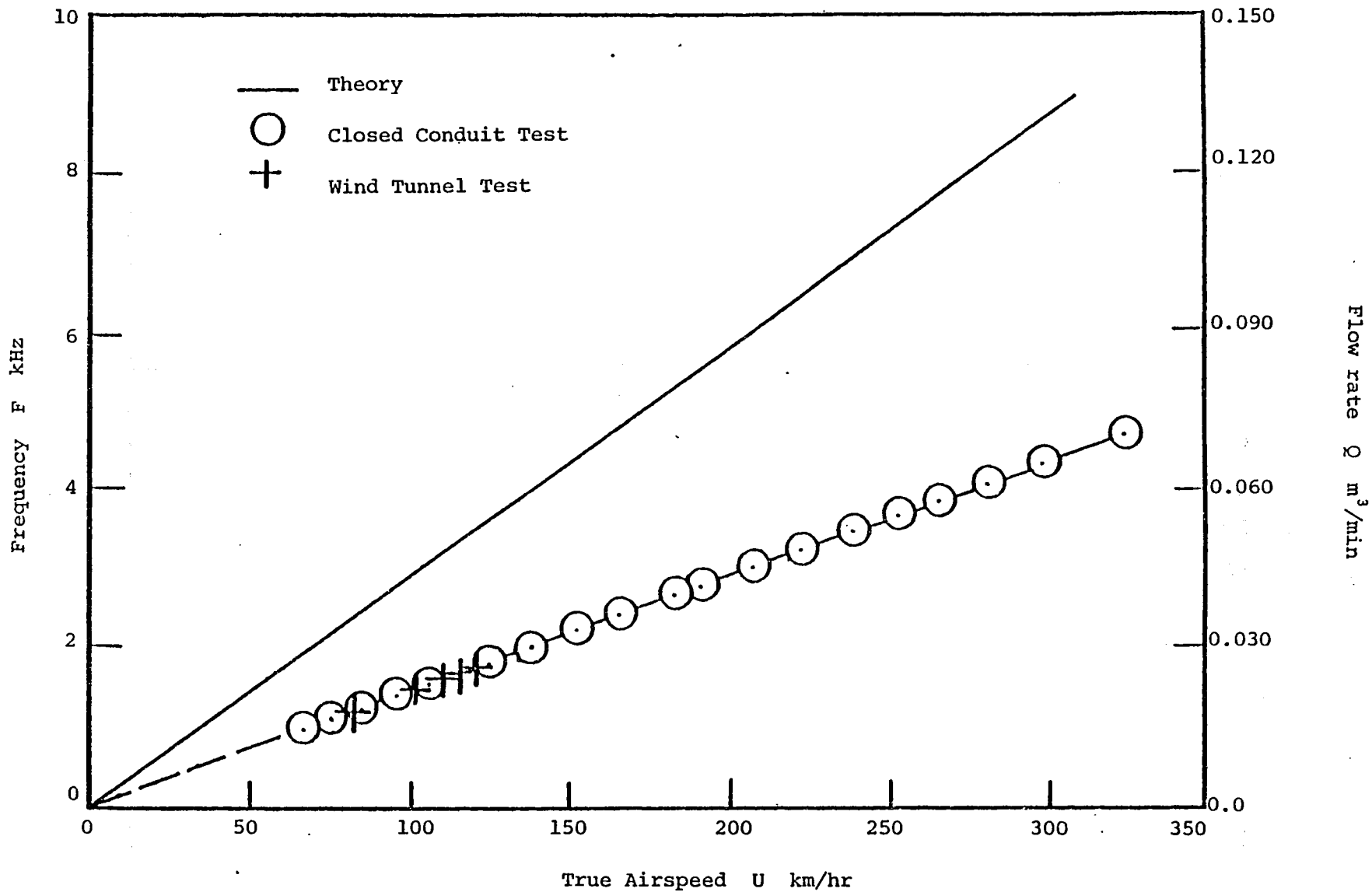
Figure 75. Performance of sensor 2 with swirler having 4 flutes and exit angle 45°.

Figure 76. Performance of sensor 2 with swirler having 4 flutes and exit angle 60°.

Figure 77. Performance of sensor 2 with swirler having 4 flutes and exit angle 75°.

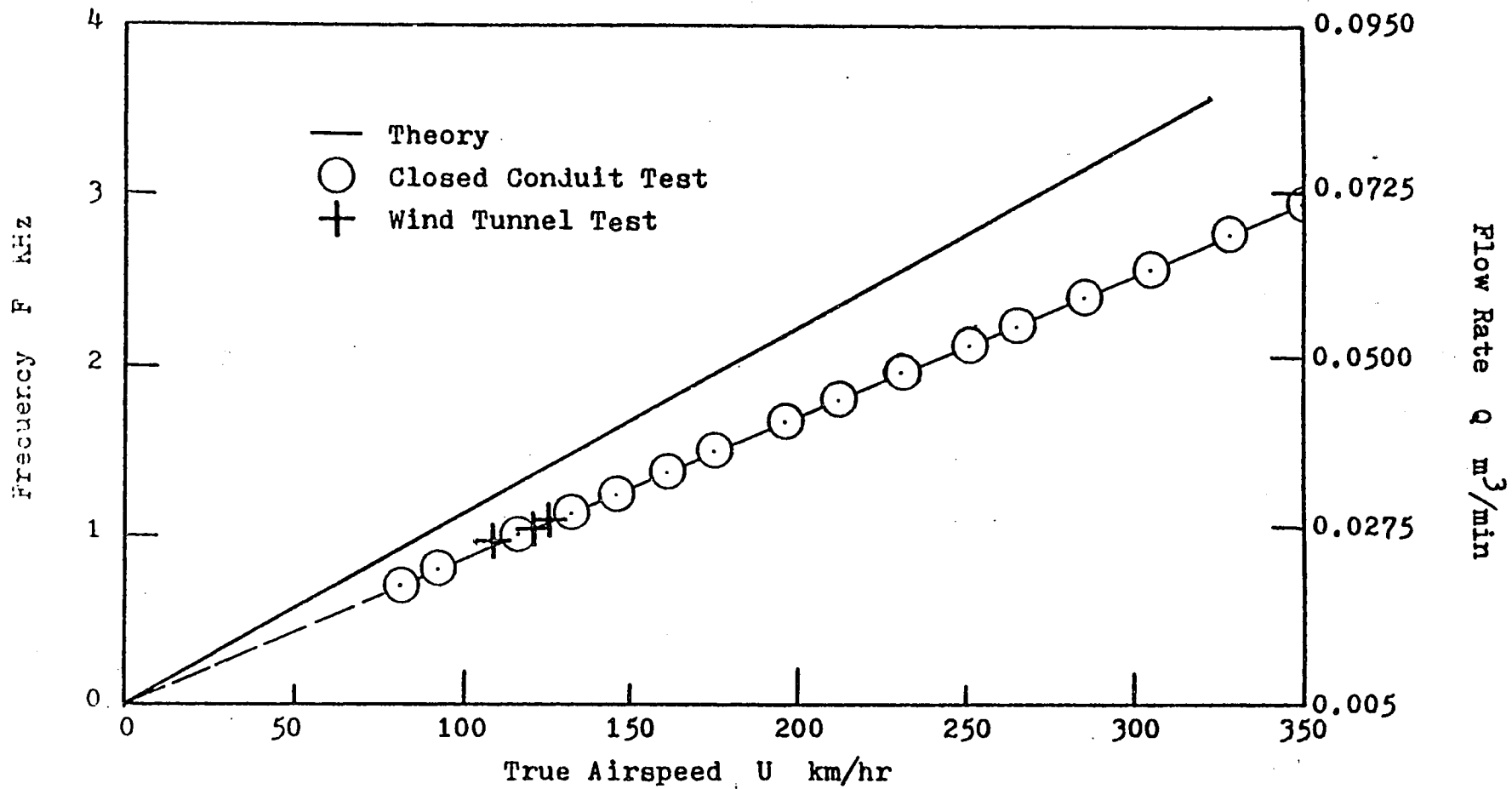Figure 78. Performance of sensor 3 with swirler having 4 flutes and exit angle 45°.

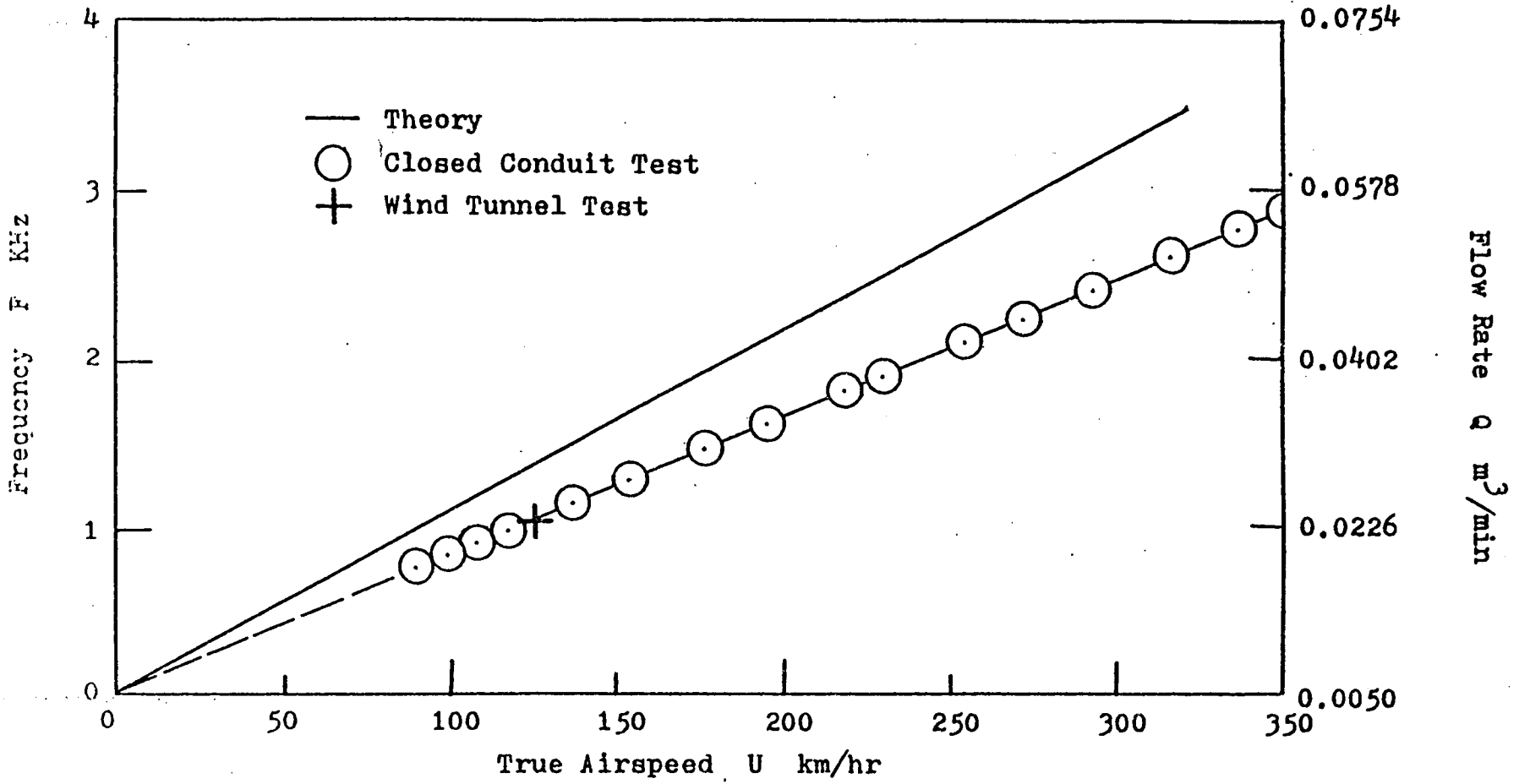Figure 79. Performance of sensor 3 with swirler having 4 flutes and exit angle 60°.

Figure 80. Performance of sensor 3 with swirler having 4 flutes and exit angle 75°.
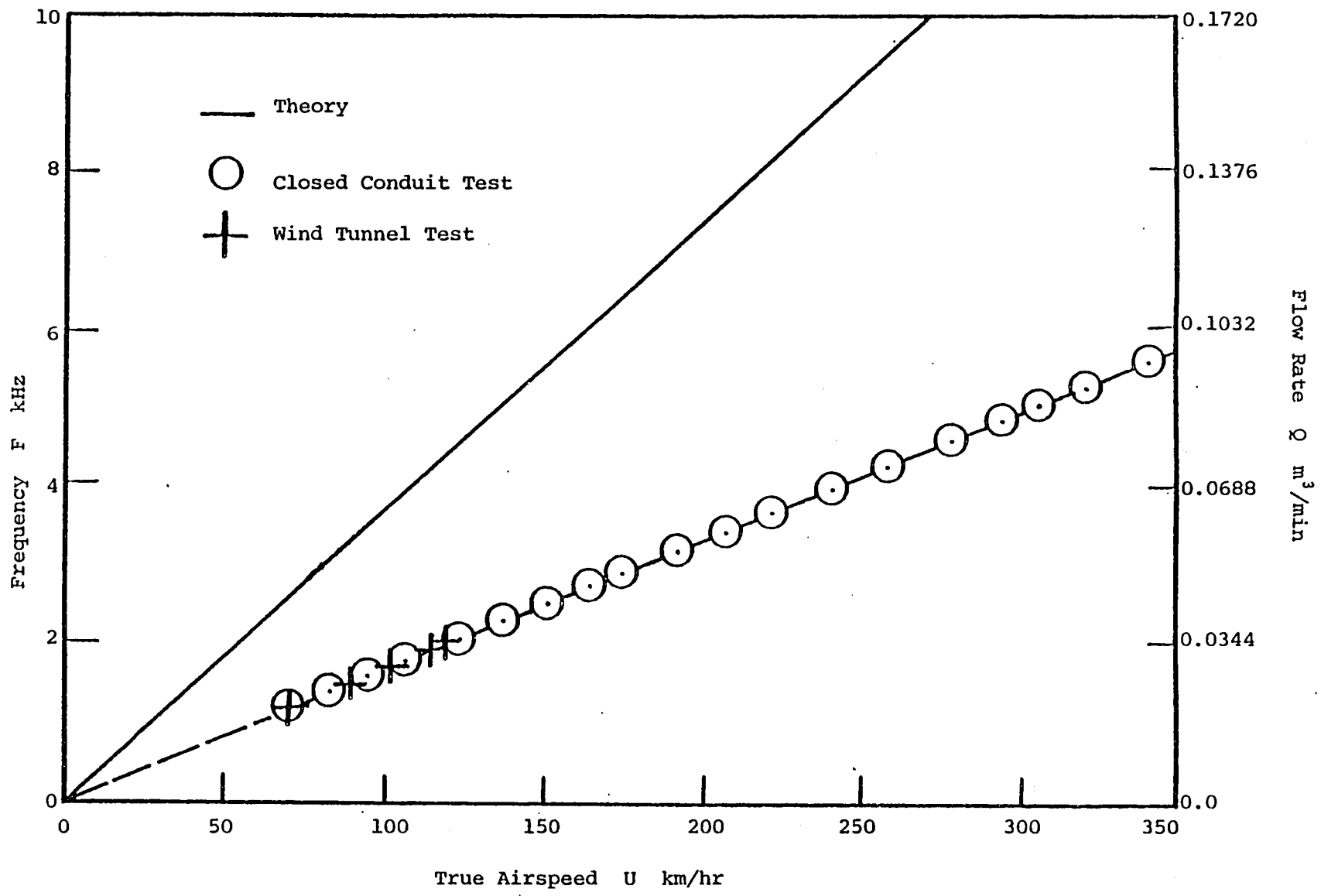
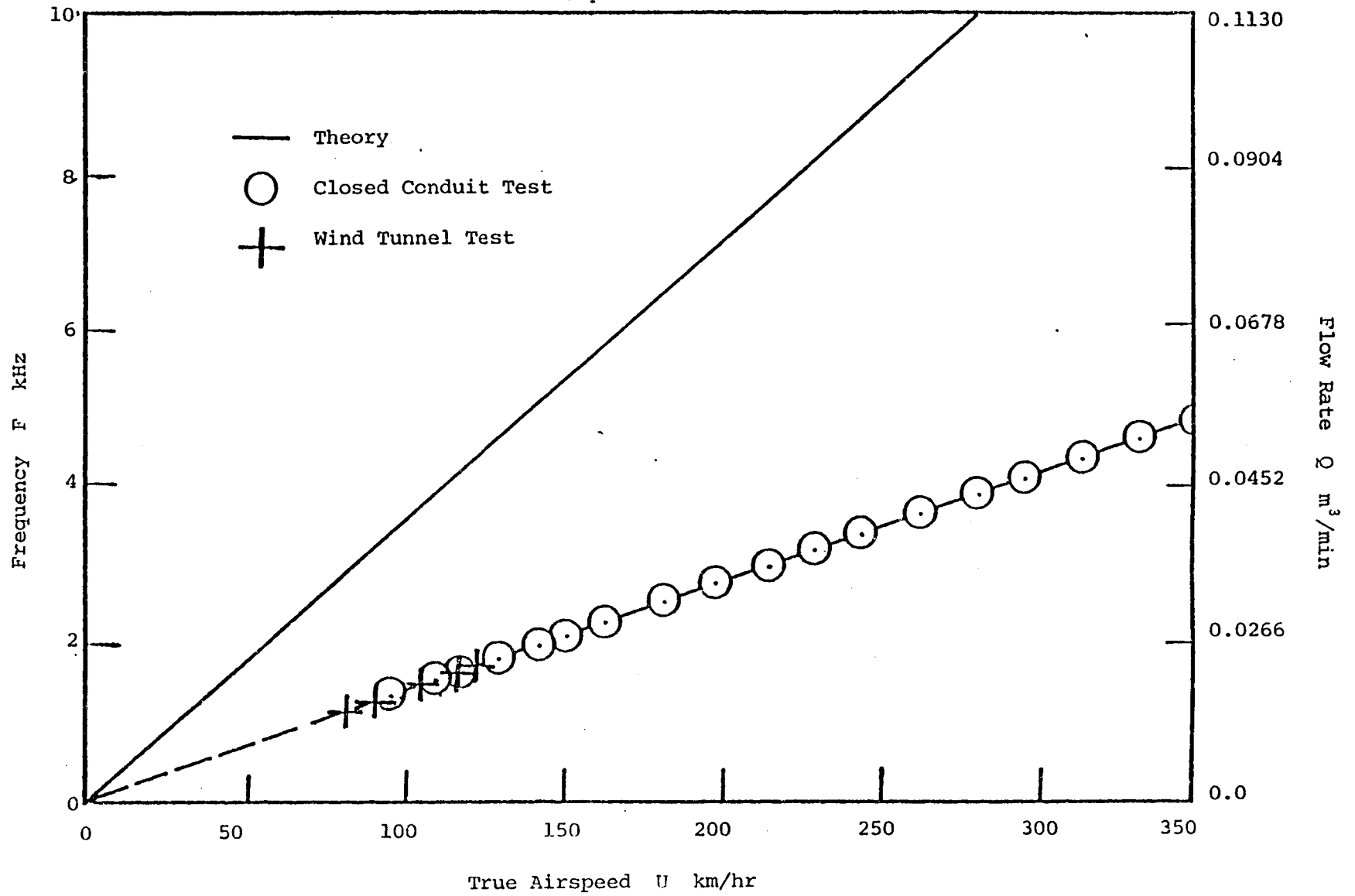Figure 81. Performance of sensor 4 with swirler having 4 flutes and exit angle 45°.

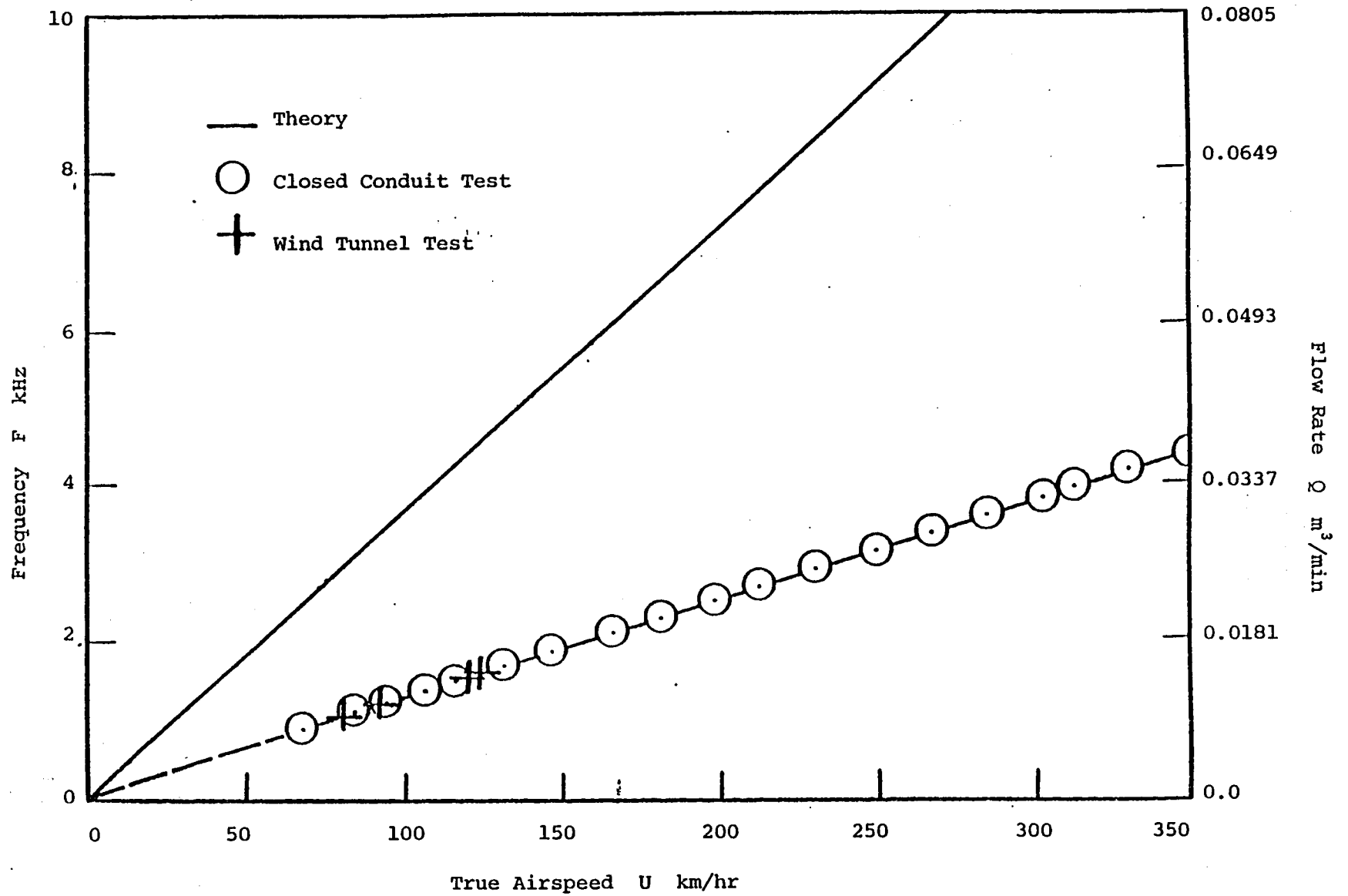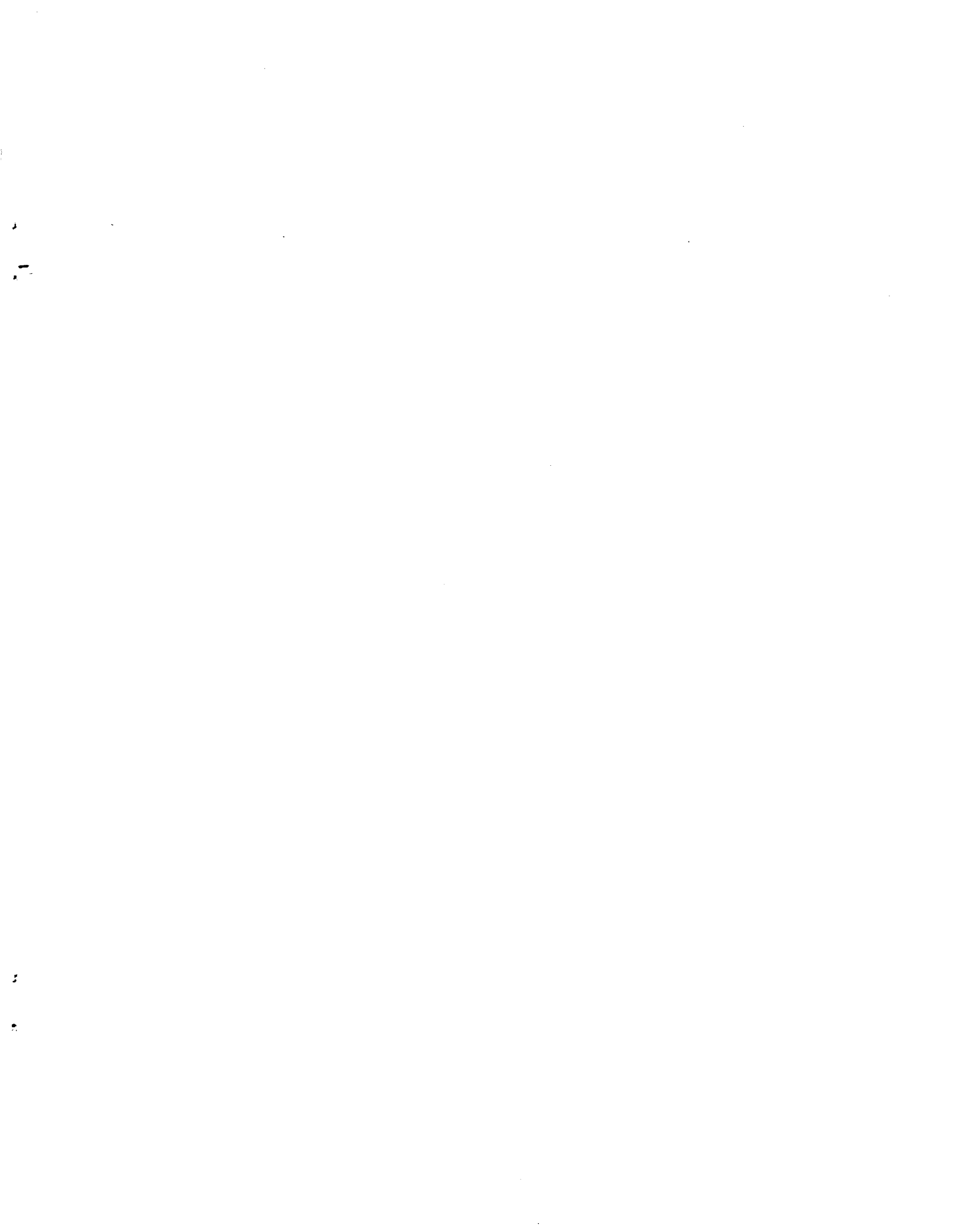Figure 82. Performance of sensor 4 with swirler having 4 flutes and exit angle 60°.

Figure 83. Performance of sensor 4 with swirler having 4 flutes and exit angle 75°.

1. Report No. NASA CR-165704	2. Government Accession No.	3. Recipient's Catalog No.
4. Title and Subtitle Experimental and Analytical Studies of A True Airspeed Sensor		5. Report Date May 1983
		6. Performing Organization Code

7. Author(s)
    G. L. Goglia
    J. Y. Shen
		8. Performing Organization Report No.

		10. Work Unit No.
9. Performing Organization Name and Address Old Dominion University Research Foundation P.O. Box 6369 Norfolk, Virginia 23508		
		11. Contract or Grant No. NSG-1177
12. Sponsoring Agency Name and Address National Aeronautics and Space Administration Washington, DC 20546		13. Type of Report and Period Covered Contractor Report
		14. Sponsoring Agency Code 505-41-63-03

15. Supplementary Notes
 	
  Langley Technical Monitor: R. F. Hellbaum
  Final Report - Period ending February 29, 1980		

16. Abstract The objective of this study was to design and analyze a true airspeed sensor based on the precession of a "vortex whistle" for sensing airspeeds up to 321.9 km/hr (200 mph). In an attempt to model the complicated fluid mechanics of the vortex precession, three-dimensional, inviscid, unsteady, incompressible fluid flow was studied by using the hydrodynamical linearized stability theory. The temporal stability approach was used to derive the relationship between the true airspeed and frequency response. The results show that the frequency response is linearly proportional to the airspeed. A computer program was developed to obtain the numerical solution. Computational results for various parameters were obtained.

The designed sensor basically consisted of a vortex tube, a swirler, and a transducer system. A microphone converted the audible tone to an electronic frequency signal. Measurements for both the closed-conduit tests and wind tunnel tests were recorded. For a specific flow rate or airspeed, larger exit swirler angles produced higher frequencies. For a smaller cross-sectional area in the precessional flow region, the frequency was higher. It was observed that as the airspeed was increased the Strouhal number remained constant. In some cases, the experimental results were found to be in reasonable agreement with the theoretical predictions. The viscous effect on the performance of the sensor was appreciable for some sensors.

17. Key Words (Suggested by Author(s)) Airspeed, Vortex, Whistle, Anemometer	18. Distribution Statement Unclassified-Unlimited Subject Category 06		
19. Security Classif. (of this report) Unclassified	20. Security Classif. (of this page) Unclassified	21. No. of Pages 172	22. Price A08

N-305